

NONINVASIVE ABSOLUTE CEREBRAL OXIMETRY
WITH FREQUENCY-DOMAIN
NEAR-INFRARED SPECTROSCOPY

A dissertation submitted

by

Bertan Hallacoglu

In partial fulfillment of the requirements

for the degree of

Doctor of Philosophy

in Biomedical Engineering

TUFTS UNIVERSITY

May 2013

© Copyright 2013 by Bertan Hallacoglu

ADVISER: Sergio Fantini

Acknowledgments

The time spent at Tufts University helped me develop not only as an intellectual, but also as an individual. It is with great pleasure that I acknowledge the many people that made this dissertation possible.

Firstly, I would like to start by thanking my advisor, Prof. Sergio Fantini. He has led me by example and expected me to set a high standard of quality for my work. Despite his busy schedule, he always kept his door open and made time for fruitful discussions. Sergio has shown me the importance of strategic and critical thinking. His great instinct for research and the ability to draw connections to simplify complex problems are attributes that I hope I have acquired during the time I worked under his guidance. I am also grateful to Prof. Angelo Sassaroli for his devotion to share his knowledge and experience. I am indebted to Angelo for being my mentor in the world of photon migration, for the many discussions we have had over diffusion theory and Monte Carlo simulations, and his enthusiasm for my research, which was always a source of motivation.

Many thanks to the members of my dissertation committee, Prof. Aron Troen, Prof. Fiorenzo Omenetto and Prof. Robin Kanarek for their valuable insights since the preliminary stages of my work.

I single out Prof. Aron Troen, with whom we have collaborated for many years. Aron has not only been a collaborator, but a mentor and a friend. Together, we have answered many research questions and started many new ones. I am thankful to him for

preaching me to always keep in mind the “big picture”. His work ethic, creativity, and ability to think outside the box have been ever so inspirational.

I am indebted to all of our collaborators; particularly to Dr. Irwin H. Rosenberg for always encouraging me to think from the clinical perspective, Dr. Fabrizio Martelli, Dr. Alwin Kienle and Dr. Andrea Liemert for their support in regards to theoretical modeling and implementation, and Prof. Eric Miller for discussions on inverse problems especially at the closing stages of my work. I would also like to acknowledge other collaborators, with whom I have worked over the years, including Dr. Harriet Paltiel, Dr. Daniel Weiner, and Dr. Michal Beeri.

I would like to thank the various faculty members in the Department of Electrical Engineering at Wentworth Institute of Technology for preparing me for graduate school education and Prof. Joseph Noonan for introducing me to Tufts University. Together with Sergio, having Prof. Noonan as a co-advisor during my master’s years was invaluable for getting me started as a graduate researcher.

I acknowledge various officemates I have had during my PhD; Ning Liu, Michele Pierro, Debbie Chen Cockrell, Feng Zheng, Yang Yu, Pami Anderson, and Roni Cantor for all the on and off work discussions and brainstorming sessions. I pay special tribute to Michele Pierro as we have closely collaborated and been through the highest and lowest point of our PhD years together. I also acknowledge other members of the diffuse optics group including Richard Matulewicz, Elleesse Pillas, Gee Weliwitigoda, Lia Hocke, Roni Cantor Balan, Jana Kainerstorfer and Nishanth Krishnamurthy with whom I have collaborated over the years.

I am thankful to Dean Gletting, Oguz Semerci, and Fridrik Larusson for various discussions about our research and post graduation plans. I will cherish our friendship and the conversations during the stressful days of our PhDs.

I thank my friends Margarita Parasi for her critical reading of this dissertation and Berke Cincin for his support from afar throughout the years.

Vëllai im, Ilir Kullolli, the closest friend I have ever had. I have made some of the most important decisions in my life in light of the discussions I have had with him. I thank him for always being there for me whether times are happy or sad. My American mom, Donna Parine, for welcoming me to the U.S. as a teenager and considering me her second son. I thank her for all her support throughout the years.

I would like to thank my grandparents Mualla and Sadan Berkan. Every good in me has been inspired by them in some way. My mother Hulya Birtek, for her unconditional love and support, and my father Tanju Hallacoglu for always being there when I needed him. Without my family and their guidance I would not have made it to where I am today.

The two individuals that this dissertation is dedicated to; my stepfather, Faruk Birtek, for being as close to me as a father can be, and everything he has done for me to become the man I am today. I can only wish to influence someone's life one day as he has so profoundly influenced mine. Finally, agapi mou, Maria Theodorou. She has been my fuel, life saver, and den. She has taken care of me and supported me both physically and emotionally throughout the years. Without her, I would not have survived the demanding life style that comes with being a PhD student.

Noninvasive absolute cerebral oximetry with frequency-domain near-infrared spectroscopy

Bertan Hallacoglu, April 2013

Tufts University, Department of Biomedical Engineering

Abstract

Near-infrared spectroscopy (NIRS) measurements of absolute concentrations of oxy-hemoglobin and deoxy-hemoglobin in the human brain can provide critical information about cerebral physiology in terms of cerebral blood volume, blood flow, oxygen delivery, and metabolic rate of oxygen. We developed several frequency domain NIRS data acquisition and analysis methods aimed at absolute measurements of hemoglobin concentration and saturation in cerebral tissue of adult human subjects.

Extensive experimental investigations were carried out in various homogenous and two-layered tissue-mimicking phantoms, and biological tissues. The advantages and limitations of commonly used homogenous models and inversion strategies were thoroughly investigated. Prior to human subjects, extensive studies were carried out in *in vivo* animal models. In rabbits, absolute hemoglobin oxygen desaturation was shown to depend strongly on surgically induced testicular torsion. Methods developed in this study were then adapted for measurements in the rat brain. Absolute values were demonstrated to discern cerebrovascular impairment in a rat model of diet-induced vascular cognitive impairment. These results facilitated the development of clinically useful optical measures of cerebrovascular health. In a large group of human subjects, employing a

homogeneous model for absolute measurements was shown to be reliable and robust. However, it was also shown to be limited due to the relatively thick extracerebral tissue.

The procedure we develop in this work and the thesis thereof performs a nonlinear inversion procedure with six unknown parameters with no other prior knowledge for the retrieval of the optical coefficients and top layer thickness with high accuracy on two-layered media. Our absolute measurements of cerebral hemoglobin concentration and saturation are based on the discrimination of extracerebral and cerebral tissue layers, and they can enhance the impact of NIRS for cerebral hemodynamics and oxygenation assessment both in the research arena and clinical practice.

List of Tables

Table 5.1. Mean absolute values of the optical properties, hemoglobin concentrations measured in testicular tissue in rabbit.....	50
Table 5.2. Cerebral NIRS parameters measured at baseline and after induction of hypoxia or hypercapnia, in folate deficient (FD) and control rats at 10 and 20 weeks	67
Table 5.3. Dependence of optical measurements on source-detector separation.....	81
Table 5.4. Summary of absolute measurements in elderly and young subjects.....	85
Table 6.1. Demonstration of the insensitivity of the inversion procedure to initialization. Convergence with good and bad initialization is reported.....	102
Table 6.2. Retrieved optical coefficients and first layer thickness on the forehead of three human subjects.....	113
Table 6.3. Retrieved optical coefficients on the forehead of three human subjects using a homogenous model as a comparison with Table 3	113
Table 6.4. Retrieved concentrations of oxy-hemoglobin and deoxy-hemoglobin on the forehead of three human subjects using two-layered (indicated by “Superficial” and “Cerebral”) and homogeneous models	113
Table 6.5. Retrieved total hemoglobin concentration and hemoglobin oxygen saturation on the forehead of three human subjects using two-layered (indicated by “Superficial” and “Cerebral”) and homogeneous models.....	114

List of Figures

Figure 1.1. Absorption spectra of oxy- and deoxy-hemoglobin, and water.....	2
Figure 1.2. A depiction of the effect of scattering in biological tissues	3
Figure 1.3. The three experimental paradigms employed in NIRS measurements.....	4
Figure 2.1. NIRS infinite geometry arrangement	11
Figure 2.2. NIRS semi-infinite geometry arrangement.....	14
Figure 2.3. NIRS two-layered planar geometry arrangement.....	17
Figure 2.4. NIRS two-layered cylindrical geometry arrangement.....	19
Figure 4.1. Block diagram of the Monte Carlo (MC) simulations.....	36
Figure 4.2. Block diagram of the heterodyne detection scheme	39
Figure 5.1. Specially-designed optical probe for the testicular ischemia study.....	47
Figure 5.2. Absolute values of concentrations of oxy- and deoxy-hemoglobin measured in testicular tissue in rabbit	52
Figure 5.3. Absolute hemoglobin saturation values measured in the testicular tissue for all four rabbits.....	53
Figure 5.4. Experimental setup for NIRS measurements in rat	59
Figure 5.5. Optical properties of brain tissue measured in rat	61
Figure 5.6. Hemoglobin values during the hypoxia protocol ten weeks after the start of folate deficient (FD) diet.....	65
Figure 5.7. Hemoglobin values during the hypoxia protocol twenty weeks after the start of folate deficient (FD) diet	66

Figure 5.8. Relative differences in cerebral tissue hemoglobin values in rat	68
Figure 5.9. Vasomotor reactivity (VMR) in response to hypercapnia in rat	71
Figure 5.10. Age distribution of the human subjects in the elderly and young study.....	75
Figure 5.11. Experimental setup and protocol in the elderly and young study.....	76
Figure 5.12. Source-detector distance dependence of the NIRS parameters in elderly subjects.....	80
Figure 5.13. NIRS parameters in Session 2 versus Session 1	82
Figure 5.14. Source-detector distance dependence of the NIRS parameters in elderly and young subjects.....	83
Figure 5.15. Mean values of NIRS parameters in the elderly young study	84
Figure 6.1. Homogenous phantom setup in infinite geometry arrangement.....	96
Figure 6.2. Results of the phantom measurements in the infinite geometry.....	97
Figure 6.3. Illustration of the two-layered liquid phantom	99
Figure 6.4. Results of the two-layered Monte Carlo (MC) simulations	101
Figure 6.5. Demonstration of the two-layered fitting procedure	103
Figure 6.6. A representative case illustrating the evolution of the parameter vector during the fitting procedure on two-layered phantom data	104
Figure 6.7. Results of the two-layered phantom measurements	105
Figure 6.8. Average of the absolute % errors in the measured parameters.....	106
Figure 6.9. Experimental setup for the human subject measurements.....	110
Figure 6.9. Results on the human subjects using two-layered analysis	112

Contents

Acknowledgments	ii
Abstract	v
List of Tables	vii
List of Figures	viii
Contents	x
Chapter 1. Introduction	1
1.1. Fundamentals of Near-Infrared Spectroscopy (NIRS)	1
1.2. The Purpose of this Work	6
1.3. Dissertation Outline	7
Chapter 2. Photon Migration in Turbid Media	10
2.1. Diffusion Theory.....	10
2.2. Solutions to the Diffusion Equation for Homogenous Media	11
2.2.1. Infinite boundary conditions	11
2.2.2. Semi-infinite boundary conditions.....	14
2.3. Solutions to the Diffusion Equation for Two-Layered Media	18
2.3.1. Solution in a Planar Geometry	18
2.3.2. Solution in a Cylindrical Geometry	20
Chapter 3. Cerebral Oximetry with NIRS	23
3.1. Background and Clinical Significance.....	23
3.2. Current Methods	24
3.3. Implications.....	25

Chapter 4. Methods	33
4.1. Nonlinear Fitting Procedures	33
4.2. Monte Carlo Simulations	35
4.3. Instrumentation for frequency-domain NIRS	37
Chapter 5. Experimental Studies based on Homogenous Modeling	42
5.1. Rabbit model of testicular ischemia.....	43
5.1.1. Background to the Study.....	43
5.1.2. Methods.....	45
5.1.3. Results of the Study	50
5.1.4. Discussion of the Results	54
5.2. Rat model of Vascular Cognitive Impairment (VCI)	57
5.2.1. Background to the Study.....	57
5.2.2. Methods.....	57
5.2.3. Results of the Study	64
5.2.4. Discussion of the Results	71
5.3. Cerebral Oximetry in Elderly and Young Humans.....	75
5.3.1. Methods.....	75
5.3.2. Results.....	79
5.3.3. Discussion of the Results	85
Chapter 6. Experimental Studies based on Two-Layered Modeling	94
6.1. Homogenous Phantom Measurements.....	95
6.1.1. Methods.....	95
6.1.2. Results of the Infinite Medium Measurements.....	97
6.2. Two-layered Monte Carlo Simulations and Phantom Measurements	98
6.2.1. Methods.....	98

6.2.2. Results of the Monte Carlo Simulations	100
6.2.3. Results of the Two-layered Phantom Measurement	102
6.2.4. Discussion of the Results	107
6.3. Demonstration in Human Volunteers	109
6.3.1. Methods.....	109
6.3.2. Results.....	111
6.3.3. Discussion of the Results	114
Chapter 7. Summary and Future Directions.....	121
Appendix A.....	126
Appendix B.....	129
Appendix C.....	133

Chapter 1

Introduction

1.1. Fundamentals of Near Infrared Spectroscopy (NIRS)

Near-infrared spectroscopy (NIRS), also known as Diffuse Optical Spectroscopy (DOS) when applied to biological tissues, is an optical spectroscopic technique that utilizes safe levels of light emission in the wavelength region 650–950 nm. In applications regarding spectroscopy of biological tissues, near-infrared light experiences two physical processes. The first one is absorption, described in terms of the absorption coefficient (μ_a) that typically assumes values between 0.01 and 0.1 cm^{-1} in biological tissues at near infrared wavelengths. Such a low value of μ_a accounts for the large penetration depth, up to several centimeters, of near-infrared light into tissues. Tissue absorption is due to the presence of a number of chromophores including hemoglobin and water, with smaller contributions from lipids (Taroni *et al.* 2003) and cytochrome oxidase in the near infrared (Wray *et al.* 1988). In particular, between 670 and 850 nm, the primary chromophores in the spectral window are oxygenated hemoglobin (HbO_2), deoxygenated hemoglobin (Hb), and water (H_2O). This feature renders NIRS particularly sensitive to hemoglobin concentrations and hemodynamics. Each of these chromophores possesses a distinct absorption spectrum as shown in figure 1.1.

The second process experienced by photons inside tissues is a phenomenon called scattering, which is described in terms of the reduced scattering coefficient (μ'_s). The reduced scattering coefficient is typically one to two orders of magnitude greater than the absorption coefficient (typically between 2 and 20 cm^{-1} in biological tissues in the near infrared), so that light scattering dominates over absorption in most biological tissues. The consequence of the much larger reduced scattering characteristics of biological tissues is that the near-infrared light injected into the tissue rapidly becomes a diffuse photon density wave, which then traverses the tissue. This poses an intrinsic limitation to the spatial resolution of non-invasive optical imaging, which is limited to a few millimeters. Depending on the biological tissue of interest, photon scattering originates from the discontinuities in the refractive index at different cellular membranes and organelles. The effect of scattering in biological tissues is depicted through the illustration in figure 1.2.

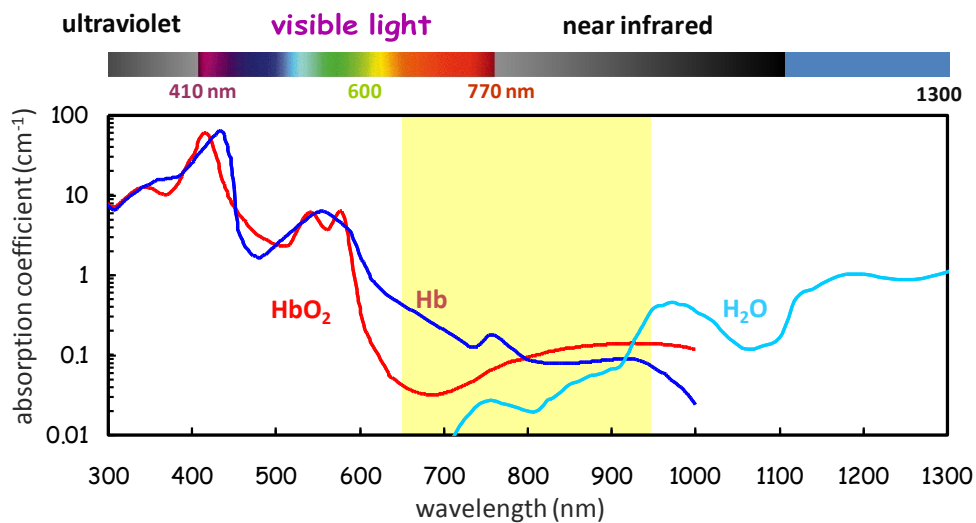


Figure 1.1. Absorption spectra of oxy-hemoglobin (HbO₂), deoxy-hemoglobin (Hb), and water (H₂O). Spectra adapted from (Hale and Querry 1973; Cheong et al. 1990)

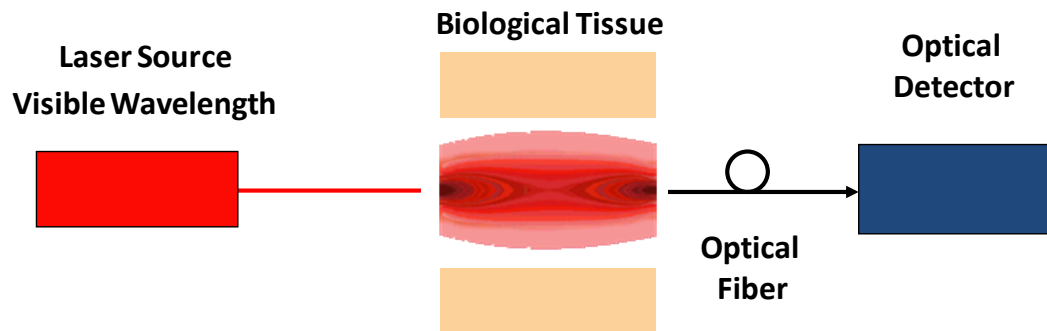


Figure 1.2. A depiction of the effect of scattering in biological tissues.

Absolute hemoglobin concentrations can be directly derived from the absorption spectra seen in figure 1.1. However, the strong diffusion of light in tissue and the effects of both optical coefficients (*i.e.* μ_a and μ'_s) on light propagation requires dedicated models to discriminate between the absorption and scattering contributions to light attenuation in tissue. Such models include random walk analysis (Gandjbakhche *et al.* 1993), transport theory models (Gu *et al.* 2007), and diffusion theory (Patterson *et al.* 1989). Diffusion theory will be discussed in detail later Chapters (Chapter 2, in particular) as it is the basis of the analysis techniques presented in this manuscript.

There are three main experimental paradigms employed for NIRS measurements, namely Continuous Wave (CW), Time Domain (TD), and Frequency Domain (FD). Schematic representations of these approaches are presented in figure 1.3.

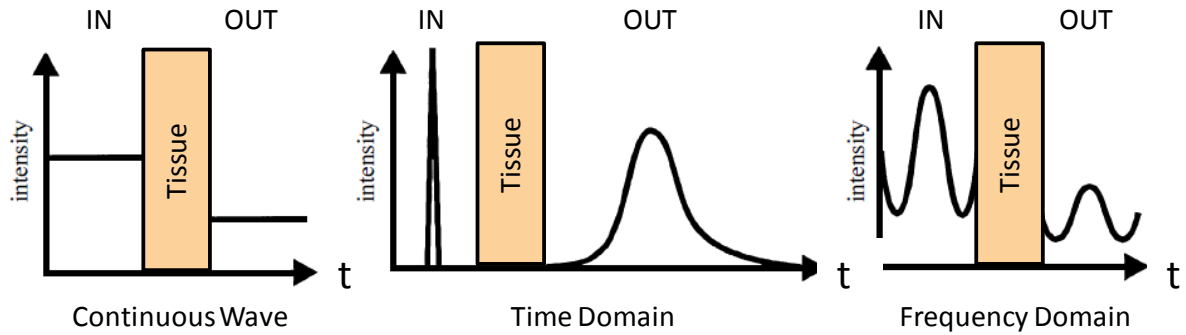


Figure 1.3. Input and output relationships of the three main experimental paradigms employed in NIRS measurements. Left, middle, and right panels represent continuous wave, time domain, and frequency domain, respectively. The x -axes represent time.

Briefly, TD systems employ a relatively short pulse of probing beam (of the order of few ps width) and measure the distribution of time of flight (of the order of ns) of the photons that traverses the tissue (Torricelli *et al.* 2011). Alternatively, FD systems employ sinusoidally modulated light intensity as the source and measure the changes in the average intensity, the amplitude, and the phase that the source undergoes as it traverses the tissue (Gratton *et al.* 1997). Continuous wave (CW) domain systems employ continuous illumination of tissues and measure the change in the amplitude of the light intensity. Standard CW systems are not capable of discriminating absorption and scattering coefficients; however there is an ongoing effort to develop specialized CW methods to address this issue (Grabtchak and Whelan 2012; Yeganeh *et al.* 2012).

The ability to extract the concentrations of both hemoglobin species is a unique feature specific to NIRS methods. Together with its high temporal resolution (in the order of milliseconds), this in turn allows for real-time monitoring and spatial mapping of underlying physiological parameters such as blood volume, blood perfusion, metabolic rate of oxygen, and oxygen delivery in tissues. Today, NIRS techniques are employed in

various research applications, for instance, optical mammography (Cerussi *et al.* 2001; Yu *et al.* 2009), exercise medicine (Belardinelli *et al.* 1995; Fantini *et al.* 1995), photodynamic therapy (Wang *et al.* 2004) and radiation therapy monitoring (Sunar *et al.* 2006), testicular ischemia detection (Hallacoglu *et al.* 2009; Burgu *et al.* 2013), a variety of applications in brain spectroscopy and imaging (for a review, see Elwell and Cooper 2011 (Elwell and Cooper 2011)) and more.

In this work and the manuscript thereof, I focus on the application of NIRS in noninvasive investigation of brain tissue. Specifically, the potential of NIRS for performing noninvasive *absolute* measurement of the concentration and oxygen saturation of hemoglobin in the human cerebral tissue is explored.

1.2. The Purpose of this Work

Accurate real-time NIRS cerebral oximetry can significantly improve critical patient care and routine clinical practice (*i.e.* emergency care, perioperative practice) (Tweddell *et al.* 2010; Parnia *et al.* 2012; Sekhon *et al.* 2012); however concerns remain on the reliability of the current methods particularly due to extracerebral tissue contamination in the NIRS measurements (Hirsch *et al.* 2010; Tweddell *et al.* 2010; Davie and Grocott 2012).

Recent advances in the field yielded techniques aimed at either inhibiting the contribution of the extracerebral tissue layer to the optical signals, or directly measuring cerebral tissue layer quantities with the help of other imaging modalities (for instance, Magnetic Resonance Imaging to measure scalp-cortex distance). The key contribution of this work is the development of a standalone frequency domain NIRS method aimed at measuring the optical coefficients of two-layered media and the thickness of the first of the two-layers from diffuse reflectance measurements, particularly for absolute cerebral oximetry application. In this manuscript, I present a collection of simulations and experiments that were carried out for the development of this method. Experimental approaches that will be presented entail *in vivo* measurements in an extended sample set of tissues, including small (rabbit testicle, rat brain) and large (human brain) tissues, as well as measurements in homogenous and layered tissue-like phantoms.

1.3. Dissertation Outline

The manuscript is structured in the following order. In Chapter 2, I discuss the intricacies of photon migration in biological tissues and provide a detailed description of diffusion theory based modeling scenarios considered in this work. Chapter 3 is an introductory chapter about cerebral oximetry, where a broad literature overview about the state-of-the-art and the limitations of the current approaches are presented. Chapter 4 covers the methods that were employed in this work including the fitting procedures, Monte Carlo simulations, and the instrumentation. Chapters 5 and 6 are dedicated to all the experimental approaches carried out in this work with the ultimate goal of performing absolute cerebral oximetry in human subjects. Specifically, I discuss the experimental approaches employing homogenous modeling in Chapter 5 and two-layered modeling in Chapter 6. Finally, in Chapter 7, implications and discussion of the experimental approaches as well as future directions are provided.

References for Chapter 1

- Belardinelli, R., T. J. Barstow, J. Porszasz and K. Wasserman (1995). "Changes in skeletal muscle oxygenation during incremental exercise measured with near infrared spectroscopy." Eur J Appl Physiol Occup Physiol **70**(6): 487-492.
- Burgu, B., O. Aydogdu, R. Huang, T. Soygur, O. Yaman and L. Baker (2013). "Pilot Feasibility Study of Transscrotal Near Infrared Spectroscopy in the Evaluation of Adult Acute Scrotum." J Urol.
- Cerussi, A. E., A. J. Berger, F. Bevilacqua, N. Shah, D. Jakubowski, J. Butler, R. F. Holcombe and B. J. Tromberg (2001). "Sources of absorption and scattering contrast for near-infrared optical mammography." Acad Radiol **8**(3): 211-218.
- Davie, S. N. and H. P. Grocott (2012). "Impact of extracranial contamination on regional cerebral oxygen saturation: a comparison of three cerebral oximetry technologies." Anesthesiology **116**(4): 834-840.
- Elwell, C. E. and C. E. Cooper (2011). "Making light work: illuminating the future of biomedical optics." Philos Transact A Math Phys Eng Sci **369**(1955): 4358-4379.
- Fantini, S., M.-A. Franceschini, J. S. Maier, S. A. Walker, B. B. Barbieri and E. Gratton (1995). "Frequency-domain multichannel optical detector for noninvasive tissue spectroscopy and oximetry." Optical Engineering **34**(1): 32-42.
- Gandjbakhche, A. H., H. Taitelbaum and G. H. Weiss (1993). "Random walk analysis of time-resolved transillumination measurements in optical imaging." Physica A: Statistical Mechanics and its Applications **200**(1-4): 212-221.
- Grabtchak, S. and W. M. Whelan (2012). "Separation of absorption and scattering properties of turbid media using relative spectrally resolved cw radiance measurements." Biomed Opt Express **3**(10): 2371-2380.
- Gratton, E., S. Fantini, M. A. Franceschini, G. Gratton and M. Fabiani (1997). "Measurements of scattering and absorption changes in muscle and brain." Philos Trans R Soc Lond B Biol Sci **352**(1354): 727-735.
- Gu, X., K. Ren and A. H. Hielscher (2007). "Frequency-domain sensitivity analysis for small imaging domains using the equation of radiative transfer." Appl Opt **46**(10): 1624-1632.
- Hallacoglu, B., R. S. Matulewicz, H. J. Paltiel, H. Padua, P. Gargollo, G. Cannon, A. Alomari, A. Sassaroli and S. Fantini (2009). "Noninvasive assessment of testicular torsion in rabbits using frequency-domain near-infrared spectroscopy: prospects for pediatric urology." J Biomed Opt **14**(5): 054027.
- Hirsch, J. C., J. R. Charpie, R. G. Ohye and J. G. Gurney (2010). "Near Infrared Spectroscopy (NIRS) Should Not Be Standard of Care for Postoperative Management." Seminars in Thoracic and Cardiovascular Surgery: Pediatric Cardiac Surgery Annual **13**(1): 51-54.
- Parnia, S., A. Nasir, C. Shah, R. Patel, A. Mani and P. Richman (2012). "A feasibility study evaluating the role of cerebral oximetry in predicting return of spontaneous circulation in cardiac arrest." Resuscitation **83**(8): 982-985.

- Patterson, M. S., B. Chance and B. C. Wilson (1989). "Time resolved reflectance and transmittance for the non-invasive measurement of tissue optical properties." Appl Opt **28**(12): 2331-2336.
- Sekhon, M. S., N. McLean, W. R. Henderson, D. R. Chittock and D. E. Griesdale (2012). "Association of hemoglobin concentration and mortality in critically ill patients with severe traumatic brain injury." Crit Care **16**(4): R128.
- Sunar, U., H. Quon, T. Durduran, J. Zhang, J. Du, C. Zhou, G. Yu, R. Choe, A. Kilger, R. Lustig, L. Loevner, S. Nioka, B. Chance and A. G. Yodh (2006). "Noninvasive diffuse optical measurement of blood flow and blood oxygenation for monitoring radiation therapy in patients with head and neck tumors: a pilot study." J Biomed Opt **11**(6): 064021.
- Taroni, P., A. Pifferi, A. Torricelli, D. Comelli and R. Cubeddu (2003). "In vivo absorption and scattering spectroscopy of biological tissues." Photochem Photobiol Sci **2**(2): 124-129.
- Torricelli, A., D. Contini, L. Spinelli, M. Caffini, A. Pifferi and R. Cubeddu (2011). Advanced Optical Methods for Functional Brain Imaging: Time-Domain Functional Near-Infrared Spectroscopy. Advances in Optical Imaging for Clinical Medicine, John Wiley & Sons, Inc.: 287-305.
- Tweddell, J. S., N. S. Ghanayem and G. M. Hoffman (2010). "Pro: NIRS is "standard of care" for postoperative management." Semin Thorac Cardiovasc Surg Pediatr Card Surg Annu **13**(1): 44-50.
- Tweddell, J. S., N. S. Ghanayem and G. M. Hoffman (2010). "Pro: NIRS is "Standard of Care" for Postoperative Management." Seminars in Thoracic and Cardiovascular Surgery: Pediatric Cardiac Surgery Annual **13**(1): 44-50.
- Wang, H. W., M. E. Putt, M. J. Emanuele, D. B. Shin, E. Glatstein, A. G. Yodh and T. M. Busch (2004). "Treatment-induced changes in tumor oxygenation predict photodynamic therapy outcome." Cancer Res **64**(20): 7553-7561.
- Wray, S., M. Cope, D. T. Delpy, J. S. Wyatt and E. O. R. Reynolds (1988). "Characterization of the near infrared absorption spectra of cytochrome aa3 and haemoglobin for the non-invasive monitoring of cerebral oxygenation." Biochimica et Biophysica Acta (BBA) - Bioenergetics **933**(1): 184-192.
- Yeganeh, H. Z., V. Toronov, J. T. Elliott, M. Diop, T.-Y. Lee and K. St. Lawrence (2012). "Broadband continuous-wave technique to measure baseline values and changes in the tissue chromophore concentrations." Biomed. Opt. Express **3**(11): 2761-2770.
- Yu, Y., N. Liu, A. Sassaroli and S. Fantini (2009). "Near-infrared spectral imaging of the female breast for quantitative oximetry in optical mammography." Appl Opt **48**(10): D225-235.

Chapter 2

Photon Migration in Turbid Media

2.1. Diffusion Theory

Starting from the radiative transfer equation (RTE) in transport theory, which describes light propagation in random media, photon migration in highly scattering media (such as biological tissues) can be approximated by the diffusion equation (DE). Letting $\mu_a(\mathbf{r})$ and $\mu'_s(\mathbf{r})$ represent the absorption and the reduced scattering coefficients, respectively, and $D(\mathbf{r}) = 1/(3\mu'_s)$ the diffusion coefficient in a medium as a function of position vector \mathbf{r} , the frequency-domain DE for the photon fluence rate $\Phi(\mathbf{r}, \omega)$ (in units of photons per unit area per unit time) due to an intensity modulated point source, is given by (Fishkin and Gratton 1993):

$$\nabla \cdot [D(\mathbf{r}) \nabla \Phi(\mathbf{r}, \omega)] - \left[\mu_a(\mathbf{r}) + i \frac{\omega}{c} \right] \Phi(\mathbf{r}, \omega) = -P(\omega) \delta(\mathbf{r}), \quad (2.1)$$

where c is the speed of light in the media, $\delta(\mathbf{r})$ is the Dirac delta function that represents a point-like photon source, and P is the frequency-dependent source power (photons/sec). Equation (2.1) reduces to the continuous wave (CW) DE by setting the angular modulation frequency (ω) to zero. Analytical solutions of the DE have been developed and reported in the literature in the time domain (Dayan *et al.* 1992; Kienle *et al.* 1998;

Tualle *et al.* 2000; Martelli *et al.* 2003; Liemert and Kienle 2010) , frequency domain (Fishkin and Gratton 1993; Kienle *et al.* 1998; Liemert and Kienle 2010), and CW (Dayan *et al.* 1992; Liemert and Kienle 2010) for homogenous (Fishkin and Gratton 1993), two-layered (Dayan *et al.* 1992; Kienle *et al.* 1998; Tualle *et al.* 2000; Martelli *et al.* 2003) and N-layered (Liemert and Kienle 2010) media. Other solutions of the DE for regularly bounded geometries have also been reported (Arridge *et al.* 1992). In this work, we have used solutions in the frequency domain for both homogenous media (as given in Fishkin and Gratton, 1993) and two-layered media (as given in Kienle *et al.*, 1998 for planar geometry, and Liemert and Kienle, 2010 for cylindrical geometry), therefore we shall summarize these solutions in the subsections below.

2.2. Solutions to the Diffusion Equation for homogenous media

2.2.1. Infinite Boundary Conditions

In the infinite geometry both the illumination (*i.e.* source) and the collection (*i.e.* detection) points are positioned inside the medium, where the diffused intensity is generated and detected only within the diffusing medium avoiding any complications due to boundary conditions. The measurement scheme employed in infinite geometry is illustrated in figure 2.1.

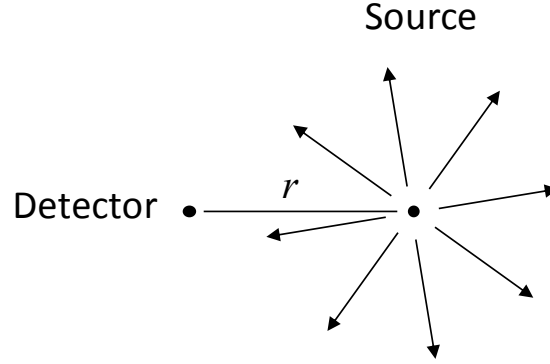


Figure 2.1. Infinite geometry arrangement, wherein the source and the detector, separated by a distance r , are positioned inside the diffuse medium.

For a source term described by: $q(\mathbf{r}, \omega, t) = \delta(\mathbf{r})P(\omega) \exp(i\omega t)$ in the frequency-domain (FD), where \mathbf{r} and t are the spatial and temporal variables, respectively, the complex fluence rate at the point of observation in an unbounded (*i.e.* infinite) homogeneous medium is given by (Fishkin and Gratton 1993):

$$\Phi(r, \omega) = \frac{P(0)}{4\pi Dr} \cdot \exp\left[-r\left(\frac{\mu_a}{D}\right)^{1/2}\right] + \frac{P(\omega)}{4\pi Dr} \cdot \exp\left[-\frac{r}{\sqrt{Dc}} \sqrt{\mu_a c + i\omega}\right], \quad (2.2)$$

where r is the distance between the point source and the point of observation. Note that Eq. (2.2) is the solution of Eq. (2.1) for a homogeneous unbounded medium. Three components of the fluence rate can be extracted from Eq. (2.2), namely the steady-state, direct current (DC or CW) term, the alternating current (AC) amplitude, and the phase (PH) of the oscillatory term, given by:

$$\text{DC} = \frac{P(0)}{4\pi Dr} \cdot \exp\left[-r\left(\frac{\mu_a}{D}\right)^{1/2}\right], \quad (2.3)$$

$$AC = \left| \frac{P(\omega)}{4\pi D r} \cdot \exp \left[-\frac{r}{\sqrt{Dc}} \sqrt{\mu_a c + i\omega} \right] \right|, \quad (2.4)$$

$$PH = \text{Arg} \left(\frac{P(\omega)}{4\pi D r} \cdot \exp \left[-\frac{r}{\sqrt{Dc}} \sqrt{\mu_a c + i\omega} \right] \right). \quad (2.5)$$

In the infinite geometry, the following expressions are linearly dependent on r in the following form (Fantini *et al.* 1994):

$$\ln(r \text{ DC}) = -r \left(\frac{\mu_a}{D} \right)^{1/2} + \ln \left(\frac{P(0)}{4\pi D} \right), \quad (2.6)$$

$$\ln(r \text{ AC}) = -r \left(\frac{c^2 \mu_a^2 + \omega^2}{c^2 D^2} \right)^{1/4} \cdot \cos \left[\frac{1}{2} \tan^{-1} \left(\frac{\omega}{c \mu_a} \right) \right] + \ln \left(\frac{AP(\omega)}{4\pi D} \right), \quad (2.7)$$

$$PH = r \left(\frac{c^2 \mu_a^2 + \omega^2}{c^2 D^2} \right)^{1/4} \cdot \sin \left[\frac{1}{2} \tan^{-1} \left(\frac{\omega}{c \mu_a} \right) \right]. \quad (2.8)$$

This linear dependence leads to an easy inversion procedure to evaluate μ_a and μ'_s using one of three ways:

- 1) The slopes of the straight lines of $\ln(r \text{ DC})$ and PH (S_{DC} and S_{PH} , respectively) as functions of r (Fishkin and Gratton 1993; Fantini *et al.* 1994):

$$\mu_a = \frac{\omega}{2c} \frac{S_{DC}}{S_{PH}} \left(\frac{S_{PH}^2}{S_{DC}^2} + 1 \right)^{-1/2}, \quad (2.9)$$

$$\mu'_s = \frac{S_{DC}^2}{3\mu_a}, \quad (2.10)$$

2) S_{PH} and the slope of the straight line of $\ln(r \text{ AC})$ as a function of r (S_{AC}):

$$\mu_a = \frac{\omega}{2c} \left(\frac{S_{\text{PH}}}{S_{\text{AC}}} - \frac{S_{\text{AC}}}{S_{\text{PH}}} \right), \quad (2.11)$$

$$\mu'_s = \frac{S_{\text{AC}}^2 - S_{\text{PH}}^2}{3\mu_a}, \quad (2.12)$$

3) The slopes, S_{DC} and S_{AC} :

$$\mu_a = \frac{\omega}{2c} \frac{S_{\text{DC}}}{S_{\text{AC}}} \left(\frac{S_{\text{AC}}^2}{S_{\text{DC}}^2} - 1 \right), \quad (2.13)$$

$$\mu'_s = \frac{S_{\text{DC}}^2}{3\mu_a}. \quad (2.14)$$

It is evident that the solution of DE for an unbounded “infinite” medium can only be considered for simulations or liquid phantom experiments, as it is physically not possible to position an illumination/detection paradigm inside solid media (*i.e.* solid phantoms or biological tissues). For all practical purposes, solutions of DE with semi-infinite boundary conditions are employed, wherein the illumination and collection is performed on the surface of the media under examination.

2.2.2. Semi-infinite Boundary Conditions

In the semi-infinite geometry, both the source and the detector points are positioned at the interface between air and the diffuse medium, wherein the interface extends indefinitely. An illustration of this measurement scheme is given in figure 2.2.

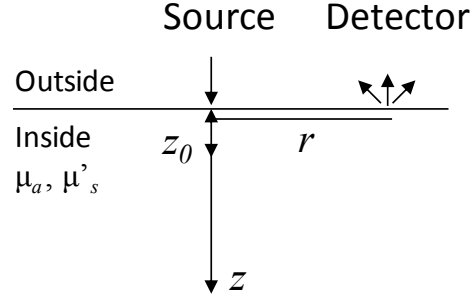


Figure 2.2. Semi-infinite geometry arrangement, wherein the source and the detector, separated by a distance r , are positioned flush with the surface of the diffuse medium. Here, z is the axis perpendicular to the medium's boundary, and z_0 ($\sim 1/\mu'_s$) is the depth of the effective (isotropic) source inside the scattering medium.

The solution of the DE requires boundary conditions and the model entails a single scattering source positioned at a depth $z_0 = 1/\mu'_s$ along the z -axis, the axis perpendicular to the medium's boundary, which is the depth of the effective isotropic source inside the scattering medium (Fantini *et al.* 1994). The complex photon fluence rate at the point of observation in a semi-infinite geometry is given by (Fantini *et al.* 1994):

$$\Phi(r, \omega) = \frac{P(0)}{4\pi D} \cdot \frac{\exp\left[-r_1 \left(\frac{\mu_a}{D}\right)^{1/2}\right]}{r_1} - \frac{\exp\left[-r_2 \left(\frac{\mu_a}{D}\right)^{1/2}\right]}{r_2} + \frac{P(\omega)}{4\pi D} \cdot \left\{ \frac{\exp\left[-r_1 \left(\frac{\mu_a}{2D}\right)^{1/2}\right]}{r_1} \xi - \frac{\exp\left[-r_2 \left(\frac{\mu_a}{2D}\right)^{1/2}\right]}{r_2} \xi \right\}, \quad (2.15)$$

Here, $\xi = (\sqrt{1+x^2} + 1)^{1/2} - i(\sqrt{1+x^2} - 1)^{1/2}$ with $x = \omega/v\mu_a$, $r_1 = \sqrt{z_0^2 + r^2}$ and

$r_2 = \sqrt{(z_0 + 2z_b)^2 + r^2}$, where $z_b = 2D_1 (1+R_{\text{eff}})/(1-R_{\text{eff}})$, and R_{eff} is the fraction of photons that are internally reflected at the mediums boundary based on (Haskell *et al.* 1994).

In this geometry, DE predicts the diffusely reflected intensity $R(r, \omega)$, which can be calculated either with photon flux at the boundary according to Fick's Law (Haskell *et al.* 1994):

$$R_{\text{flux}}(r) = D_1 \left. \frac{\partial}{\partial z} \Phi_1(r, z) \right|_{z=0} \quad (2.16)$$

or by a combination of photon fluence rate and flux, given by (Kienle and Patterson 1997):

$$R_{\text{fluence rate \& flux}}(r) = \eta_1 \Phi_1(r, z=0) + \eta_2 D_1 \left. \frac{\partial}{\partial z} \Phi_1(r, z) \right|_{z=0}, \quad (2.17)$$

where the coefficients η_1 and η_2 are chosen based on the refractive index mismatch between first layer and surrounding medium (Kienle and Patterson 1997). We have used Eq. (2.16) (*i.e.* Fick's law) for the calculation of $R(r)$ throughout this work, as we found it to be in better agreement with Monte Carlo simulations. The expression for the diffusely reflected intensity in the frequency domain for semi-infinite geometry is given by:

$$R(r, \omega) = \frac{P(\omega)}{4\pi} \left[z_0 \left(\frac{1}{r_1} + \mu_{\text{eff}} \right) \frac{\exp(-r_1 \mu_{\text{eff}})}{r_1^2} + (z_0 + 2z_b) \left(\frac{1}{r_2} + \mu_{\text{eff}} \right) \frac{\exp(-r_2 \mu_{\text{eff}})}{r_2^2} \right] \quad (2.18)$$

where $\mu_{\text{eff}} = [(\mu_a c + i \omega)/Dc]^{1/2}$. In this scheme, AC and PH terms are obtained by:

$$AC = |R(r)| \quad (2.19)$$

$$PH = \text{Arg}[R(r)]. \quad (2.20)$$

The linear relationships [given in Eqs. (2.6–2.8)] for infinite geometry do not strictly hold for semi-infinite geometry, therefore their semi-infinite counterparts have been reformulated (Fantini *et al.* 1994). Under this formulation, Eq. (2.9–2.14) are still valid with the assumption that the slopes of AC and DC are defined as $S_{AC} = \ln(r^2 AC)$, and $S_{DC} = \ln(r^2 DC)$, respectively. However these expressions work well only if the condition $r \mu_{\text{eff}} \gg 1$ is satisfied. For this reason, usually a nonlinear inversion procedure is used to retrieve the optical properties. In Appendix A, I provide results on Monte Carlo simulated data, where the performance of the semi-infinite geometry approximations is compared against a nonlinear fitting procedure.

2.3. Solutions to the Diffusion Equation for Two-Layered Media

We have implemented two separate solutions of the DE for two-layered media: First, the solution using the Fourier transform formalism for the planar geometry (*i.e.* semi-infinite regime), given in (Kienle *et al.* 1998), and second, the improved solution, which was developed in the cylindrical geometry, given in (Liemert and Kienle 2010). The latter solution (Liemert and Kienle 2010) was used for the analysis presented in the phantom and human studies (Chapter 8), because it was found to be computationally faster and more robust at large source-detector separations ($r > 30$ mm) and high reduced scattering coefficients ($\mu'_s > 1$ mm⁻¹). I provide a description of these solutions in the following subsections.

2.3.1. Solution in a Planar Geometry

An illustration of the measurement scheme in the planar geometry is shown in figure 2.3.

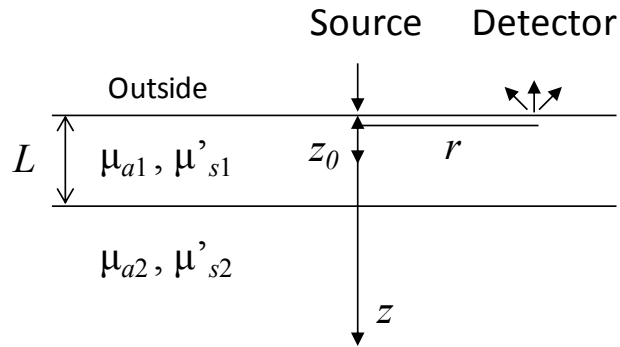


Figure 2.3. Two-layered planar geometry arrangement, wherein the top layer (layer 1) is infinitely long, having a finite thickness (L); and the bottom layer (layer 2) is semi-infinite. Optical coefficients μ_{ak} and μ'_{sk} represent the k^{th} layer ($k = 1$ or 2) properties.

The general solution of the DE for two-layered media for the planar geometry is derived in the frequency-domain by carrying out a transverse spatial Fourier transform (with respect to the variables x and y) solving the new partial differential equation obtained and finally “transforming back” into the spatial coordinates. The solution of the partial differential equation obtained after the transverse spatial Fourier transform is given by (Kienle *et al.* 1998):

$$\Phi_1(z, s) = \frac{\sinh[\alpha_1(z_b + z_0)]}{D_1\alpha_1} \left\{ \frac{D_1\alpha_1 \cosh[\alpha_1(L - z)] + D_2\alpha_2 \sinh[\alpha_1(L - z)]}{D_1\alpha_1 \cosh[\alpha_1(L + z_b)] + D_2\alpha_2 \sinh[\alpha_1(L + z_b)]} \right\} - \frac{\sinh[\alpha_1(z_0 - z)]}{D_1\alpha_1} \quad (2.21)$$

$$\Phi_2(z, s) = \frac{\sinh[\alpha_1(z_b + z_0)] \exp[\alpha_2(L - z)]}{D_1\alpha_1 \cosh[\alpha_1(L + z_b)] + D_2\alpha_2 \sinh[\alpha_1(L + z_b)]}, \quad (2.22)$$

where Φ_k and D_k represent the photon fluence rate and the diffusion coefficient in the k^{th} layer of the medium (i.e. $k = 1$ or 2 for a two-layered medium). Here, L represents first

layer thickness, $\alpha_k = \sqrt{\frac{\mu_{ak}}{D_k} + s_n^2 + \frac{i\omega}{D_k c}}$, $s = \sqrt{s_1^2 + s_2^2}$ is the radial spatial frequency

variable, and s_1 and s_2 are the spatial frequency variables along x and y , respectively. The fluence rates are evaluated in the spatial domain by the following (Kienle *et al.* 1998):

$$\Phi_k(\mathbf{r}, z) = \frac{1}{(2\pi)} \int_0^\infty \Phi_k(z, s) s J_0(sr) ds, \quad (2.23)$$

where J_0 is the Bessel function of first kind and order 0. Eq. (2.23) can then be used in Eqs. (2.16) or (2.17) to evaluate the photon reflectance. On a computer, real arithmetic is

not exact due to finite precision. To avoid numerical errors encountered in performing the integration in Eq. (2.23), limiting forms of these expressions have been developed.

2.3.2. Solution in a Cylindrical Geometry

An illustration of the measurement scheme in the cylindrical geometry is provided in figure 2.4.

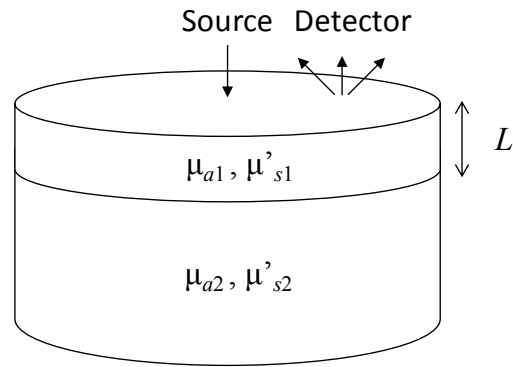


Figure 2.4. Two-layered cylindrical geometry arrangement, wherein both the top layer (layer 1) and the bottom layer are confined by the radius of the cylinder. Layer 1 has a finite thickness (L); and layer 2 is infinitely thick. Optical coefficients μ_{ak} and μ'_{sk} represent the k^{th} layer ($k = 1$ or 2) properties.

For a point source that is incident onto the center of a layered cylindrical medium, the general solution of the two-layered DE in cylindrical coordinates (ρ, θ, z) is given by (Liemert and Kienle 2010):

$$\hat{\Phi}_k(\mathbf{r}, \omega) = \frac{1}{\pi a'^2} \sum_{n=1}^{\infty} G_k(s_n, z, \omega) J_0(s_n \rho) J_1^{-2}(a' s_n), \quad (2.24)$$

where $\hat{\Phi}_k$ is the photon fluence in the k^{th} layer of the medium, s_n are the positive roots of the 0-order Bessel function of first kind divided by $a' = a + z_b$, (where a is the radius of the cylinder), J_m is the Bessel function of first kind and order m . Here, G_1 is defined in the following form (Liemert and Kienle 2010):

$$G_1(s_n, z, \omega) = \frac{\exp(-\alpha_1|z - z_0|) - \exp[\alpha_1(z + z_0 + 2z_b)]}{2D_1\alpha_1} + \frac{\sinh[\alpha_1(z_0 + z_b)]\sinh[\alpha_1(z_0 + z_b)]}{D_1\alpha_1 \exp[\alpha_1(l_1 + z_b)]} \cdot (2.25)$$

$$\times \frac{D_1\alpha_1 - D_2\alpha_2}{D_1\alpha_1 \cosh[\alpha_1(L - z_b)] + D_2\alpha_2 \sinh[\alpha_1(L - z_b)]}$$

In the case of two-layers, as opposed to the homogenous case, the inverse problem becomes much more complicated due to the increased number of unknowns. These unknowns are the absorption and reduced scattering coefficients of layer 1 (μ_{a1} , μ'_{s1}) and layer 2 (μ_{a2} , μ'_{s2}), the thickness of layer 1 (L), and a multiplicative AC factor (AF) and an additive phase term introduced by the measurement apparatus. The phase term can be neglected by considering the differences at different source-detector separations [for instance, $\text{PH}(r_2) - \text{PH}(r_1)$]. Unlike the homogenous solution, analytical approximations to address the inverse problem do not exist. The problem requires nonlinear fitting procedures on the measured quantities (PH and either AC or DC as a function of r). I provide a description of the inversion procedures used in this work in Chapter 3.

References for Chapter 2

- Arridge, S. R., M. Cope and D. T. Delpy (1992). "The theoretical basis for the determination of optical pathlengths in tissue: temporal and frequency analysis." Phys Med Biol **37**(7): 1531-1560.
- Dayan, I., S. Havlin and G. H. Weiss (1992). "Photon Migration in a Two-layer Turbid Medium a Diffusion Analysis." Journal of Modern Optics **39**(7): 1567-1582.
- Fantini, S., M. A. Franceschini, J. B. Fishkin, B. Barbieri and E. Gratton (1994). "Quantitative determination of the absorption spectra of chromophores in strongly scattering media: a light-emitting-diode based technique." Appl Opt **33**(22): 5204-5213.
- Fantini, S., M. A. Franceschini and E. Gratton (1994). "Semi-infinite-geometry boundary problem for light migration in highly scattering media: a frequency-domain study in the diffusion approximation." J. Opt. Soc. Am. B **11**(10): 2128-2138.
- Fishkin, J. B. and E. Gratton (1993). "Propagation of photon-density waves in strongly scattering media containing an absorbing semi-infinite plane bounded by a straight edge." J Opt Soc Am A **10**(1): 127-140.
- Haskell, R. C., L. O. Svaasand, T. T. Tsay, T. C. Feng, M. S. McAdams and B. J. Tromberg (1994). "Boundary conditions for the diffusion equation in radiative transfer." J Opt Soc Am A Opt Image Sci Vis **11**(10): 2727-2741.
- Kienle, A. and M. S. Patterson (1997). "Improved solutions of the steady-state and the time-resolved diffusion equations for reflectance from a semi-infinite turbid medium." J Opt Soc Am A Opt Image Sci Vis **14**(1): 246-254.
- Kienle, A., M. S. Patterson, N. Dognitz, R. Bays, G. Wagninures and H. van den Bergh (1998). "Noninvasive determination of the optical properties of two-layered turbid media." Appl Opt **37**(4): 779-791.
- Liemert, A. and A. Kienle (2010). "Light diffusion in a turbid cylinder. II. Layered case." Opt Express **18**(9): 9266-9279.
- Liemert, A. and A. Kienle (2010). "Light diffusion in N-layered turbid media: frequency and time domains." J Biomed Opt **15**(2): 025002.
- Liemert, A. and A. Kienle (2010). "Light diffusion in N-layered turbid media: steady-state domain." J Biomed Opt **15**(2): 025003.
- Martelli, F., A. Sassaroli, S. Del Bianco, Y. Yamada and G. Zaccanti (2003). "Solution of the time-dependent diffusion equation for layered diffusive media by the eigenfunction method." Phys Rev E Stat Nonlin Soft Matter Phys **67**(5 Pt 2): 056623.
- Tualle, J. M., J. Prat, E. Tinet and S. Avrillier (2000). "Real-space Green's function calculation for the solution of the diffusion equation in stratified turbid media." J Opt Soc Am A Opt Image Sci Vis **17**(11): 2046-2055.

Chapter 3

Cerebral Oximetry with NIRS

In this chapter, I provide a thorough literature review about NIRS techniques in the context of brain spectroscopy and imaging. I describe current strategies with an emphasis on the role of absolute NIRS measurements. Finally, I describe the problem shared by non-invasive optical brain imaging techniques, namely the extracerebral tissue contamination of the optical signals, which is the exact topic of interest of this work.

3.1. Background and Clinical Significance

Over the past several years, NIRS has seen an increasing appeal in the clinical realm. This has given rise to commercial devices that perform non-invasive cerebral oximetry by providing an estimate of oxygen saturation of hemoglobin in the human head (variously termed tissue oxygenation index (TOI), tissue saturation index (TSI), regional oxygen saturation (rSO₂) and oxygen saturation (SO₂)) (for a review, see Wolf *et al.* 2007 (Wolf *et al.* 2007)). Currently explored applications of clinical relevance include monitoring post traumatic brain injury (Sekhon *et al.* 2012), ischemic stroke (Kellert *et al.* 2011), coronary bypass surgery (Murkin *et al.* 2007), and detecting, for instance, cardiopulmonary dysfunction (Heringlake *et al.* 2011), cerebral hemorrhage (Hintz *et al.* 1999), and impaired cerebral autoregulation (Wong *et al.* 2012). Despite the strong

indication that accurate real-time NIRS measurement of cerebral hemoglobin parameters could significantly improve critical patient care and routine clinical practice (Tweddell *et al.* 2010; Parnia *et al.* 2012; Sekhon *et al.* 2012), concerns remain on the reliability of the current methods particularly due to extracerebral tissue contamination of the NIRS signals (Hirsch *et al.* 2010; Davie and Grocott 2012).

3.2. Current Methods

In a common research paradigm, functional NIRS (fNIRS) approaches are employed to study hemodynamic and metabolic responses to brain activation, which involve measurements of relative changes of oxy- and deoxy-hemoglobin concentrations (Wolf *et al.* 2008; Leff *et al.* 2011; Ferrari and Quaresima 2012). Existing fNIRS strategies to partly account for extracerebral hemodynamic trends include devising task-based experimental protocols to inhibit systemic contaminants (Franceschini *et al.* 2003; Jaszewski *et al.* 2003; Boden *et al.* 2007; Yamada *et al.* 2012); averaging measured hemodynamic changes over multiple events (as employed by most fNIRS studies) (Saager *et al.* 2011); and performing two-distance measurements and fitting and regressing out detected near signals (i.e. near the point of illumination) from far signals (i.e. far from the point of illumination) (Saager and Berger 2005; Saager and Berger 2008; Yamada *et al.* 2009; Gregg *et al.* 2010; Saager *et al.* 2011). Other strategies employ methods such as adaptive filtering (Zhang *et al.* 2007; Zhang *et al.* 2009); principal component analysis (PCA) (Zhang *et al.* 2005; Franceschini *et al.* 2006; Virtanen *et al.* 2009); and independent component analysis (ICA) (Markham *et al.* 2009; Virtanen *et al.* 2009). Furthermore, computationally more sophisticated diffuse optical

tomography (DOT) methods feature volumetric mesh based modeling of the human head with the aim of localizing measured hemodynamic changes under the assumption that underlying tissue is homogenous (Bluestone *et al.* 2001; Gibson and Dehghani 2009; Koch *et al.* 2010; Habermehl *et al.* 2012) or layered (Zeff *et al.* 2007).

While addressing the extracerebral contamination to some degree, fNIRS studies do not perform a baseline correction of measured dynamic changes (i.e. measured changes in optical coefficients divided by baseline/resting state optical coefficients). DOT studies recognize the importance of baseline values and employ absolute baseline/resting optical coefficients in their forward modeling (Bluestone *et al.* 2001; Zeff *et al.* 2007); however these studies typically rely on assumed values from the literature, thus neglecting inter-subject and intra-subject variability in these parameters. Relative measurements such as those typically employed in fNIRS lack the ability to provide information about the baseline state of the brain that result from baseline cerebral blood flow, blood volume, and metabolic rate of oxygen. Absolute NIRS measurements of the concentration and saturation of hemoglobin in brain tissue can fill this gap.

3.3. Implications

Absolute NIRS measurements found prominent applications in the longitudinal monitoring of infant brain development (Franceschini *et al.* 2007; Tina *et al.* 2009) as well as in the detection of anomalies, for instance, led by brain injury (Grant *et al.* 2009) and respiratory distress (Lemmers *et al.* 2006). Absolute brain oximetry (namely, measurement of StO₂ in absolute terms) was predicted to become a way for clinicians to

more quickly and noninvasively identify infants and children with altered levels of cerebral and/or somatic tissue oxygenation (Drayna *et al.* 2011).

Despite the success in animal and infant human studies, translation of such methods to adult human brain remains a challenge. Relatively large extracerebral scalp-cortex distance in adult humans (10–23 mm) (Okamoto *et al.* 2004; Stokes *et al.* 2005; Haeussinger *et al.* 2011) in comparison to rats (~1 mm) (Hallacoglu *et al.* 2011), piglets (~4 mm) (Fantini *et al.* 1999), or infants (5–11 mm) (Beauchamp *et al.* 2011) creates a problem for traditional light propagation models (*i.e.* homogenous models) to analyze the NIRS data. While the assumption of tissue homogeneity in the probed volume may be adequate for small animal or infant human brain imaging (Dehaes *et al.* 2011), and may yield robust and reproducible measurements in the adult human brain (Hallacoglu *et al.* 2012), dependence of the optical coefficients to source detector separations have been reported in several studies (Choi *et al.* 2004; Ohmae *et al.* 2006; Comelli *et al.* 2007; Gagnon *et al.* 2008; Dehaes *et al.* 2011; Hallacoglu *et al.* 2012), indicating a non-negligible depth dependence of the tissue composition. To overcome the limitation of homogenous models, two-layered models have been developed in both the time domain (Martelli *et al.* 2003) and frequency domain (Kienle *et al.* 1998), with experimental validations on tissue-mimicking layered phantoms (Pham *et al.* 2000; Alexandrakis *et al.* 2001; Ripoll *et al.* 2001; Martelli *et al.* 2004; Li *et al.* 2007; Pucci *et al.* 2010). *In vivo* application of these approaches to noninvasive brain measurements of absolute optical coefficients have also been investigated in the frequency domain (Choe *et al.* 2003; Choi *et al.* 2004) and time domain (Gagnon *et al.* 2008), and differences with respect to homogenous assumption have been measured in experimental (Choe *et al.* 2003) and

simulation based (Gagnon *et al.* 2008) data. For instance, Gagnon *et al.* (Gagnon *et al.* 2008) showed that the homogeneous model underestimated the absolute hemoglobin concentrations in the brain by about 30% (Fig. 1 in their paper). Choe *et al.* (Choe *et al.* 2003) measured absolute changes in StO_2 during hypoxia (i.e baseline minus hypoxic state) using homogenous and two-layered models and reported that homogenous model underestimated this quantity by up to 90% (true values were determined using a hemoximeter). The advantages of using two-layer models over homogenous models in brain imaging have been demonstrated through the works discussed above; however widespread adoption of such approaches has not occurred due to limitations. These limitation include requirement of complementary MRI measurements (Choi *et al.* 2004; Gagnon *et al.* 2008) or invasive means (Choe *et al.* 2003) to measure top layer thickness (cortex depth) and inability to measure first and second layer optical properties simultaneously.

References for Chapter 3

- Alexandrakis, G., D. R. Busch, G. W. Faris and M. S. Patterson (2001). "Determination of the optical properties of two-layer turbid media by use of a frequency-domain hybrid monte carlo diffusion model." *Appl Opt* **40**(22): 3810-3821.
- Beauchamp, M. S., M. R. Beurlot, E. Fava, A. R. Nath, N. A. Parikh, Z. S. Saad, H. Bortfeld and J. S. Oghalai (2011). "The Developmental Trajectory of Brain-Scalp Distance from Birth through Childhood: Implications for Functional Neuroimaging." *PLoS ONE* **6**(9): e24981.
- Bluestone, A., G. Abdoulaev, C. Schmitz, R. Barbour and A. Hielscher (2001). "Three-dimensional optical tomography of hemodynamics in the human head." *Opt Express* **9**(6): 272-286.
- Boden, S., H. Obrig, C. Kohncke, H. Benav, S. P. Koch and J. Steinbrink (2007). "The oxygenation response to functional stimulation: is there a physiological meaning to the lag between parameters?" *Neuroimage* **36**(1): 100-107.
- Choe, R., T. Durduran, G. Yu, M. J. Nijland, B. Chance, A. G. Yodh and N. Ramanujam (2003). "Transabdominal near infrared oximetry of hypoxic stress in fetal sheep brain in utero." *Proc Natl Acad Sci U S A* **100**(22): 12950-12954.
- Choi, J., M. Wolf, V. Toronov, U. Wolf, C. Polzonetti, D. Hueber, L. P. Safonova, R. Gupta, A. Michalos, W. Mantulin and E. Gratton (2004). "Noninvasive determination of the optical properties of adult brain: near-infrared spectroscopy approach." *J Biomed Opt* **9**(1): 221-229.
- Comelli, D., A. Bassi, A. Pifferi, P. Taroni, A. Torricelli, R. Cubeddu, F. Martelli and G. Zaccanti (2007). "In vivo time-resolved reflectance spectroscopy of the human forehead." *Appl Opt* **46**(10): 1717-1725.
- Davie, S. N. and H. P. Grocott (2012). "Impact of extracranial contamination on regional cerebral oxygen saturation: a comparison of three cerebral oximetry technologies." *Anesthesiology* **116**(4): 834-840.
- Dehaes, M., P. E. Grant, D. D. Sliva, N. Roche-Labarbe, R. Pienaar, D. A. Boas, M. A. Franceschini and J. Selb (2011). "Assessment of the frequency-domain multi-distance method to evaluate the brain optical properties: Monte Carlo simulations from neonate to adult." *Biomed Opt Express* **2**(3): 552-567.
- Drayna, P. C., T. J. Abramo and C. Estrada (2011). "Near-infrared spectroscopy in the critical setting." *Pediatr Emerg Care* **27**(5): 432-439; quiz 440-432.
- Fantini, S., D. Hueber, M. A. Franceschini, E. Gratton, W. Rosenfeld, P. G. Stubblefield, D. Maulik and M. R. Stankovic (1999). "Non-invasive optical monitoring of the newborn piglet brain using continuous-wave and frequency-domain spectroscopy." *Phys Med Biol* **44**(6): 1543-1563.
- Ferrari, M. and V. Quaresima (2012). "A brief review on the history of human functional near-infrared spectroscopy (fNIRS) development and fields of application." *Neuroimage* **63**(2): 921-935.
- Franceschini, M. A., S. Fantini, J. H. Thompson, J. P. Culver and D. A. Boas (2003). "Hemodynamic evoked response of the sensorimotor cortex measured noninvasively with near-infrared optical imaging." *Psychophysiology* **40**(4): 548-560.

- Franceschini, M. A., D. K. Joseph, T. J. Huppert, S. G. Diamond and D. A. Boas (2006). "Diffuse optical imaging of the whole head." J Biomed Opt **11**(5): 054007.
- Franceschini, M. A., S. Thaker, G. Themelis, K. K. Krishnamoorthy, H. Bortfeld, S. G. Diamond, D. A. Boas, K. Arvin and P. E. Grant (2007). "Assessment of infant brain development with frequency-domain near-infrared spectroscopy." Pediatr Res **61**(5 Pt 1): 546-551.
- Gagnon, L., C. Gauthier, R. D. Hoge, F. Lesage, J. Selb and D. A. Boas (2008). "Double-layer estimation of intra- and extracerebral hemoglobin concentration with a time-resolved system." J Biomed Opt **13**(5): 054019.
- Gibson, A. and H. Dehghani (2009). "Diffuse optical imaging." Philos Transact A Math Phys Eng Sci **367**(1900): 3055-3072.
- Grant, P. E., N. Roche-Labarbe, A. Surova, G. Themelis, J. Selb, E. K. Warren, K. S. Krishnamoorthy, D. A. Boas and M. A. Franceschini (2009). "Increased cerebral blood volume and oxygen consumption in neonatal brain injury." J Cereb Blood Flow Metab **29**(10): 1704-1713.
- Gregg, N. M., B. R. White, B. W. Zeff, A. J. Berger and J. P. Culver (2010). "Brain specificity of diffuse optical imaging: improvements from superficial signal regression and tomography." Front Neuroenergetics **2**.
- Habermehl, C., S. Holtze, J. Steinbrink, S. P. Koch, H. Obrig, J. Mehnert and C. H. Schmitz (2012). "Somatosensory activation of two fingers can be discriminated with ultrahigh-density diffuse optical tomography." Neuroimage **59**(4): 3201-3211.
- Haeussinger, F. B., S. Heinzl, T. Hahn, M. Schecklmann, A. C. Ehlis and A. J. Fallgatter (2011). "Simulation of near-infrared light absorption considering individual head and prefrontal cortex anatomy: implications for optical neuroimaging." PLoS ONE **6**(10): e26377.
- Hallacoglu, B., A. Sassaroli, S. Fantini and A. M. Troen (2011). "Cerebral perfusion and oxygenation are impaired by folate deficiency in rat: absolute measurements with noninvasive near-infrared spectroscopy." J Cereb Blood Flow Metab **31**(6): 1482-1492.
- Hallacoglu, B., A. Sassaroli, M. Wysocki, E. Guerrero-Berroa, M. Schnaider Beerli, V. Haroutunian, M. Shaul, I. H. Rosenberg, A. M. Troen and S. Fantini (2012). "Absolute measurement of cerebral optical coefficients, hemoglobin concentration and oxygen saturation in old and young adults with near-infrared spectroscopy." J Biomed Opt **17**(8): 081406-081401.
- Heringlake, M., C. Garbers, J. H. Kabler, I. Anderson, H. Heinze, J. Schon, K. U. Berger, L. Dibbelt, H. H. Sievers and T. Hanke (2011). "Preoperative cerebral oxygen saturation and clinical outcomes in cardiac surgery." Anesthesiology **114**(1): 58-69.
- Hintz, S. R., W. F. Cheong, J. P. van Houten, D. K. Stevenson and D. A. Benaron (1999). "Bedside imaging of intracranial hemorrhage in the neonate using light: comparison with ultrasound, computed tomography, and magnetic resonance imaging." Pediatr Res **45**(1): 54-59.
- Hirsch, J. C., J. R. Charpie, R. G. Ohye and J. G. Gurney (2010). "Near Infrared Spectroscopy (NIRS) Should Not Be Standard of Care for Postoperative

- Management." Seminars in Thoracic and Cardiovascular Surgery: Pediatric Cardiac Surgery Annual **13**(1): 51-54.
- Jaszewski, G., G. Strangman, J. Wagner, K. K. Kwong, R. A. Poldrack and D. A. Boas (2003). "Differences in the hemodynamic response to event-related motor and visual paradigms as measured by near-infrared spectroscopy." Neuroimage **20**(1): 479-488.
- Kellert, L., E. Martin, M. Sykora, H. Bauer, P. Gussmann, J. Diedler, C. Herweh, P. A. Ringleb, W. Hacke, T. Steiner and J. Bosel (2011). "Cerebral oxygen transport failure?: decreasing hemoglobin and hematocrit levels after ischemic stroke predict poor outcome and mortality: STroke: RelevAnt Impact of hemoGlobin, Hematocrit and Transfusion (STRAIGHT)--an observational study." Stroke **42**(10): 2832-2837.
- Kienle, A., M. S. Patterson, N. Dognitz, R. Bays, G. Wagninures and H. van den Bergh (1998). "Noninvasive determination of the optical properties of two-layered turbid media." Appl Opt **37**(4): 779-791.
- Koch, S. P., C. Habermehl, J. Mehnert, C. H. Schmitz, S. Holtze, A. Villringer, J. Steinbrink and H. Obrig (2010). "High-resolution optical functional mapping of the human somatosensory cortex." Front Neuroenergetics **2**: 12.
- Leff, D. R., F. Orihuela-Espina, C. E. Elwell, T. Athanasiou, D. T. Delpy, A. W. Darzi and G. Z. Yang (2011). "Assessment of the cerebral cortex during motor task behaviours in adults: a systematic review of functional near infrared spectroscopy (fNIRS) studies." Neuroimage **54**(4): 2922-2936.
- Lemmers, P. M., M. Toet, L. J. van Schelven and F. van Bel (2006). "Cerebral oxygenation and cerebral oxygen extraction in the preterm infant: the impact of respiratory distress syndrome." Exp Brain Res **173**(3): 458-467.
- Li, A., R. Kwong, A. Cerussi, S. Merritt, C. Hayakawa and B. Tromberg (2007). "Method for recovering quantitative broadband diffuse optical spectra from layered media." Appl Opt **46**(21): 4828-4833.
- Markham, J., B. R. White, B. W. Zeff and J. P. Culver (2009). "Blind identification of evoked human brain activity with independent component analysis of optical data." Hum Brain Mapp **30**(8): 2382-2392.
- Martelli, F., S. Del Bianco, G. Zaccanti, A. Pifferi, A. Torricelli, A. Bassi, P. Taroni and R. Cubeddu (2004). "Phantom validation and in vivo application of an inversion procedure for retrieving the optical properties of diffusive layered media from time-resolved reflectance measurements." Opt Lett **29**(17): 2037-2039.
- Martelli, F., A. Sassaroli, S. Del Bianco, Y. Yamada and G. Zaccanti (2003). "Solution of the time-dependent diffusion equation for layered diffusive media by the eigenfunction method." Phys Rev E Stat Nonlin Soft Matter Phys **67**(5 Pt 2): 056623.
- Murkin, J. M., S. J. Adams, R. J. Novick, M. Quantz, D. Bainbridge, I. Iglesias, A. Cleland, B. Schaefer, B. Irwin and S. Fox (2007). "Monitoring brain oxygen saturation during coronary bypass surgery: a randomized, prospective study." Anesth Analg **104**(1): 51-58.
- Ohmae, E., Y. Ouchi, M. Oda, T. Suzuki, S. Nobesawa, T. Kanno, E. Yoshikawa, M. Futatsubashi, Y. Ueda, H. Okada and Y. Yamashita (2006). "Cerebral hemodynamics evaluation by near-infrared time-resolved spectroscopy:

- correlation with simultaneous positron emission tomography measurements." *Neuroimage* **29**(3): 697-705.
- Okamoto, M., H. Dan, K. Sakamoto, K. Takeo, K. Shimizu, S. Kohno, I. Oda, S. Isobe, T. Suzuki, K. Kohyama and I. Dan (2004). "Three-dimensional probabilistic anatomical cranio-cerebral correlation via the international 10–20 system oriented for transcranial functional brain mapping." *Neuroimage* **21**(1): 99-111.
- Parnia, S., A. Nasir, C. Shah, R. Patel, A. Mani and P. Richman (2012). "A feasibility study evaluating the role of cerebral oximetry in predicting return of spontaneous circulation in cardiac arrest." *Resuscitation* **83**(8): 982-985.
- Pham, T. H., T. Spott, L. O. Svaasand and B. J. Tromberg (2000). "Quantifying the properties of two-layer turbid media with frequency-domain diffuse reflectance." *Appl Opt* **39**(25): 4733-4745.
- Pucci, O., V. Toronov and K. St Lawrence (2010). "Measurement of the optical properties of a two-layer model of the human head using broadband near-infrared spectroscopy." *Appl Opt* **49**(32): 6324-6332.
- Ripoll, J., V. Ntziachristos, J. P. Culver, D. N. Pattanayak, A. G. Yodh and M. Nieto-Vesperinas (2001). "Recovery of optical parameters in multiple-layered diffusive media: theory and experiments." *J Opt Soc Am A Opt Image Sci Vis* **18**(4): 821-830.
- Saager, R. and A. Berger (2008). "Measurement of layer-like hemodynamic trends in scalp and cortex: implications for physiological baseline suppression in functional near-infrared spectroscopy." *J Biomed Opt* **13**(3): 034017.
- Saager, R. B. and A. J. Berger (2005). "Direct characterization and removal of interfering absorption trends in two-layer turbid media." *J Opt Soc Am A Opt Image Sci Vis* **22**(9): 1874-1882.
- Saager, R. B., N. L. Telleri and A. J. Berger (2011). "Two-detector Corrected Near Infrared Spectroscopy (C-NIRS) detects hemodynamic activation responses more robustly than single-detector NIRS." *Neuroimage* **55**(4): 1679-1685.
- Sekhon, M. S., N. McLean, W. R. Henderson, D. R. Chittock and D. E. Griesdale (2012). "Association of hemoglobin concentration and mortality in critically ill patients with severe traumatic brain injury." *Crit Care* **16**(4): R128.
- Stokes, M. G., C. D. Chambers, I. C. Gould, T. R. Henderson, N. E. Janko, N. B. Allen and J. B. Mattingley (2005). "Simple metric for scaling motor threshold based on scalp-cortex distance: application to studies using transcranial magnetic stimulation." *J Neurophysiol* **94**(6): 4520-4527.
- Tina, L. G., A. Frigiola, R. Abella, B. Artale, G. Puleo, S. D'Angelo, C. Musmarra, P. Tagliabue, G. Li Volti, P. Florio and D. Gazzolo (2009). "Near Infrared Spectroscopy in healthy preterm and term newborns: correlation with gestational age and standard monitoring parameters." *Curr Neurovasc Res* **6**(3): 148-154.
- Tweddell, J. S., N. S. Ghanayem and G. M. Hoffman (2010). "Pro: NIRS is "standard of care" for postoperative management." *Semin Thorac Cardiovasc Surg Pediatr Card Surg Annu* **13**(1): 44-50.
- Virtanen, J., T. Noponen and P. Merilainen (2009). "Comparison of principal and independent component analysis in removing extracerebral interference from near-infrared spectroscopy signals." *J Biomed Opt* **14**(5): 054032.

- Wolf, M., M. Ferrari and V. Quaresima (2007). "Progress of near-infrared spectroscopy and topography for brain and muscle clinical applications." J Biomed Opt **12**(6): 062104.
- Wolf, M., G. Morren, D. Haensse, T. Karen, U. Wolf, J. Fauchère and H. Bucher (2008). "Near infrared spectroscopy to study the brain: an overview." Opto-Electronics Review **16**(4): 413-419.
- Wong, F. Y., R. Silas, S. Hew, T. Samarasinghe and A. M. Walker (2012). "Cerebral Oxygenation Is Highly Sensitive to Blood Pressure Variability in Sick Preterm Infants." PLoS ONE **7**(8): e43165.
- Yamada, T., S. Umeyama and K. Matsuda (2009). "Multidistance probe arrangement to eliminate artifacts in functional near-infrared spectroscopy." J Biomed Opt **14**(6): 064034.
- Yamada, T., S. Umeyama and K. Matsuda (2012). "Separation of fNIRS signals into functional and systemic components based on differences in hemodynamic modalities." PLoS ONE **7**(11): e50271.
- Zeff, B. W., B. R. White, H. Dehghani, B. L. Schlaggar and J. P. Culver (2007). "Retinotopic mapping of adult human visual cortex with high-density diffuse optical tomography." Proc Natl Acad Sci U S A **104**(29): 12169-12174.
- Zhang, Q., E. N. Brown and G. E. Strangman (2007). "Adaptive filtering for global interference cancellation and real-time recovery of evoked brain activity: a Monte Carlo simulation study." J Biomed Opt **12**(4): 044014.
- Zhang, Q., G. E. Strangman and G. Ganis (2009). "Adaptive filtering to reduce global interference in non-invasive NIRS measures of brain activation: how well and when does it work?" Neuroimage **45**(3): 788-794.
- Zhang, Y., D. H. Brooks, M. A. Franceschini and D. A. Boas (2005). "Eigenvector-based spatial filtering for reduction of physiological interference in diffuse optical imaging." J Biomed Opt **10**(1): 11014.

Chapter 4

Methods

4.1. Nonlinear Fitting Procedures

For the solutions of the diffusion equation (DE) in homogenous media in the frequency domain, the inversion procedure is easy. In fact, under certain conditions, approximations such as those presented in Chapter 2 are sufficient enough to retrieve the optical properties (as I have demonstrated in Appendix A). However, in the more sophisticated solutions, *i.e.* the two-layered solution, such approximations do not exist and nonlinear fitting procedures are necessary.

To solve the inverse problem of diffuse optical measurements, we implemented a Levenberg-Marquard optimization routine in Matlab (Mathworks Inc, Natick, MA) based on (Madsen *et al.* 2004) of the form:

$$\mathbf{x}^* = \arg \min_{\mathbf{x}} \{F(\mathbf{x})\}. \quad (4.1)$$

Here, \mathbf{x}^* is the result of the optimization, *i.e.* the best estimates of the unknown parameter vector \mathbf{x} , where:

$$\mathbf{x} = \begin{cases} [\mu_a, \mu'_s, AF]^T & \text{for homogenous media} \\ [\mu_{a1}, \mu'_{s1}, L, \mu_{a2}, \mu'_{s2}, AF]^T & \text{for twolayered media} \end{cases}$$

The best estimate of \mathbf{x} minimizes the cost function of the following form:

$$F(\mathbf{x}) = \frac{1}{2} \|\boldsymbol{\varepsilon}\|_2^2, \quad (4.2)$$

where, $\boldsymbol{\varepsilon}$ is the error vector composed of the difference between theoretical values and experimental (or simulated) values as:

$$\boldsymbol{\varepsilon} = \begin{bmatrix} \text{AC}_{Mod}(\mathbf{x}; r) \\ \text{PH}_{Mod}(\mathbf{x}; r) \end{bmatrix} - \begin{bmatrix} \text{AC}_{Exp}(r) \\ \text{PH}_{Exp}(r) \end{bmatrix}. \quad (4.3)$$

Here, AC_{Mod} and PH_{Mod} are the theoretical values yielded from either the homogenous or the two-layered model, AC_{Exp} and PH_{Exp} are the experimental values either from Monte Carlo simulations or measurements, and $\|\cdot\|_2$ represents the Euclidean norm. In order to employ the Levenberg-Marquardt algorithm, the calculation of the Jacobian matrix \mathbf{J} of the error vector with respect to the parameter vector is required. In the two-layered case, the jacobian is in the following form:

$$\mathbf{J} = \frac{\partial \boldsymbol{\varepsilon}}{\partial \{\boldsymbol{\mu}_{a1}, \boldsymbol{\mu}'_{s1}, L, \boldsymbol{\mu}_{a2}, \boldsymbol{\mu}'_{s2}, \text{AF}\}}(\mathbf{x}). \quad (4.4)$$

The solution is then obtained by updating \mathbf{x} at each iteration as: $\mathbf{x}^{n+1} = \mathbf{x}^n + \mathbf{h}$, where \mathbf{h} is obtained by solving the following linear system:

$$(\mathbf{J}^T \mathbf{J} + \psi \mathbf{D}) \mathbf{h} = -\mathbf{J}^T \boldsymbol{\varepsilon} \text{ with } \psi \geq 0, \quad (4.5)$$

where ψ is a damping parameter affecting the size and direction of \mathbf{h} and found via an appropriate line search algorithm (Madsen *et al.* 2004). Once the optimal fit parameters were determined, parameter statistics were computed for the converged solution using weight values equal to the mean square measurement error (namely, errors on AC and PH). The asymptotic standard parameter errors were computed by considering:

$\sigma_x = \sqrt{\text{diag}[\mathbf{J}^T \mathbf{W} \mathbf{J}]}$, where $[\mathbf{J}^T \mathbf{W} \mathbf{J}]$ is the covariance matrix, \mathbf{J} is the Jacobian matrix,

and \mathbf{W} is the weighting matrix, which is constructed as a diagonal matrix with elements representing the inverse square of the measurement errors (Press *et al.* 1992). Here, $\text{diag}[\mathbf{J}^T \mathbf{W} \mathbf{J}]$ represents a vector constructed with the diagonal elements of the covariance matrix. In all measurements, we considered the measurement errors to be 0.1° and 2% on each PH and AC datum, respectively, which are typical error values of the measurement apparatus used in this work (Fantini and Franceschini 2002).

4.2. Monte Carlo Simulations

Monte Carlo (MC) is a stochastic (probabilistic) method that is frequently used for modeling the behavior of light in biological tissue. The term “Monte Carlo” refers to a technique first proposed in the 1940s (Metropolis and Ulam 1949) to use a stochastic simulation to model physical processes. Indeed, MC method uses statistical measures of empirically gathered values to generate model datum and through iterations it generates a complete data set.

Throughout this work, MC simulations were performed based on Sassaroli *et al.* 2010 (Sassaroli *et al.* 2010) for the validation of the forward models and testing of the inversion procedures. A block diagram of the MC code is given in figure 4.1. Briefly, each injected photon is “followed” in its path through the medium until it is either detected, or lost through the medium’s boundary. Moreover the photon is abandoned if its total pathlength (travelled in the medium) exceeds a fixed threshold (chosen differently for each source-detector distance). This corresponds to about three-four decades of the temporal point spread function. We note that the “late” photons, even if detected, do not

contribute to the calculated parameters (DC, AC, PH). The simulations are typically run until 10000 photons are detected in each receiver. This number guarantees an accuracy in the DC estimated values of 1% for non-absorbing media (as typically chosen for our simulations). Scaling relationships based on the microscopic Beer-Lambert (Tsuchiya 2001) law are applied in order to scale the results to an arbitrary value of the absorption coefficient. Typically, multiple (around 10) independent simulations are run in order to estimate errors in the DC, AC and PH data.

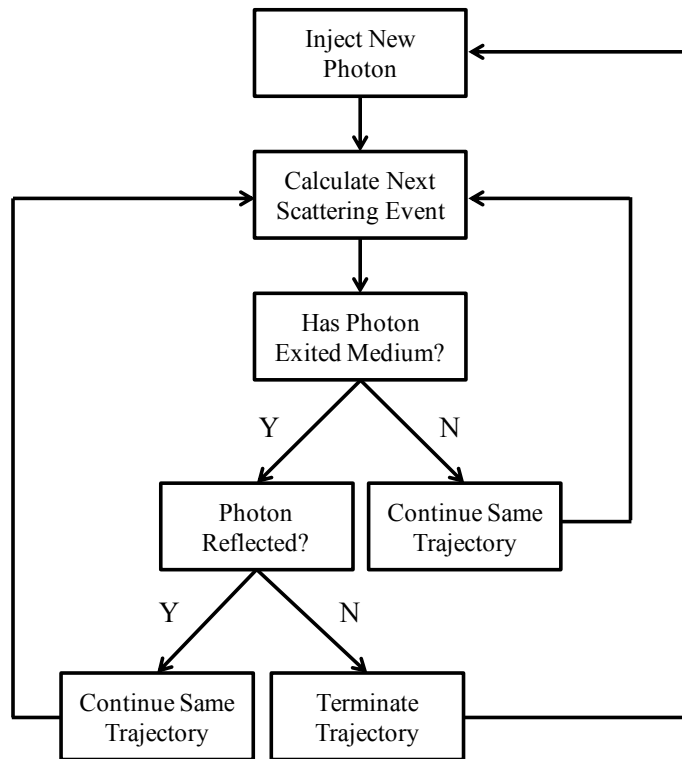


Figure 4.1. Block diagram of the Monte Carlo (MC) code that was used throughout this work.

4.3. Instrumentation for frequency-domain NIRS

As I have introduced in Chapter 1, near-infrared spectroscopy (NIRS) instruments operate in one of three different modes (namely, continuous wave, time domain or frequency domain). In this chapter, I focus on frequency domain (FD) mode, as it is the modality that was used in all of our experimental approaches. Below, I provide some details about the components and the principle of operation of FD NIRS instruments and describe a specific FD NIRS instrument for tissue spectroscopy and imaging that was used in this work.

Frequency domain NIRS instruments rely on intensity modulated emission and specially devised detection processes. In the emission side, typically, laser diodes are employed, which are intensity modulated by means of an oscillating current source. Fast response time of laser diodes allow modulation frequencies reaching up to the gigahertz range (Fantini and Franceschini 2002). Other advantages of employing laser diodes in modulated spectroscopy/imaging applications include their cost-effectiveness, ease of modulation, effectiveness in coupling to fiber optics, and availability in various discrete wavelengths.

In the detection end, depending on the application, optical detectors such as photomultiplier tubes (PMTs), microchannel plate photomultipliers (MCP-PMT), avalanche photodiodes (APD), or charge coupled device (CCD) cameras are employed. Briefly, PMTs are vacuumed phototubes with very high sensitivity to light in the visible and in the near-infrared (up to about 1,000 nm) range of the electromagnetic spectrum. Photomultiplier tubes feature multiple dynode stages for step-wise amplification of the

incident current generated by the detected light. For internal frequency down-conversion, their gain is modulated by a signal applied to the second dynode of the amplification stages. Their rapid rise time (in the nanosecond range), allows for modulation bandwidths of several hundred megahertz. Micro-channel plates PMTs have similar features with the additional advantage of faster rise times, which allows modulation bandwidths of the order of gigahertz (Charbonneau *et al.* 1992). In MC-PMTs frequency down conversion is performed either by modulating the grid or through external electronic mixers (Fishkin *et al.* 1996). Avalanche photodiodes feature comparable rise times to MC-PMTs and they require electronic mixers for the frequency down conversion (Louis *et al.* 1988). Finally, CCD cameras with modulated image intensifiers are commonly used in frequency-domain spectroscopy, microscopy, and imaging applications (Fantini and Franceschini 2002). The frequency down conversion in CCD cameras are performed by applying a modulation signal to the photocathode or to the microchannel plate of the image intensifier (Szmecinski *et al.* 1994).

Frequency-domain spectroscopy can be implemented in several different instrumental schemes, including heterodyne or homodyne techniques. In figure 4.2, I provide a block diagram that illustrates the principle behind the heterodyne detection technique. Briefly, the intensity of the light source is modulated by a radio-frequency (RF) synthesizer 1 with frequency f (hundreds of megahertz) and applied into the biological tissue. This leads to an amplitude attenuation and shift in the phase of f . The beating between the detected signal from the tissue and the down conversion signal at frequency $f + \Delta f$, generated by RF Synthesizer 2, determines a low frequency component Δf (typically, of the order of kilohertz) that is filtered by a low pass filter (LPF),

converted to digital by Analog to Digital Converter (ADC), and fast Fourier transformed (FFT) to yield the peak amplitude (AC), average amplitude (DC) and phase shift (PH). The phase information is contained within the beating signal because the RF Synthesizers 1 and 2 are synchronized (Fantini and Franceschini 2002).

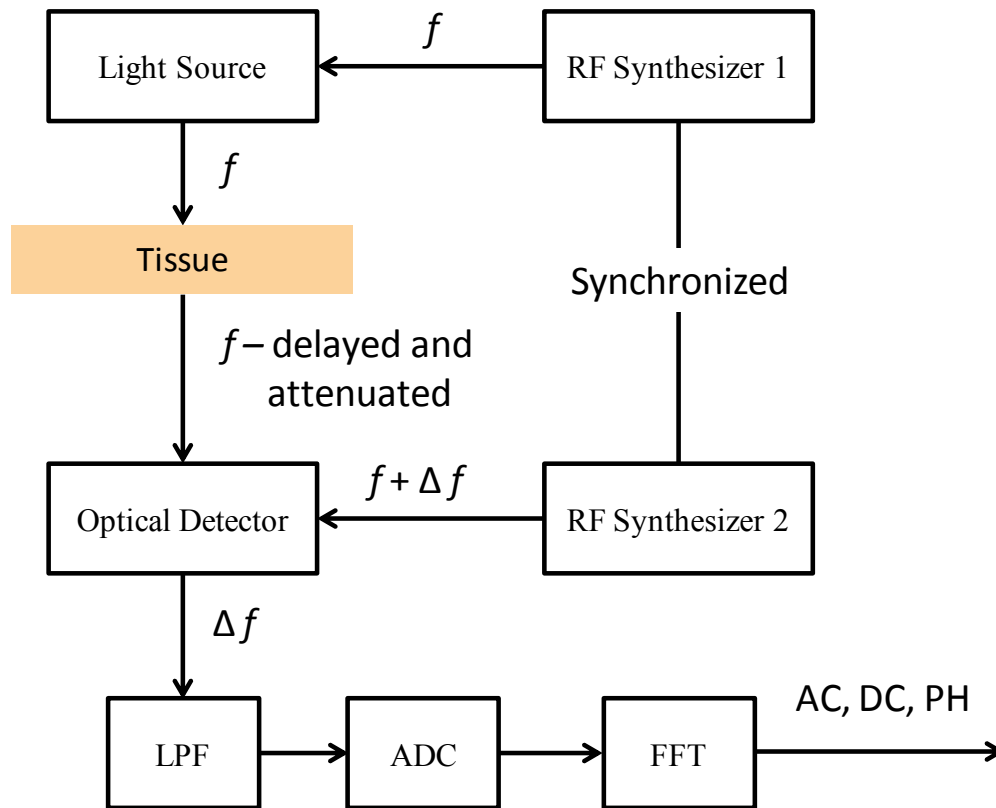


Figure 4.2. Block diagram of the heterodyne detection scheme and the generation of the readings for peak amplitude (AC), average amplitude (DC) and phase shift (PH). The intensity of the light source is modulated by a radio-frequency (RF) synthesizer with frequency f , typically around ~ 100 MHz and applied into the medium (in this case biological tissue). The beating between the detected signal at frequency f and the down conversion signal at frequency $f + \Delta f$, generated by RF Synthesizer 2, determines a low frequency component Δf that is filtered by a low pass filter (LPF), converted to digital by Analog to Digital Converter (ADC), and fast Fourier transformed (FFT) to yield the AC, DC and PH. The phase information is contained in the signal because the RF Synthesizer 1 and 2 are synchronized.

Similar to heterodyne detection, homodyne detection technique also yields AC, DC, and PH, however this technique does not perform down conversion of the RF signal. Further details about these techniques can be found elsewhere (Collett *et al.* 1987).

All experimental approaches that were carried out in the framework of this thesis were performed using a frequency domain instrument (OxiplexTS, ISS Inc, Champaign, IL). The instrument features sixteen laser diodes, with emissions wavelengths of 690 nm ($\times 8$) (Hitachi HL6738MG) and 830 nm ($\times 8$) (Hitachi LTO15MDO), and two PMT (Hamamatsu Photonics R928) detectors. The laser diode light sources are intensity modulated at a frequency of 110 MHz. In the typical experimental setup, modulated light from the laser diodes are delivered to the medium of interest by means of optical fibers. The optical power at the end of the illumination optical fibers are typically ~ 2 mW. On the detection end, another optical fiber (generally a fiber bundle) is used to deliver the light to a PMT, whose gain function is modulated at a slightly different frequency ($110 \text{ MHz} + 5 \text{ kHz}$) than that of the intensity modulation of the light sources, giving rise to a beating signal of 5 kHz, which is sent to the computer for analysis. The built in Fast-Fourier-Transform algorithm computes the phase (relative to a reference signal) (PH), the average intensity (DC), and the amplitude of the intensity oscillations (AC) of the detected light as described in the previous section. Further details of such frequency-domain system can be found elsewhere (Fantini and Franceschini 2002).

References for Chapter 4

- Charbonneau, S., L. B. Allard, J. F. Young, G. Dyck and B. J. Kyle (1992). "2-dimensional time-resolved imaging with 100-ps resolution using a resistive anode photomultiplier tube." Review of Scientific Instruments **63**(11): 5315-5319.
- Collett, M. J., R. Loudon and C. W. Gardiner (1987). "Quantum Theory of Optical Homodyne and Heterodyne Detection." Journal of Modern Optics **34**(6-7): 881-902.
- Fantini, S. and M. A. Franceschini (2002). Frequency-domain techniques for tissue spectroscopy and imaging. Handbook of Optical Biomedical Diagnostics. V. V. Tuchin. Bellingham, WA, SPIE Press.
- Fishkin, J. B., S. Fantini, M. J. vandeVen and E. Gratton (1996). "Gigahertz photon density waves in a turbid medium: Theory and experiments." Phys Rev E Stat Phys Plasmas Fluids Relat Interdiscip Topics **53**(3): 2307-2319.
- Louis, T., G. H. Schatz, P. Kleinbolting, A. R. Holzwarth, G. Ripamonti and S. Cova (1988). "Performance comparison of a single photon avalanche diode with a microchannel plate photomultiplier in time correlated single photon counting." Review of Scientific Instruments **59**(7): 1148-1152.
- Madsen, K., H. B. Nielsen and O. Tingleff (2004). Methods for non-linear least squares problems, Technical Report, Informatics and Mathematical Modelling Technical University of Denmark.
- Metropolis, N. and S. Ulam (1949). "The Monte Carlo method." J Am Stat Assoc **44**(247): 335-341.
- Press, W. H., S. A. Teukolsky, W. T. Vetterling and B. P. Flannery (1992). Numerical Recipes in FORTRAN 77, 2nd ed., The Art of Scientific Computing., Cambridge, U.K., Cambridge University Press.
- Sassaroli, A., F. Martelli and S. Fantini (2010). "Perturbation theory for the diffusion equation by use of the moments of the generalized temporal point-spread function. III. Frequency-domain and time-domain results." J Opt Soc Am A Opt Image Sci Vis **27**(7): 1723-1742.
- Szmacinski, H., J. R. Lakowicz and M. L. Johnson (1994). Fluorescence lifetime imaging microscopy: Homodyne technique using high-speed gated image intensifier. Methods in Enzymology. L. B. Michael L. Johnson, Academic Press. **Volume 240**: 723-748.
- Tsuchiya, Y. (2001). "Photon path distribution and optical responses of turbid media: theoretical analysis based on the microscopic Beer-Lambert law." Phys Med Biol **46**(8): 2067-2084.

Chapter 5

Experimental Studies based on Homogenous Modeling

In this chapter, I present three studies, wherein we performed absolute measurements of the optical coefficients in biological tissues *in vivo* under the assumption of homogeneity of the probed tissue volume.

In Section 5.1, I describe a study in a rabbit model of testicular ischemia, which provided for an excellent opportunity to demonstrate the proof-of-concept of our frequency domain NIRS approach to perform absolute tissue oximetry *in vivo* in small tissue volumes. In collaboration with Dr. Harriet Paltiel at the Children's Hospital Boston (Boston, MA), we explored the potential applicability of our methods in pediatric urology, specifically in the detection, assessment, and evaluation of testicular torsion, a prominent pediatric disorder.

In Section 5.2, we investigate the potential of our NIRS approach in the structurally and functionally much more complex brain tissue, specifically in rat. Studying a rat model made an appropriate first step towards performing such measurements in the brain (through intact skull) due to the thin superficial skin/scalp tissue layer overlaying the cerebral tissue layer. In collaboration with Dr. Aron Troen at

the Human Nutrition Research Center on Aging (HNRCA USDA, Boston, MA), we explored the feasibility of performing noninvasive cerebral oximetry measurements in rat. Specifically, we employed a strategy similar to that of the testicular ischemia study (Section 5.1) to investigate cerebrovascular impairment in a rat model of diet-induced vascular cognitive impairment (VCI).

Encouraging results in the rat study (Section 5.2) led the way for investigating our approach in the human brain. In Section 5.3, I describe an exploratory study in the elderly and young human subjects, wherein we investigated the feasibility of absolute NIRS measurements, featuring homogenous semi-infinite analysis, in the adult human forehead.

5.1. Rabbit model of testicular ischemia

5.1.1. Background to the Study

Testicular torsion is the most serious cause of acute scrotal symptoms, with an incidence of approximately 1 in 4000 (Williamson 1976). Torsion occurs at all ages, although it is most common in the pediatric population. Because of the risk of infarction, testicular torsion must be immediately excluded in any patient who presents with acute scrotal symptoms. Historically, about 50% of all torsive testes explored emergently are successfully salvaged, while the other 50% require orchiectomy or develop postoperative atrophy (Koh *et al.* 1995). Color Doppler ultrasound (US) is routinely employed worldwide to elucidate the various causes of acute scrotal pain with a high degree of success due to its ability to directly visualize the testicular blood supply and to depict alterations

in perfusion without the need for ionizing radiation. However, there are persistent limitations of conventional color Doppler US in the diagnosis of testicular torsion, especially in the pediatric population (Nussbaum Blask *et al.* 2002; Kalfa *et al.* 2004; Karmazyn *et al.* 2005). Color Doppler diagnosis of torsion is based on a subjective impression of unilaterally diminished testicular perfusion and tissue ischemia. However, in the prepubertal population in particular, normal testicular flow is depicted with difficulty. A noninvasive diagnostic method capable of providing quantitative measurement of tissue oxygenation, rather than a qualitative assessment of relative testicular perfusion as provided by color Doppler US, would be ideal for evaluating patients with acute scrotal symptoms and assessing testicular viability after detorsion. Given the potential risks of anesthesia and surgery, an added benefit would be the avoidance of emergency exploration in patients with nonviable testes.

NIRS has been previously proposed for imaging human testes with an envisioned application of testicular tumor detection (Hampel *et al.* 2002), and it has been used to assess testicular hemodynamics and oxygenation in a boar model based on the occlusion of the spermatic vessel or the vas deferens with its vessels (Colier *et al.* 1995) and in a sheep model of testicular torsion (Capraro *et al.* 2007). The boar study showed the capability of NIRS in detecting the effects of vascular occlusions in testes through relative measurements of active testicular blood volume (ATBV). Specifically, in their boar study, Colier *et al.* found no measurable ATBV after occlusion of the spermatic vessels, suggesting subsequent atrophy (Colier *et al.* 1995). In this boar study, NIRS measurements of active testicular blood volume required a transient lowering of arterial saturation by reducing the fraction of inspired oxygen for a few minutes. The sheep study

(Colier *et al.* 1995) investigated the absolute tissue saturation (StO₂) of testes at baseline, and following 720-degree torsion (on one side) or sham surgery (on the other side), similar to the protocol reported in our study. NIRS measurements were performed every 15 minutes with a single source-detector distance, continuous-wave spectrometer that allowed for absolute tissue saturation measurements. The results of the sheep study found a median baseline tissue saturation of 59% (interquartile range 57–69%) on the experimental side and 67% (interquartile range 59–68%) on the control-side (Capraro *et al.* 2007). About 2.5 hours after torsion surgery, the torsioned testes stabilized to a lower median tissue saturation value of 14% (interquartile range 11–29%), whereas the sham-surgery testes showed an increased median tissue saturation of 77% (interquartile range 77–94%) (Capraro *et al.* 2007).

We have conducted measurements on rabbit's testes, whose size compare well to those found in the pediatric population. In contrast to the boar and sheep studies reported above, we have used a multi-distance, frequency-domain NIRS approach (as described in Chapter 2) for quantifying the absolute concentration and oxygen saturation of hemoglobin in testicular tissue. We separately measured the absorption and reduced scattering coefficients of tissue as described in Chapter 2, and translated the absorption coefficients at two wavelengths (690 and 830 nm in this study) into absolute concentration and oxygen saturation of hemoglobin.

5.1.2. Methods

Four adult male New Zealand white rabbits (Millbrook Breeding Labs, Amherst, Mass) with a mean weight of 4.0 kg were examined. The study was performed according to a

protocol approved by the Animal Care and Use Committee of Children's Hospital Boston, Boston, MA, and conformed to guidelines issued by the National Institutes of Health for care of laboratory animals. General anesthesia was induced with Glycopyrrolate 0.04 mg/kg IM, followed by Ketamine 10 mg/kg IV, and Acepromazine 0.5 mg/kg IV. Endotracheal intubation was performed, and the animals placed on a ventilator. Anesthesia was maintained with 0.25-3% Isoflurane. The A catheter was placed in one ear vein of each experimental animal for administration of maintenance fluids. A heparin flush was placed on the venous line. For pain control prior to scrotal incision and testicular torsion, a spermatic cord block was administered containing Bupivacaine/Lidocaine (≤ 3 mg/kg total dose) and a dose of Ketoprofen (1mg/kg) IM. At the conclusion of the experiment, each rabbit was sacrificed with an intravenous overdose of pentobarbital (1 mL/4.5 kg).

Bilateral medial, ventral incisions were made under sterile conditions and the scrotal layers dissected to the tunica vaginalis. The testes were exposed, and following unilateral torsion and contralateral orchidopexy the testes were secured in place and the overlying scrotum closed. Baseline NIRS measurements of testicular oxygen saturation levels were obtained followed by unilateral testicular torsion (720° in rabbits 1 and 3; 540° in rabbit 2; 0° [sham surgery] in rabbit 4) on the experimental testis and contralateral sham surgery on the control testis. Sham surgery on the experimental side was referred to as 0° torsion due to the clinical protocol.

The NIRS experiments were performed using one fiber-coupled photomultiplier tube (PMT) detector and two fiber-coupled laser diodes, one emitting at 690 nm and the other at 830 nm, of an OxiplexTS (ISS, Inc., Champaign, IL) optical tissue spectrometer

(as described thoroughly in Chapter 4). Light was delivered to and from the tissue by a pair of single illumination fibers, 400 μm in diameter, and by one 3.0 mm-diameter detector optical fiber bundle. The two source fibers carrying light at 690 and 830 nm were bundled together and positioned right next to each other at the emission end. A programmable mechanical linear stage (Model XN10-0020-M01-71, Velmex, Inc., Bloomfield, NY) was used for linear scanning of the two illumination fibers toward and away from the fixed collection fiber bundle over each testis.

Multi-distance, frequency-domain measurements were performed on each testis, with a fixed detector and a linearly scanned dual-wavelength source. Probe placement and scanning method are illustrated in figure 5.1.

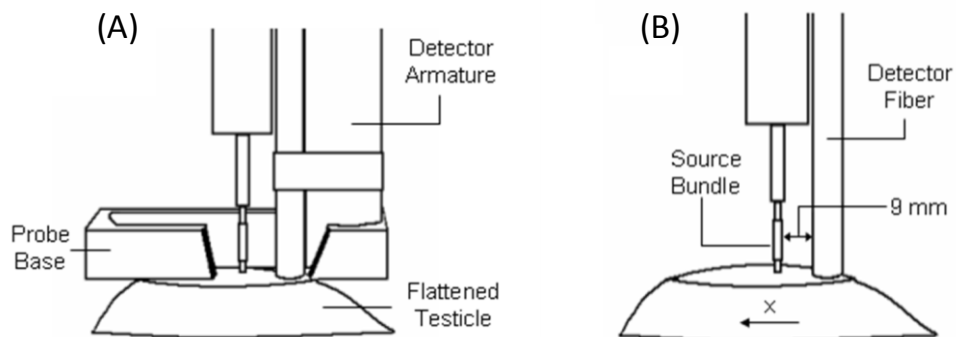


Figure 5.1. Configuration of the specially-designed optical probe, showing (A) a schematic diagram of the probe including the flattening base; (B) a simplified image of the probe showing the scanning path and distance.

The detector fiber was placed in contact with the tissue at the inferior aspect of the scrotum and the source pair of illumination fibers was placed at a distance of ~ 1 mm from the tissue and at an initial distance of approximately 9 mm from the detector fiber.

We performed a linear scan of the source pair along the x coordinate (shown in the figure) over the gently flattened scrotal surface covering a source-detector distance range of ~ 9 mm to ~ 18 mm. During the linear scan we acquired frequency-domain measurements of amplitude (AC) and phase (PH). The linear scan was performed back and forth in “sweeps” (each unidirectional scan) multiple times in a continuous manner. Ideal measurement method would be to register the beginning and end of each scan within the oximeter, however due to hardware limitations such as the maximum data acquisition rate of the oximeter and the minimum scan speed of the linear stage, this was not a possible option in this work. Instead, source fiber positions and NIRS measurements were logged separately, and the linear scanner was setup to generate a trigger signal that was transmitted through an auxiliary connection to the computer and registered by the NIRS instrument for synchronization purposes. An average scanning speed of ~ 2.6 mm/s was used, while optical measurements were taken at a data acquisition rate of 25 Hz. Two sets of optical properties (one set at 690 nm and one set at 830 nm) were obtained through each sweep. Each sweep was followed by a ~ 5 s pause (that brought scanning motors to a complete stop) to help separate the continuous scans and set the experimental parameters to default before each scan. As a result, we collected one amplitude/phase data point every ~ 0.1 mm along the scanning coordinate x , and one absorption/scattering data point (from each sweep) every $\sim 8-9$ s. Of course, one can increase the speed of data collection (one single sweep yields a reading of optical coefficients in a few seconds) but for the purposes of this study, aimed at measurements of stable baseline or post-surgery values of hemoglobin concentration and saturation, a time of 8 to 9 s between successive measurements of optical coefficients was appropriate.

We used the frequency-domain solution to the diffusion equation in the semi-infinite geometry with extrapolated boundary conditions as a model for the optical signal detected in our study (as described in detail in Chapter 2). This solution was implemented in an inversion procedure using the Levenberg-Marquardt method (as described in detail in Chapter 4) to iteratively compute the absolute optical properties (μ_a and μ'_s) of the testicular tissue from the AC and PH of the detected optical signal. From the absorption coefficients obtained with this fitting procedure, concentrations of oxy-hemoglobin [HbO_2] and deoxy-hemoglobin [Hb] in testicular tissue was calculated using Eqs. (5.1) and (5.2), respectively (Fantini *et al.* 1994):

$$[\text{HbO}_2] = \frac{\mu_a^{\lambda_1} \epsilon_{\text{Hb}}^{\lambda_2} - \mu_a^{\lambda_2} \epsilon_{\text{Hb}}^{\lambda_1}}{\epsilon_{\text{HbO}_2}^{\lambda_1} \epsilon_{\text{Hb}}^{\lambda_2} - \epsilon_{\text{HbO}_2}^{\lambda_2} \epsilon_{\text{Hb}}^{\lambda_1}}, \quad (5.1)$$

$$[\text{Hb}] = \frac{\mu_a^{\lambda_2} \epsilon_{\text{HbO}_2}^{\lambda_1} - \mu_a^{\lambda_1} \epsilon_{\text{HbO}_2}^{\lambda_2}}{\epsilon_{\text{HbO}_2}^{\lambda_1} \epsilon_{\text{Hb}}^{\lambda_2} - \epsilon_{\text{HbO}_2}^{\lambda_2} \epsilon_{\text{Hb}}^{\lambda_1}}, \quad (5.2)$$

where ϵ_{Hb} and ϵ_{HbO_2} are the molar extinction coefficients of deoxy-hemoglobin and oxy-hemoglobin (here we have used the following values (Wray *et al.* 1988): $\epsilon_{\text{Hb}}(690 \text{ nm}) = 4.854 \text{ mM}^{-1}\text{cm}$, $\epsilon_{\text{HbO}_2}(690 \text{ nm}) = 0.956 \text{ mM}^{-1}\text{cm}$, $\epsilon_{\text{Hb}}(830 \text{ nm}) = 1.790 \text{ mM}^{-1}\text{cm}$, $\epsilon_{\text{HbO}_2}(830 \text{ nm}) = 2.333 \text{ mM}^{-1}\text{cm}$). Finally, the oxygen saturation of hemoglobin in the tissue (StO_2) is given by (Fantini *et al.* 1994):

$$\text{StO}_2 = \frac{[\text{HbO}_2]}{[\text{HbO}_2] + [\text{Hb}]}. \quad (5.3)$$

5.1.3. Results of the Study

In each rabbit we performed sequential measurements on the two sides preoperative and postoperative. Each measurement consisted of about one hundred and twelve sweeps of the illumination fibers over a total time of about 25 min. In Table 5.1, we report the average values measured over the multiple sweeps for the absorption and reduced scattering coefficients (at both wavelengths), the concentrations of oxy-hemoglobin, deoxy-hemoglobin, and total hemoglobin, and the tissue hemoglobin saturation for right and left sides, pre and postoperative, for all four rabbits.

Table 5.1. Mean absolute values of the optical properties (absorption coefficient (μ_a) and reduced scattering coefficient (μ'_s)) at 690 and 830 nm, hemoglobin concentrations (oxy-hemoglobin [HbO₂], deoxy-hemoglobin [Hb], total hemoglobin [tHb]) and hemoglobin saturation (StO₂) measured on the right and left testes of the four rabbits included in this study. The error in the last significant digit is reported in parenthesis and represents the standard deviation of the measurements over multiple scans.

Testis Side	Surgical Stage	μ_a 690 nm (cm ⁻¹)	μ_a 830 nm (cm ⁻¹)	μ'_s 690 nm (cm ⁻¹)	μ'_s 830 nm (cm ⁻¹)	[HbO ₂] (μM)	[Hb] (μM)	[tHb] (μM)	StO ₂ (%)
Left	Baseline	0.16(1)	0.21(2)	6.0(3)	5.6(4)	73(10)	19(2)	92(12)	79(2)
	Control	0.19(1)	0.19(1)	6.8(4)	5.6(3)	57(8)	27(4)	84(11)	67(5)
Right	Baseline	0.18(2)	0.22(3)	5.3(3)	4.9(4)	79(14)	21(3)	100(17)	79(3)
	Torsion-720°	0.26(2)	0.15(1)	6.1(3)	5.2(2)	30(6)	47(4)	77(10)	39(6)
Left	Baseline	0.12(1)	0.18(2)	5.9(1)	5.4(3)	68(9)	12(2)	80(11)	84(3)
	Torsion-540°	0.29(4)	0.16(3)	5.6(3)	4.2(6)	30(10)	53(8)	83(18)	35(8)
Right	Baseline	0.17(1)	0.20(2)	5.5(1)	4.9(3)	68(10)	22(2)	90(13)	76(4)
	Control	0.18(3)	0.23(3)	5.8(4)	5.1(6)	84(15)	20(5)	103(20)	81(4)
Left	Baseline	0.12(1)	0.14(1)	3.9(3)	3.5(4)	49(7)	14(2)	64(9)	78(4)
	Torsion-720°	0.33(2)	0.19(1)	8.1(7)	7.0(3)	34(8)	62(6)	96(14)	36(7)
Right	Baseline	0.12(0)	0.12(1)	4.7(1)	3.8(2)	38(3)	18(1)	56(5)	68(3)
	Control	0.14(2)	0.16(4)	4.1(4)	3.7(4)	57(12)	17(8)	73(21)	77(4)
Left	Baseline	0.13(1)	0.17(1)	4.6(1)	4.0(2)	59(5)	16(1)	75(7)	79(2)
	Control	0.29(1)	0.35(4)	3.0(7)	3.0(3)	125(7)	35(2)	160(9)	78(2)
Right	Baseline	0.12(1)	0.16(1)	4.7(3)	3.8(3)	57(7)	13(2)	70(9)	81(4)
	Torsion-0°	0.22(2)	0.29(2)	3.1(2)	3.0(1)	106(8)	25(4)	131(12)	81(3)

The error in each of these measured parameters was estimated by the standard deviation over the multiple sweeps and is reported in Table 5.1, where the error in the last significant digit is indicated in parenthesis. Such standard deviation over the multiple sweeps, as opposed to the standard error (*i.e.* the standard deviation divided by the square root of the number of sweeps), gives an estimate of the error on a single measurement, which is the case of a practical clinical measurement.

At baseline and after sham surgery, the absorption coefficients at 690 nm are smaller than those at 830 nm, which is consistent with high values of hemoglobin saturation (>65%). By contrast, after torsion surgery the absorption coefficients at 690 nm are greater than those at 830 nm, which is indicative of low values of hemoglobin saturation (<40%). Such dramatic wavelength-dependent changes observed in the measured absorption coefficients after torsion surgery are not reflected in similar or correlated changes in the reduced scattering coefficients, which always show smaller values at the longer wavelength, as expected for the case of optically turbid media such as tissues. In fact, the normalized differences of the optical coefficients at the two wavelengths [*i.e.* $[\mu^{690\text{nm}} - \mu^{830\text{nm}}]/[\mu^{690\text{nm}} + \mu^{830\text{nm}}]$ where μ is either the absorption or reduced scattering coefficient] show a change between post- and pre-torsion-surgery of $0.40 \pm 0.08\%$ for absorption (significantly different from zero: $p < 0.02$) and $0.05 \pm 0.04\%$ for reduced scattering (not significantly different from zero: $p > 0.1$).

The measured values of [Hb] and [HbO₂] tissue concentrations before and after surgery are reported graphically in figure 5.2, while the absolute values of tissue oxygen saturation before and after surgery are shown in figure 5.3.

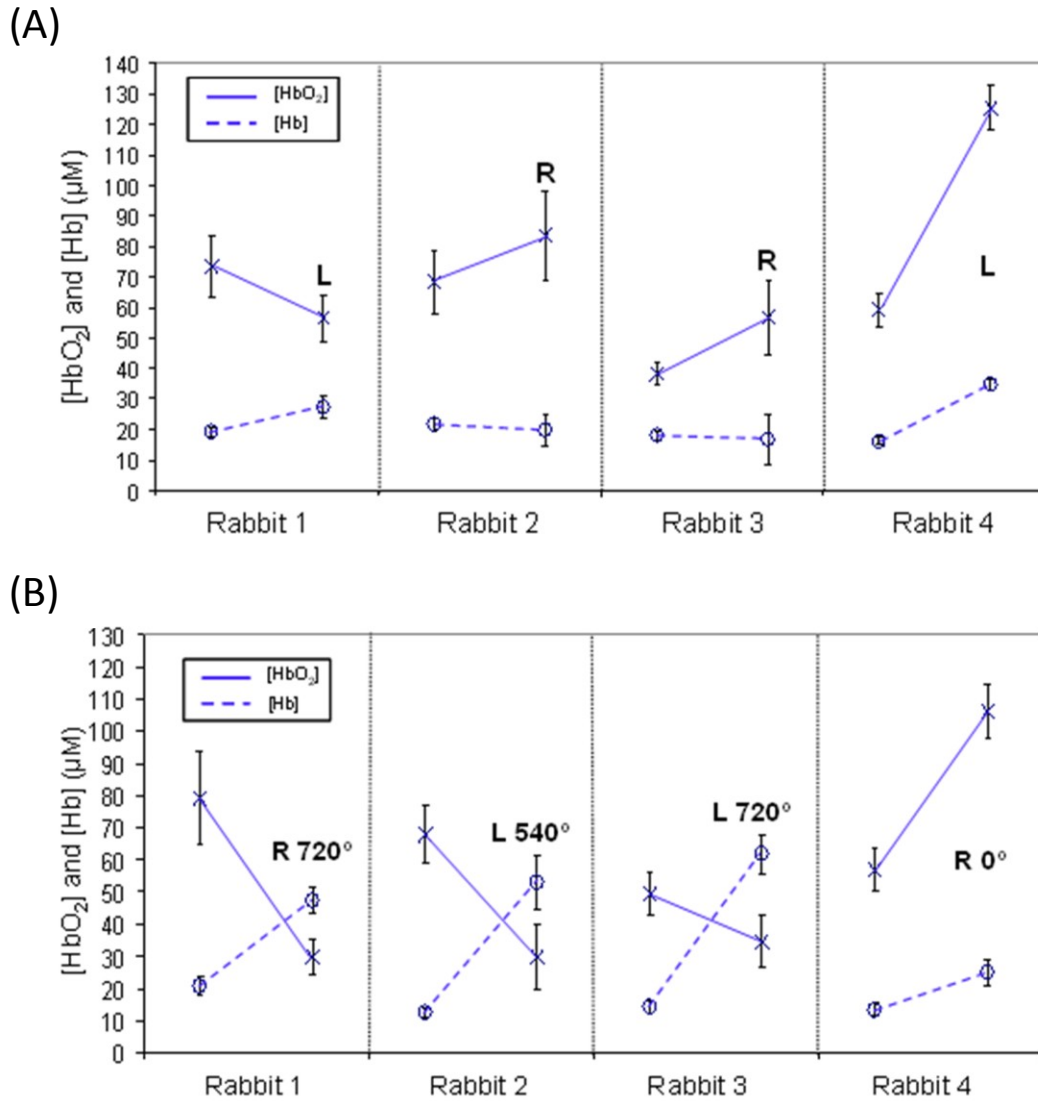
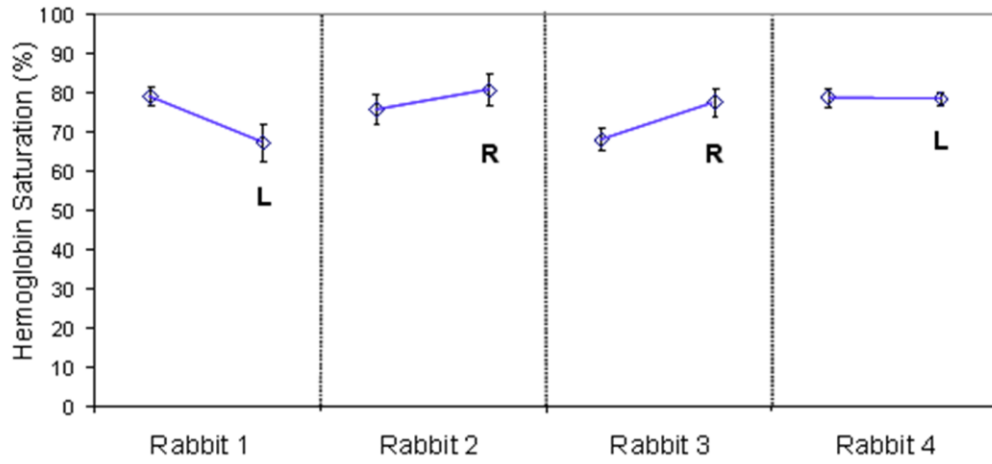


Figure 5.2. Absolute values of concentrations of HbO_2 and Hb measured in testicular tissue for all four rabbits. Each line starts at the baseline value and ends at the postoperative value of $[\text{HbO}_2]$ (continuous lines) and $[\text{Hb}]$ (dashed lines) on the control testes (panel (A)) or the experimental testes (panel (B)).

(A)



(B)

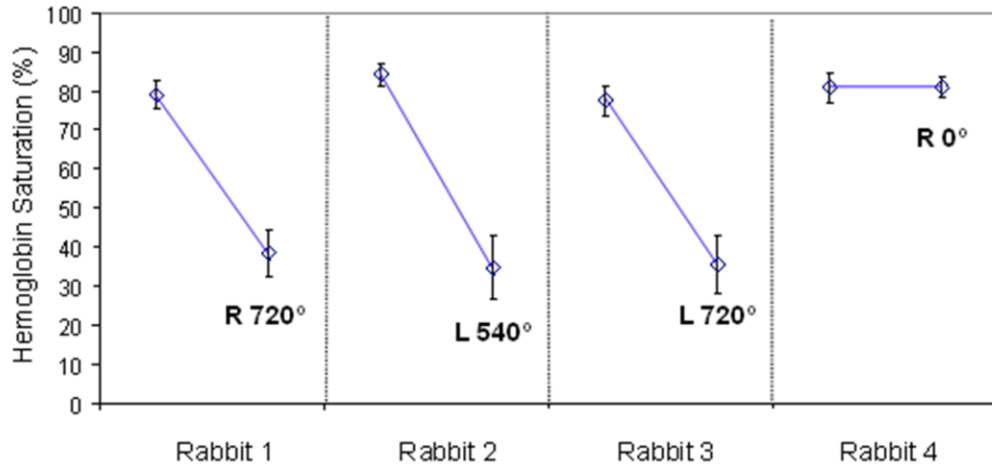


Figure 5.3. Absolute hemoglobin saturation values measured in the testicular tissue for all four rabbits. Each line starts at the baseline value and ends at the postoperative value of tissue hemoglobin saturation on the control testes [panel (A)] or the experimental testes [panel (B)].

The main results reported in figures 5.2 and 5.3 are:

(1) The absolute baseline (preoperative) values of [Hb], [HbO₂], and StO₂ are consistent across animals with average \pm standard deviation values of $17 \pm 3 \mu\text{M}$ for baseline [Hb], $62 \pm 13 \mu\text{M}$ for baseline [HbO₂], and $78\% \pm 5\%$ for baseline StO₂;

(2) The absolute values of [Hb], [HbO₂], and StO₂ after sham surgery are consistent across animals with average \pm standard deviation values of $25 \pm 7 \mu\text{M}$ for baseline [Hb], $86 \pm 30 \mu\text{M}$ for baseline [HbO₂], and $77\% \pm 6\%$ for baseline StO₂;

(3) the absolute values of [Hb], [HbO₂], and StO₂ after torsion surgery are consistent across animals with average \pm standard deviation values of $54 \pm 7 \mu\text{M}$ for baseline [Hb], $31 \pm 3 \mu\text{M}$ for baseline [HbO₂], and $36\% \pm 2\%$ for baseline StO₂;

(4) as a result of our absolute measurements at baseline, after sham, and after torsion surgery, we have found that the changes in [Hb], [HbO₂], and StO₂ in response to sham surgery ($\Delta[\text{Hb}]^{(\text{sham})} = 7 \pm 9 \mu\text{M}$, $\Delta[\text{HbO}_2]^{(\text{sham})} = 27 \pm 32 \mu\text{M}$, $\Delta\text{StO}_2^{(\text{sham})} = 0\% \pm 8\%$) are significantly different from the changes in response to torsion surgery ($\Delta[\text{Hb}]^{(\text{torsion})} = 38 \pm 11 \mu\text{M}$, $\Delta[\text{HbO}_2]^{(\text{torsion})} = -34 \pm 17 \mu\text{M}$, $\Delta\text{StO}_2^{(\text{torsion})} = -44\% \pm 5\%$).

In summary, the strong testicular tissue desaturation measured in response to torsion surgery, and the consistent absolute values of hemoglobin concentration and saturation across animals were the major results of this study.

5.1.4. Discussion of the Results

The absolute measurement capability of our frequency-domain approach to near-infrared oximetry employed in the rabbit study was a feature of paramount importance. In fact, a

reliable assessment of tissue viability in a clinical setting may not always be based on relative measurements of changes induced by a diagnostic procedure. In the specific case of testicular viability assessment, which was the focus of this study, the question was how do values of hemoglobin saturation in pathologic testes compare with the range of saturation values measured on healthy testes. Even though this study involved a relatively small number of animals (four), it nevertheless provided strong indications on this point. In fact, the absolute values of tissue hemoglobin saturation measured on torsioned testes ($36\% \pm 2\%$, $n=3$) were significantly different from the saturation values measured at baseline, after sham surgery, or after 0° torsion surgery ($77\% \pm 5\%$, $n = 13$) ($p < 0.0001$). As a result, one could hypothesize that absolute oxygenation measurements could successfully assess testicular viability for the diagnosis of testicular torsion and monitoring of therapy without relying on a comparison with reference or baseline data. Here I stress again that the errors on the reported oxygen saturation measurements are the standard deviations of the measurements over multiple sweeps, so that they provide indications on errors on a single measurement, which is relevant for prospective clinical applications of the method.

The relatively small variability of 5-6% (standard deviation) in the tissue hemoglobin saturation (StO_2) measured across animals at baseline (pre-surgery) and after sham surgery demonstrates the relative insensitivity of StO_2 to a number of factors that may potentially confound NIRS measurements. In this study, such factors included changes in temperature and blood pressure of the animal and vascular changes induced by surgery. Furthermore, physical effects such as the changes in testicular structure and presence of sutures after surgery could have also potentially introduce artifacts or

unwanted contributions to optical measurements. However, despite the many potentially confounding factors introduced by surgery, the absolute measurements reported in this study were highly consistent, especially those for StO₂, which allowed NIRS to robustly differentiate between sham surgery and torsion surgery.

The approach employed in this study for the absolute measurement of the concentration and oxygen saturation of hemoglobin in testicular tissue was based on multi-distance, frequency-domain NIRS, in conjunction with the solution to the diffusion equation for semi-infinite boundary conditions, as given in Chapter 2, Section 2.2.2. Here, the assumptions associated with the use of this solution are tissue homogeneity, the applicability of diffusion theory (which we validated through phantom measurements in Appendix B), and semi-infinite boundary conditions (which are well-approximated even for relatively small testicles in the case of high absorption coefficients, such as those observed by us of 1-2 mm⁻¹).

5.2. Rat model of Vascular Cognitive Impairment (VCI)

5.2.1. Background to the Study

Folate deficiency and its associated elevation of plasma homocysteine have been shown to be risk factors for cognitive decline (Selhub *et al.* 2000; Kado *et al.* 2005; Troen and Rosenberg 2005), Alzheimer's disease (Clarke *et al.* 1998), cerebrovascular disease and stroke (Snowdon *et al.* 1997). Microvascular damage is thought to be an important potential mechanism for these associations. In mouse, consuming a diet deficient in folate and vitamins B12 and B6, has been shown to cause a 30% reduction in brain capillary density, in the absence of neurodegeneration and in association with impaired performance on tests of learning and memory (Troen *et al.* 2008b). In rats fed diets that are only deficient in folate, similar findings have been reported (Troen *et al.* 2008). Similarly, impaired cerebrovascular reactivity has been shown in some mouse models of hyperhomocysteinemia (Dayal *et al.* 2004; Dayal and Lentz 2008). Based on these observations our hypothesis was that folate deficiency would result in functional decrements in cerebral blood volume oxygen delivery, and vascular reactivity, which together could account for the cognitive impairment observed in rat (Troen *et al.* 2008).

5.2.2. Methods

All animal procedures were approved by the Institutional Animal Care and Use Committee of Tufts Medical Center and Jean Mayer USDA Human Nutrition Research Center on Aging. Young male Sprague Dawley rats were systematically assigned to groups of similar mean body weight (~85 g), housed individually and fed their assigned

diet for twenty weeks. Diets formulated with AIN 93 M vitamin-free ethanol-precipitated casein-based basal mix (TD 03595, Harlan Teklad, Madison, WI) and an appropriate vitamin-mix. The control diet (C) contained normal folate (2 mg FA/kg diet, vitamin mix TD 94047). The folate-deficient (FD) diet contained 0 mg FA/kg diet (vitamin mix TD 95052). The diets also contained 1% sulfathiazole (SIGMA – St. Louis MO, USA), a non-absorbed sulfa drug that inhibits folate formation by gut bacteria, to ensure that the animal's only source of available folate was from diet. Rats were provided with free access to water and group pair-fed in order to ensure comparable food intake across the population (Troen *et al.* 2008). For the NIRS measurements, they were food-deprived overnight. At the end of the 20 week study (while consuming the diets), they were euthanized by exsanguination followed by perfusion through the heart with ice-cold normal saline. Complete blood counts were performed using an aliquot of EDTA whole blood on a clinical analyzer. Folate was measured using the Quantaphase II radioassay kit (Bio-Rad Laboratories, Hercules, CA).

For the NIRS measurements, optical fibers were reproducibly positioned using a rat stereotaxic frame (Stoelting Co., Wood Dale, IL), fitted with nose mask for delivery of inhaled isoflurane anesthesia and a controlled atmosphere. One collection optical fiber bundle (3 mm in active diameter), coupled with a photomultiplier tube (PMT), was positioned at a fixed point on the posterior plane of the rat's head, ~4 mm behind the ear bars and ~1.5 mm left of the sagittal line. Two 400 μm -diameter plastic clad silica illumination fibers (that guided light at 690 and 830 nm) were positioned at a distance of ~1 mm above the scalp to allow a drag-free linear scan and prevent coupling based confounding. The illumination fibers were linearly scanned away from the collection

fiber by means of a programmable mechanical linear stage scanning system (Velmex, Inc., Bloomfield, NY), at a scanning speed of 2.5 mm/s over a range of source-detector distances of ~5–12 mm, allowing for a full linear scan (back and forth) in 5 s, thus resulting in a 5 s acquisition time per NIRS data point for tissue hemoglobin parameters. Arterial oxygen saturation (SaO_2) was monitored independently through a veterinary pulse oximeter (Nonin, Plymouth MN) from the rat's foot during experiments. All instruments were temporally synchronized and driven through our user control interface designed in LabView software (National Instruments, Austin TX). Experimental setup and NIRS probe placement/scanning scheme are illustrated in figure 5.4.

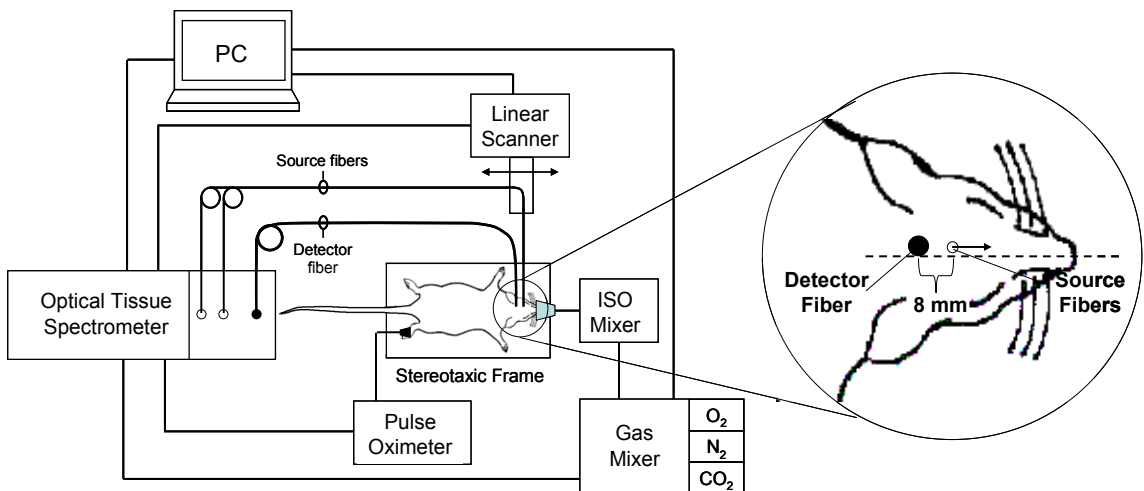


Figure 5.4: Experimental setup, optical fiber placement on the rat's head, and illustration of the linear scanning scheme for absolute near-infrared spectroscopy measurements.

Rats were food-deprived overnight, and their heads were shaved after brief induction of anesthesia with 3% inhaled isoflurane. NIRS measurements were performed in two phases consisting of intermediate (ten weeks after the initiation of diets) and final (20 weeks after the initiation of diets) measurements. For intermediate measurements, a

manually controlled modified human anesthesia device was used to administer mixtures of O₂, N₂ and CO₂ at a constant total flow rate of 10 L/min. Following 2 min baseline NIRS measurements at normal fraction of inspired oxygen (~21% FiO₂), 2 min transient hypoxia challenges (~10% FiO₂) were introduced to test for system sensitivity and method development; 4 min normoxic recovery periods followed. By week 20, a computer controlled GSM-3 gas mixer (CWE, Inc., Ardmore PA) was incorporated for more precise control and delivery of gas mixtures at a constant total flow rate of 5 liters/min. Week 20 measurements comprised the same hypoxia protocol of week 10, and in addition hypercapnia experiments that allowed evaluation of the associated hyperemic response and vasomotor reactivity. Hypercapnia experiments consisted of 1.5 min baseline NIRS measurements at normal fraction of inspired carbon dioxide (0% FiCO₂) followed by 3 min transient hypercapnia (5% FiCO₂), and 8 min normoxic recovery at 0% FiCO₂. Anesthesia was maintained with 1.5% isoflurane throughout all measurements. A warming blanket was used to maintain body temperature of rats during the procedure. All procedures were repeated three times on each rat for verification of reproducibility. Coefficient of variation (i.e. standard deviation divided by the mean) for repeat measurements of cerebral hemoglobin concentration and saturation was less than 3%.

Similar to the rabbit study, we used diffusion theory for a semi-infinite medium with extrapolated boundary conditions (Fantini *et al.* 1994) as a model for the detected optical signal. Although we collected data beginning with a source-detector separation of 5 mm, data collected at source-detector distances shorter than 8 mm were excluded from

the analysis, because studies on tissue-like phantoms showed that assumptions of our diffusion based model do not hold at shorter source-detector distances (Appendix B).

During challenge periods, we typically measured minor or no changes in reduced scattering coefficients. Figures 5.5 (a) and 5.5. (b) show two representative cases, in which the dashed lines represent the measured reduced scattering coefficient which are either constant (to within noise) [figure 5.5 (a)] or feature relatively minor changes [figure 5.5 (b)].

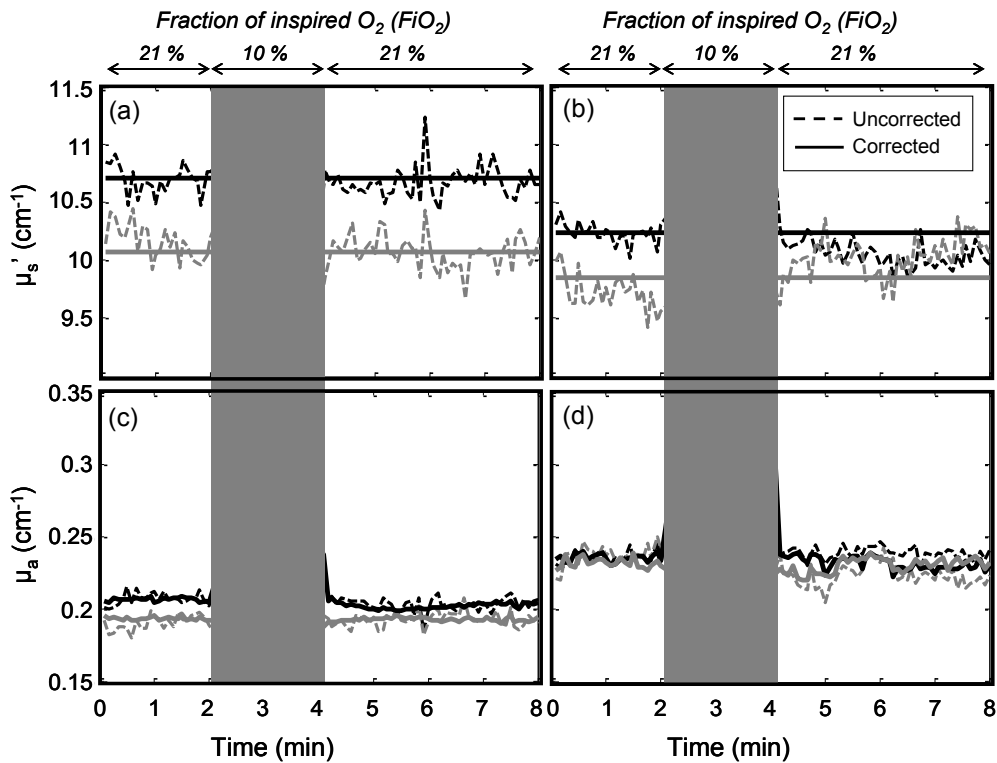


Figure 5.5: Reduced scattering coefficient (panels (a) and (b)) and absorption coefficient (panels (c) and (d)) of brain tissue measured in two different animals ((a),(c): first animal; (b),(d): second animal) during the hypoxia protocol. Black lines refer to a wavelength of 690 nm and gray lines to 830 nm. Dashed lines are the measurements of both optical coefficients from intensity and phase measurements (uncorrected). Solid lines are measurements from intensity only, after the reduced scattering coefficient has been set to a constant value (corrected) (average over the whole protocol).

Changes in opposite directions at the two wavelengths [such as the case of figure 5.5 (b)], are inconsistent with the fact that relative scattering changes in diffusive media with respect to the baseline values should not have wavelength dependence (Graaff *et al.* 1992; Kohl *et al.* 1998). Cases of observed opposite behavior of the reduced scattering coefficient at the two wavelengths, are assigned to absorption/scattering crosstalk resulting from the assumption of tissue homogeneity for the analysis of the data. To minimize crosstalk, we set the reduced scattering coefficient to a constant (the average measured value) and recalculated absorption coefficients using such constant reduced scattering value and AC intensity data. The result of this analysis method is shown by the solid traces in figure 5.5, in comparison with the dashed lines that represent the independent measurement of both absorption and reduced scattering coefficients using AC and phase. This additional step in data analysis achieves two goals; it restores the absorption changes that are mapped onto scattering values [figure 5.5(d)], and avoids noise contributions from phase measurements [figures 5.5(c) and 5.5(d)].

Similar to the rabbit study (Section 5.1), the absorption coefficients measured at two wavelengths (690 and 830 nm) were translated into absolute tissue concentrations of oxy-hemoglobin ($[HbO_2]$) and deoxy-hemoglobin ($[Hb]$) by using Eqs. (5.1) and (5.3). Using these hemoglobin parameters we derived absolute total hemoglobin concentration ($[HbT] = [HbO_2] + [Hb]$), and oxygen saturation of hemoglobin in the brain tissue.

The total hemoglobin concentrations in tissue ($[HbT]$, measured with NIRS) and in blood ($[HbT]_b$, measured from blood samples) are related by the following expression (Fantini 2002):

$$[\text{HbT}] = [\text{HbT}]_b \cdot \frac{V_b}{V_t}, \quad (5.4)$$

where V_b/V_t is the volume ratio of blood to tissue in the NIRS probed volume. By differentiating Eq. (5.4), one gets the following relationship between the relative changes in these parameters:

$$\frac{\Delta[\text{HbT}]}{[\text{HbT}]} = \frac{\Delta[\text{HbT}]_b}{[\text{HbT}]_b} + \frac{\Delta(V_b/V_t)}{(V_b/V_t)}, \quad (5.5)$$

where $\Delta(V_b/V_t)/(V_b/V_t)$ describes changes in the capillary density and in the overall cross-section of blood vessels in the investigated tissue volume. We used Eq. (5.5) to model: (i) differences between dietary groups; and (ii) changes in each dietary group from week 10 to week 20. Measured changes in total hemoglobin concentration ($\Delta[\text{HbT}]$) reflect only blood volume changes, and we used such relative changes as a measure of volume-related vasomotor reactivity (VMR), as previously reported (Vernieri *et al.* 2008):

$$\text{VMR} \equiv \frac{\Delta V_b}{V_b} = \frac{\Delta[\text{HbT}]}{[\text{HbT}]_0}, \quad (5.6)$$

where $[\text{HbT}]_0$ is the absolute tissue hemoglobin concentration during baseline (~1 min average value) and $\Delta[\text{HbT}]$ is the change induced by hypercapnia.

An important observation here was that meaningful assessment of vasomotor reactivity requires absolute measurements so that concentration changes could be normalized to baseline values [as in Eq. (5.5)]. Such absolute measurements, which were a key result of this work, are not easily achieved and in their absence one has to rely on estimating vasomotor reactivity without normalization to baseline values (Smielewski *et al.* 1995).

Statistical analysis for all parameters was performed using a two-tailed t-test with $p < 0.05$ for significance.

5.2.3. Results of the Study

All rats gained weight on the diets and no morbidity was observed. At week 10, body weight of folate deficient rats was not significantly different from controls (393 ± 9 g vs. 410 ± 7 g; $p = 0.11$). By week 20, FD rats weighed on average 10% less than control rats (423 ± 8 g vs. 467 ± 13 g; $p = 0.04$).

Folate deficient diets predictably depleted plasma folate and resulted in a corresponding increase in circulating plasma total homocysteine. At 20 weeks, blood folate in FD rats was less than 10% of control values (0.6 ± 0.3 ng/mL vs. >48 ng/mL (assay maximum); $p < 0.001$). In keeping with this finding, fasting plasma total homocysteine in FD rats, was more than 6 times higher than in controls (36.1 ± 8.2 μ mol/L vs. 4.0 ± 1.2 μ mol/L; $p < 0.001$). These values are consistent with findings from a previous study where measurements were conducted at 10 weeks (Troen *et al.* 2008).

In a previous study where blood was collected at week 10, blood hemoglobin concentrations in folate deficient rats were reported to be the same as the controls (13 ± 1 g/dL vs 13 ± 1 g/dL) (Troen *et al.* 2008). However, by week 20 of this study, folate deficient rats had lower red blood cell counts (5.5 ± 1.4 cell/mcl vs $7.9 \pm 1.2 \times 10^6$ cell/mcl; $p < 0.05$) and blood hemoglobin concentrations (11 ± 2 g/dL vs. 15 ± 2 g/dL; $p < 0.05$) compared with controls. These findings are consistent with mild macrocytic anemia that is expected in chronic folate deficiency.

Summary figures and tables. Figures 5.6 and 5.7 report time traces of measured parameters, namely tissue concentrations of oxy-hemoglobin [HbO₂], deoxy-hemoglobin [Hb], and total hemoglobin [HbT], tissue hemoglobin saturation (StO₂), and arterial saturation (SaO₂), at 10 and 20 weeks after the initiation of the diets, respectively.

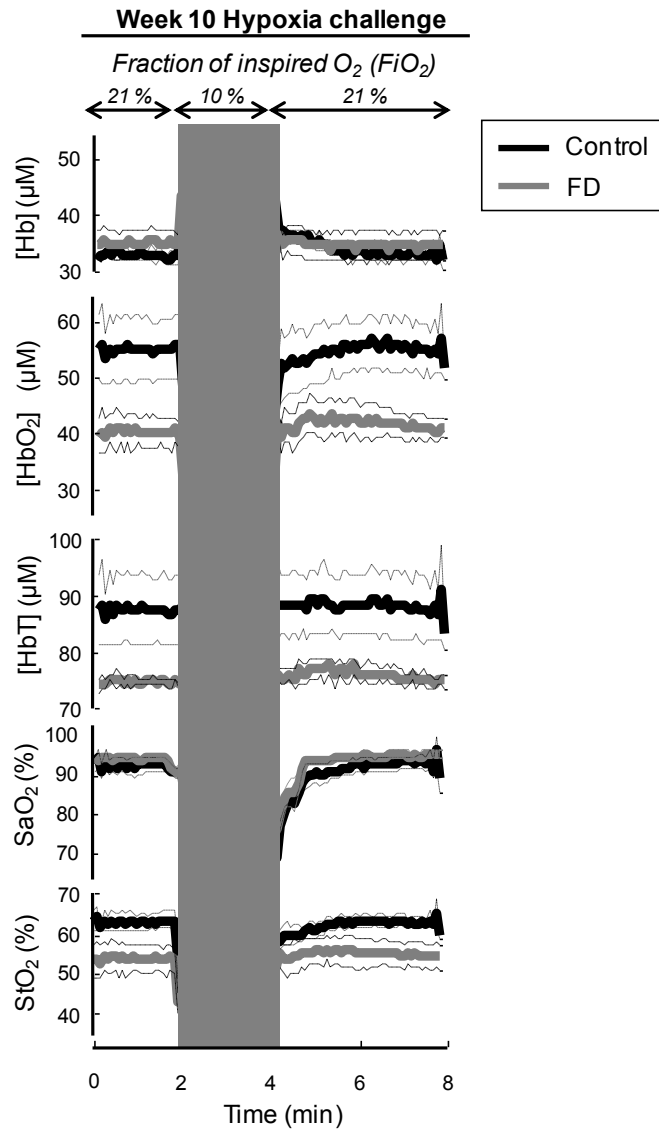


Figure 5.6. Time traces of [Hb], [HbO₂], [HbT], SaO₂ and StO₂ during the hypoxia protocol ten weeks after the start of folate deficient (FD) diet.

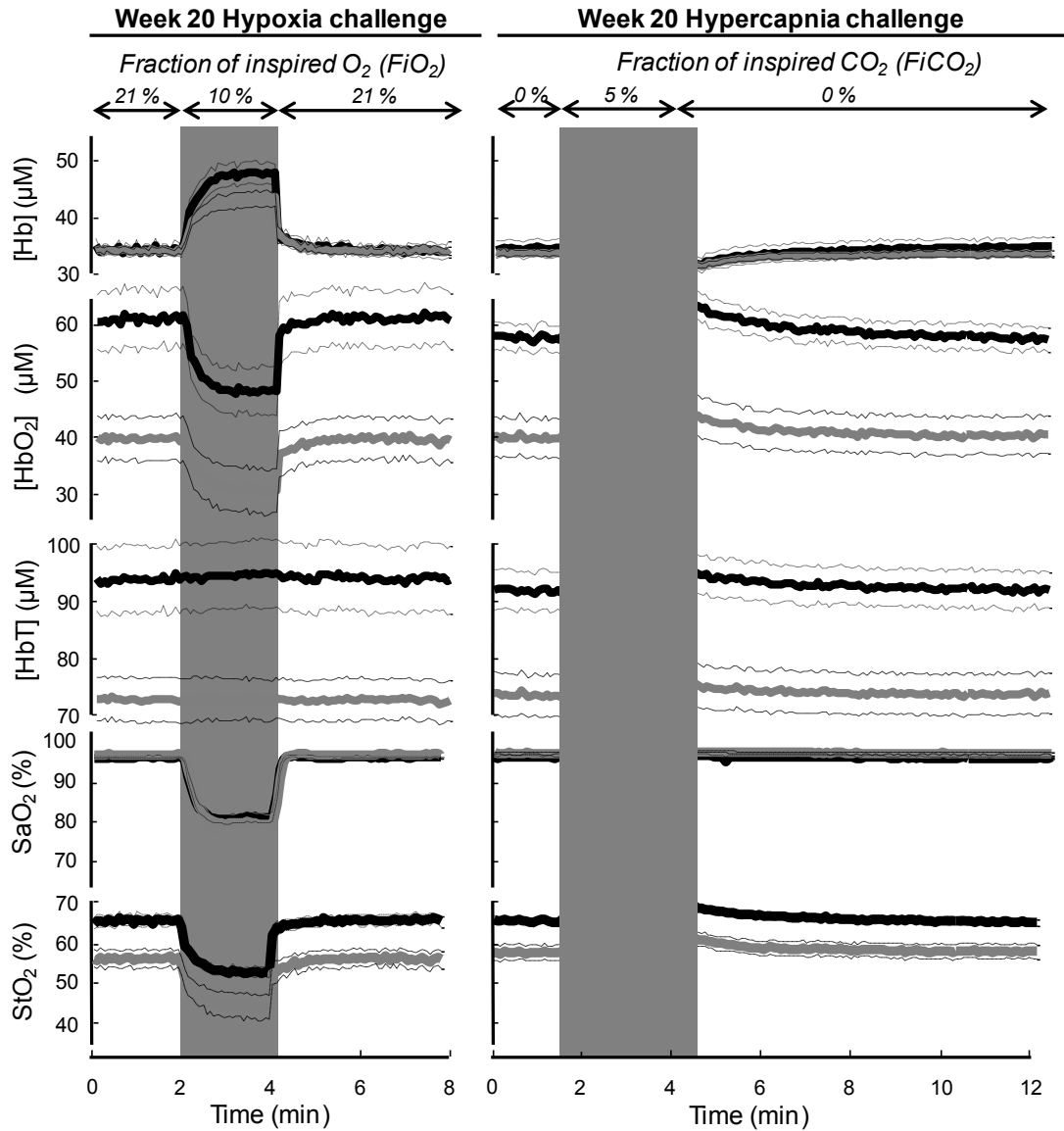


Figure 5.7. Time traces of [Hb], [HbO₂], [HbT], SaO₂ and StO₂ during the hypoxia and hypercapnia protocols twenty weeks after the start of folate deficient (FD) diet.

Solid, thick lines represent the mean values for each dietary group, whereas thin, dashed lines indicate the range corresponding to \pm one standard error from the mean. Shaded areas in figures 5.6 and 5.7 indicate the challenge periods, and column titles denote the type of challenge (transient hypoxia or transient hypercapnia). Absolute values

of the measured parameters at baseline and their changes induced by hypoxia or hypercapnia are reported in Table 5.2.

Table 5.2. Absolute cerebral NIRS parameters measured at baseline and after induction of hypoxia or hypercapnia, in folate deficient (FD) and control rats at 10 and 20 weeks. Values represent Mean (SEM).

<u>Hypoxia - Week 10</u>		[HbO ₂] (μM)	[Hb] (μM)	[HbT] (μM)	StO ₂ (%)	SaO ₂ (%)
Baseline	Control	54(6)	33(1)	87(7)	62(2)	92(2)
	FD	37(3)	35(3)	73(1)	51(4)	94(6)
Hypoxia		Δ[HbO ₂] (μM)	Δ[Hb] (μM)	Δ[HbT] (μM)	ΔStO ₂ (%)	ΔSaO ₂ (%)
	Control	-17(1)	18(1)	0.7(4)	-20(2)	-19(2)
	FD	-13(3)	13(3)	0.1(3)	-17(4)	-19(2)
<hr/>						
<u>Hypoxia - Week 20</u>		[HbO ₂] (μM)	[Hb] (μM)	[HbT] (μM)	StO ₂ (%)	SaO ₂ (%)
Baseline	Control	62(5)	33(1)	95(6)	65(2)	95(3)
	FD	40(4)	33(1)	72(4)	54(3)	95(5)
Hypoxia		Δ[HbO ₂] (μM)	Δ[Hb] (μM)	Δ[HbT] (μM)	ΔStO ₂ (%)	ΔSaO ₂ (%)
	Control	-12(1)	12(1)	0.7(1)	-12(1)	-14(1)
	FD	-8(1)	8(1)	0.1(3)	-11(3)	-16(2)
<hr/>						
<u>Hypercapnia-Week 20</u>		[HbO ₂] (μM)	[Hb] (μM)	[HbT] (μM)	StO ₂ (%)	SaO ₂ (%)
Baseline	Control	59(2)	33(2)	92(4)	65(1)	95(4)
	FD	41(4)	32(1)	72(4)	56(2)	96(4)
Hypercapnia		Δ[HbO ₂] (μM)	Δ[Hb] (μM)	Δ[HbT] (μM)	ΔStO ₂ (%)	ΔSaO ₂ (%)
	Control	6(7)	-9(4)	3(3)	4(4)	0.4(1)
	FD	4(5)	-2(3)	2(4)	4(1)	0.5(2)

Baseline absolute measurements. A first striking result is the consistency of baseline values across animals within a group (control or FD), and the reproducibility of baseline values measured at week 10 and week 20. This is important considering the intrinsic challenges of non-invasive, absolute measurements of tissue hemoglobin concentrations *in vivo*. Such consistency and reproducibility of our measurements allow us to perform meaningful comparisons among experimental groups of animals. With respect to control rats, folate deficient rats showed comparable baseline values of [Hb] and SaO₂, and

significantly lower baseline values of [HbO₂], [HbT], and StO₂ (Table 5.2). Baseline [HbO₂] values were lower by 17 ± 5 μM (or 31%) at week 10 and by 22 ± 7 μM (or 35%) at week 20. Baseline [HbT] values were lower by 14 ± 5 μM (or 16%) at week 10 and by 23 ± 7 μM (or 24%) at week 20. Baseline StO₂ values were lower by 11% ± 3% (or 18%) at week 10 and by 11% ± 3% (or 17%) at week 20 (Table 5.2). Changes in absolute baseline values of StO₂ and [HbT] for control and FD animals at weeks 10 and 20 are shown in figure 5.8.

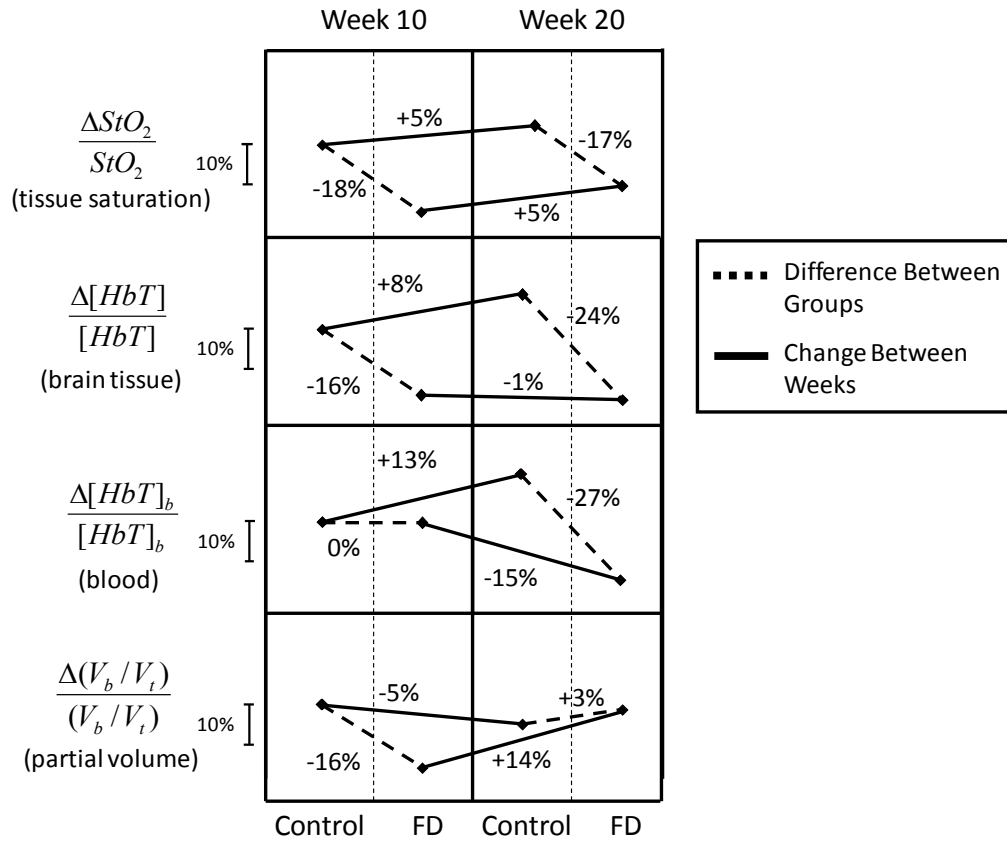


Figure 5.8: Summary of relative differences in cerebral tissue hemoglobin saturation (StO₂), tissue hemoglobin concentration ([HbT]), blood hemoglobin concentration ([HbT]_b), and partial blood volume in brain tissue (V_b/V_t) between animal groups (control and folate deficient (FD) rats) at each time point and change within each group between weeks (week 10 and week 20 after the onset of the folate deficient diet). It is important to note that such comparisons are only possible because of the absolute NIRS measurements of tissue hemoglobin concentration and saturation performed in this study.

The measured values of $[\text{HbO}_2]$ and $[\text{HbT}]$ are mostly associated with brain tissue, because our slope-based, frequency-domain method has been shown to be insensitive to the thin (~ 1 mm) superficial skin/scalp tissue layer (Franceschini *et al.* 1998). Furthermore, the specific size and shape of each rat's head is also not expected to have a significant influence on our slope-based measurements, as we have previously demonstrated that the surface curvature has only minor effects on the absolute measurement of the optical properties using this approach (Cerussi *et al.* 1996). Obtaining absolute tissue hemoglobin concentration $[\text{HbT}]$ at baseline in conjunction with measured blood hemoglobin concentrations, $[\text{HbT}]_b$, allowed us to derive an estimate of differences between groups and changes within a group in cerebral blood volume (which reflects the volume of the microvascular space) by relating blood-to-tissue partial volume according to Eq. (5.5). As shown in figure 5.8, FD rats have significantly lower cerebral blood volume (CBV) compared to control rats at week 10, but this value appears to recover to control levels by week 20.

Percent changes induced by hypoxia. Reduction in the fraction of inspired oxygen induced percent changes in SaO_2 that were comparable (about 20%) in FD rats and control rats, while it did not induce any detectable changes in $[\text{HbT}]$. In contrast with the significant differences observed between dietary groups in the absolute baseline values of $[\text{HbO}_2]$ and StO_2 (Table 5.2), their percent changes induced by hypoxia were comparable in FD rats and in control rats. At week 10, percent $[\text{HbO}_2]$ changes during hypoxia were $-35\% \pm 5\%$ in FD rats, and $-31\% \pm 4\%$ in control rats, whereas percent StO_2 changes during hypoxia were $-33\% \pm 5\%$ in FD rats, and $-32\% \pm 4\%$ in control rats. At week 20, percent $[\text{HbO}_2]$ changes during hypoxia were $-20\% \pm 3\%$ in FD rats, and $-19\% \pm 1\%$ in

control rats, whereas percent StO₂ changes during hypoxia were $-20\% \pm 3\%$ in FD rats, and $-18\% \pm 1\%$ in control rats.

Percent changes induced by hypercapnia. As shown in figure 5.7, hypercapnia induced a decrease in [Hb], an increase in [HbO₂], [HbT], and StO₂, and no changes in SaO₂. The percent increases in [HbO₂], [HbT], and StO₂ induced by hypercapnia were comparable in FD and control rats. Specifically, percent increases in [HbO₂] were $10\% \pm 1\%$ (FD) and $10\% \pm 1\%$ (control); percent increases in [HbT] were $2.4\% \pm 0.5\%$ (FD) and $3.2\% \pm 0.4\%$ (control); percent increases in StO₂ were $7\% \pm 1\%$ (FD) and $6\% \pm 1\%$ (control). The percent decreases induced by hypercapnia in [Hb] were also similar in FD rats ($7\% \pm 1\%$) and in control rats ($8\% \pm 1\%$).

The relative percent increase in [HbT] was somewhat greater in control rats than in FD rats. As described in the Methods-Data Analysis section, this finding indicates a greater volume-related vasomotor reactivity [Eq. (5.6)] in response to hypercapnia. It is possible to monitor the temporal evolution of vasomotor reactivity during hypercapnia by considering the time dependence of hemoglobin concentration changes. By doing that, we have derived an estimate of vasomotor responses to hypercapnia associated with volume changes (VMR: Figure 5.9).

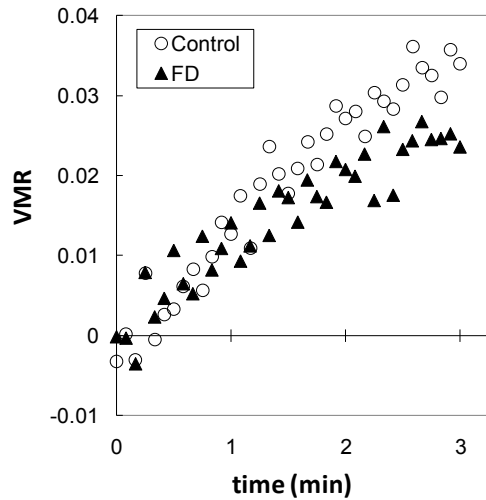


Figure 5.9. Vasomotor reactivity (VMR) in response to hypercapnia (time 0 is the start of a 3-min hypercapnia period) associated with vascular volume changes). VMR is estimated from absolute near-infrared spectroscopy measurements according to Eq. (5.6). Folate deficient (FD) rats feature a vasomotor response that is significantly dampened than the control rats by the end of the challenge period.

Slopes of the regression analysis on the first one minute of the hypercapnia challenge did not show statistical difference between FD and control rats in response to changes in blood volume ($p > 0.05$); however response to these changes at the final thirty seconds of the hypercapnia challenge were significantly lower in FD than control rats ($p < 0.001$) (figure 5.9).

5.2.4. Discussion of the Results

In this study, we demonstrated that the ability to perform non-invasive and robust absolute measurements of cerebral tissue hemoglobin concentration and saturation can be of paramount importance for the characterization of hemodynamic cerebral responses as a mechanism of neurological dysfunction. We also demonstrated the critical importance of obtaining absolute measurements of these parameters, as opposed to technically easier relative measurements. First, absolute measurements provide a baseline assessment that

allowed direct comparisons to be made between different animals, in addition to serving as a baseline reference for temporal hemodynamic responses within a given animal. Here, absolute measurements of baseline values revealed differences between the treatment (FD) and control groups that were far more pronounced and informative than the relative hemodynamic responses of each group to hypoxia and hypercapnia. The fact that absolute measures revealed significant differences between control and treatment groups, whereas relative measures did not, demonstrated the richer information content that absolute NIRS measures can provide for the evaluation of cerebrovascular health. Second, relative measurements typically require manipulations or physiological challenges that may introduce additional sources of variability and may complicate the measurement protocol (for example, the need to maintain precise levels of FiO_2 and $FiCO_2$ in the hypoxia and hypercapnia challenges considered in this study). Normalizing the dynamic response to a physiological challenge to an absolute initial value can improve the accuracy and interpretability of relative dynamic measures. Combining absolute and relative values in this way allows valuable information to be obtained, such as the derivation of vasomotor reactivity in Eq. (5.6).

Following this approach we were able to show that folate deficiency can induce a significant deficit in central nervous system oxygen delivery and blood perfusion, as indicated by lower absolute tissue concentrations of total hemoglobin [HbT] and oxy-hemoglobin [HbO₂], and lower tissue hemoglobin saturation (StO₂) despite normal arterial saturation (SaO₂)¹. This finding could explain the cognitive deficits that have

¹ Reduced baseline [HbT] in FD rats indicates a smaller cerebral blood volume. The reduction in [HbO₂] but not in [Hb] at baseline (Figure 5.7) is consistent with an increased oxygen extraction per unit blood volume (to yield the same cerebral metabolic rate of oxygen) or with a decreased blood flow velocity. Both effects would also translate into the observed lower baseline StO₂ in the FD rats.

been previously observed in this model (Troen *et al.* 2008). Indeed, we showed that resting oxygen saturation (StO_2) in folate deficient rats was about the same as StO_2 during transient hypoxia in controls (figure 5.7), suggesting that the central nervous system of folate deficient rats might be chronically exposed to sub-optimal if not overtly hypoxic conditions. Similarly, the difference in vasomotor reactivity between control and folate deficient rats suggested impaired mechanisms in the regulation of cerebral blood flow during hypercapnia in FD rats. Although chronic folate deficiency causes anemia, anemia would not explain the observed cognitive or hemodynamic deficits we observed at week 10 since blood hemoglobin was normal at week 10, and anemia only emerged later in the study. However, anemia did contribute to the observed decrease in $StO_2\%$ and [HbT] between weeks 10 and 20. In this respect, it has been documented that mammalian physiology is well adapted to compensate for reduction in the blood hemoglobin concentration (hematocrit) through optimizing the ability of the cardiovascular system to deliver oxygen to tissues. It has been reported that these adaptive hemodynamic changes include increase in heart rate and oxygen extraction, coupled with reduction in systemic vascular resistance and mean arterial pressure (Hare 2004; Vovenko and Chuikin 2008).

Our results suggested that microvascular remodeling might have also occurred between weeks 10 and 20. Relative changes in partial blood volume, obtained by combining relative changes in [HbT] and $[HbT]_b$ according to Eq. (5.5), indicated that cerebral blood volume (CBV) was lower in folate deficient rats than in controls by week 10 and slightly higher than in controls by week 20 (see figure 5.8). Under the assumptions of Eq. 5.5, the lower value of baseline [HbT] in FD rats versus controls at week 10 could be mostly assigned to a smaller CBV, because blood hemoglobin

concentrations $[\text{HbT}]_b$ did not differ between the groups at this time. In contrast, the lower baseline $[\text{HbT}]_b$ in FD rats versus controls at week 20, could be mostly assigned to the observed reduction in $[\text{HbT}]_b$ in the FD rats. The calculated reduction and recovery of CBV in the folate deficient rats, suggested that considerable microvascular remodeling might have occurred over the course of the study.

Intriguingly, the initial reduction in CBV that was observed at week 10 might be consistent with findings from other studies of capillary rarefaction in mice fed B-vitamin deficient diets for 10 weeks (Troen *et al.* 2008b) and with brain microvascular damage in rats fed folate deficient diets for 8 weeks (Kim *et al.* 2002). Assuming that the chronic reduction of brain StO_2 observed between weeks 10 and 20 did in fact result in tissue hypoxia, one might also speculate that the subsequent recovery of CBV by week 20 could be due to a hypoxia-driven angiogenesis that has been observed physiologically (LaManna *et al.* 2004) and in neurodegenerative disease (Kalaria *et al.* 1998).

In summary, we found through this study that diet-induced folate deficiency caused profound functional changes to brain hemodynamics and oxygen delivery in rats. The absolute NIRS measurements reported were significant, robust, and more informative than relative measurements. They allowed us to reveal functional cerebrovascular effects of folate deficiency, and provide a basis to test the hypothesis that such functional vascular changes were related to cognitive impairment.

5.3. Cerebral Oximetry in Elderly and Young Humans

5.3.1. Methods

We examined fifty-five subjects of whom 36 were healthy elderly adults (mean age, 85 ± 6 years; twenty-six females, ten males) and 19 were young adult volunteers (mean age, 28 ± 4 years; six females, thirteen males). The elderly subjects were participants in an ongoing epidemiological study of aging conducted by Mount Sinai School of Medicine. Sixteen of the elderly volunteers were examined a second time five months after the first session to evaluate the reproducibility of the absolute measurements. Young adults were measured separately in a third session. The research protocol was approved by Tufts University and Mount Sinai School of Medicine Institutional Review Boards, and informed consent was obtained from all subjects prior to each measurement session. Age distribution of the subjects based on measurement session is shown in figure 5.10.

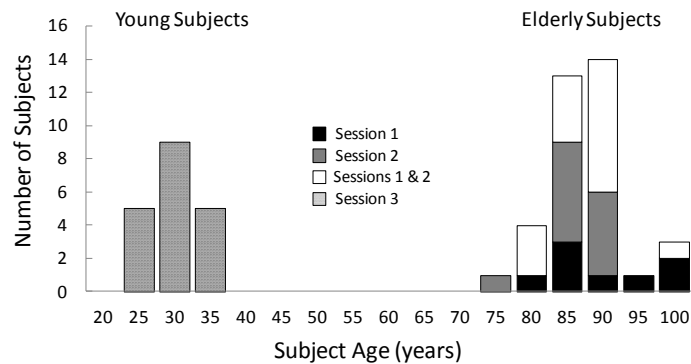


Figure 5.10. Age distribution of the human subjects investigated in this study.

We employed two different polyurethane silicon optical probes featuring one collection optical fiber bundle (3 mm in core diameter) and either four or seven illumination positions each comprising two optical fibers (0.4 mm in core diameter) that

guided light at 690 and 830 nm wavelengths, located several centimeters apart from the collection fiber bundles. Source-detector separations for the first probe used in session 1 were from 2 to 3.5 cm in 0.5 cm increments. Source-detector separations for the second probe used in sessions 2 and 3 were from 0.8 to 3.8 cm in 0.5 cm increments. In the elderly group, measurements were performed both on the left and the right side of the forehead close to the hair line. I provide an illustration of the probe layout and placement in figure 5.11.

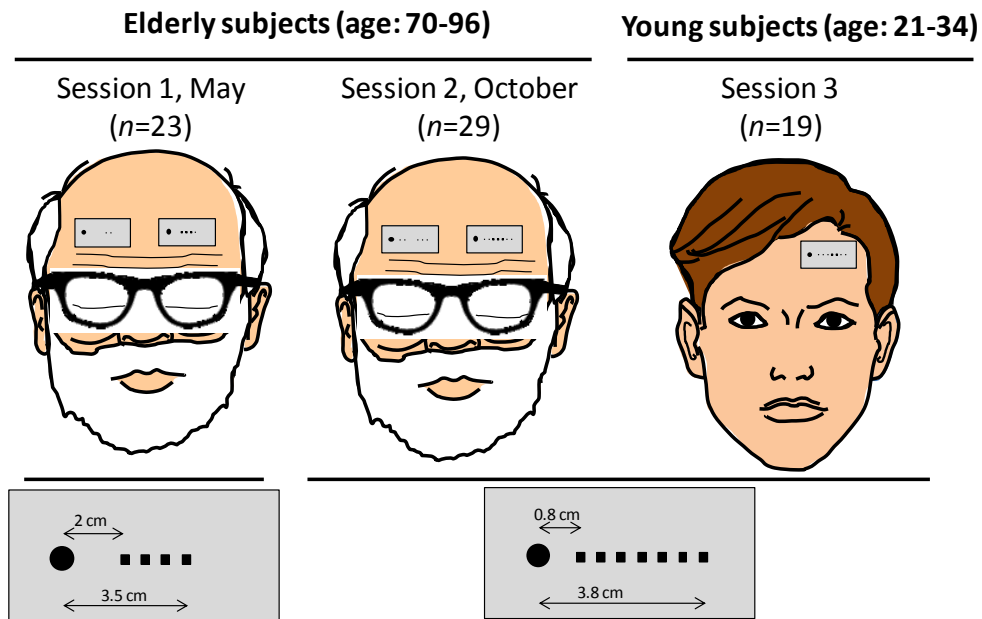


Figure 5.11. Experimental setup and protocol description.

The probes were held in place using a commercial sports band to exert light pressure for comfort, while guaranteeing good contact between the optical fibers and the subject's skin. Because of the good agreement between left and right side measurements obtained in the elderly group, measurements in young subjects were performed only on one side (left).

For the analysis, once again, we used a semi-infinite homogenous mode, similar to the rabbit (Section 5.1) and rat (Section 5.2) studies. Because of the sufficiency of the source-detector distances (I have described the criteria for sufficiency in Appendix A), in this study we used the linear approximations [Eqs. (2.11) and (2.12)] to derive the absolute absorption (μ_a) and reduced scattering (μ'_s) coefficients from the frequency-domain AC and PH values measured at multiple distances. I have provided the details of these approximations in Chapter 2 and demonstrated their validity in Appendix A. Equations (2.11) and (2.12) require that light source emissions at the matching wavelengths have identical intensity and phase values. Since this is not the case (because of physical differences among the individual laser diodes, their bias and radio-frequency supplies, and their optical coupling to the tissue), we performed a calibration procedure prior to the measurements on each subject using a phantom with empirically determined optical properties that are similar to those of cerebral tissues. We determined the phantom optical properties by a calibration-free method described in Appendix B and found them to be: $\mu_a^{690\text{nm}} \sim 0.19 \text{ cm}^{-1}$, $\mu_a^{830\text{nm}} \sim 0.16 \text{ cm}^{-1}$, $\mu'_s^{690\text{nm}} \sim 5.0 \text{ cm}^{-1}$ and $\mu'_s^{830\text{nm}} \sim 4.8 \text{ cm}^{-1}$.

We considered oxy-hemoglobin (HbO_2), deoxy-hemoglobin (Hb) and water to be the major absorbers in the probed tissue volume at the two wavelengths considered. We did not consider other absorbers such as melanin for being present only in the thin, superficial epidermis and dermis skin layers, and lipids for their lower absorption (by a factor of 2-4) with respect to water absorption at the wavelengths considered by us. Under this assumption, we have improved equations (5.1) and (5.2) reported in Section 5.1.4 to reflect the characteristics of water absorption. The revised equations for HbO_2 and Hb concentrations became:

$$[\text{HbO}_2] = \frac{\mu_a^{690\text{nm}} \cdot \epsilon_{\text{Hb}}^{830\text{nm}} - \mu_a^{830\text{nm}} \cdot \epsilon_{\text{Hb}}^{690\text{nm}}}{\epsilon_{\text{HbO}_2}^{690\text{nm}} \epsilon_{\text{Hb}}^{830\text{nm}} - \epsilon_{\text{HbO}_2}^{830\text{nm}} \epsilon_{\text{Hb}}^{690\text{nm}}} - \frac{\mu_{a(\text{H}_2\text{O})}^{690\text{nm}} \cdot \epsilon_{\text{Hb}}^{830\text{nm}} - \mu_{a(\text{H}_2\text{O})}^{830\text{nm}} \cdot \epsilon_{\text{Hb}}^{690\text{nm}}}{\epsilon_{\text{HbO}_2}^{690\text{nm}} \epsilon_{\text{Hb}}^{830\text{nm}} - \epsilon_{\text{HbO}_2}^{830\text{nm}} \epsilon_{\text{Hb}}^{690\text{nm}}} C_{\text{H}_2\text{O}-\text{vf}}, \quad (5.6)$$

$$[\text{Hb}] = \frac{\mu_a^{830\text{nm}} \cdot \epsilon_{\text{HbO}_2}^{690\text{nm}} - \mu_a^{690\text{nm}} \cdot \epsilon_{\text{HbO}_2}^{830\text{nm}}}{\epsilon_{\text{HbO}_2}^{690\text{nm}} \epsilon_{\text{Hb}}^{830\text{nm}} - \epsilon_{\text{HbO}_2}^{830\text{nm}} \epsilon_{\text{Hb}}^{690\text{nm}}} + \frac{\mu_{a(\text{H}_2\text{O})}^{690\text{nm}} \cdot \epsilon_{\text{HbO}_2}^{830\text{nm}} - \mu_{a(\text{H}_2\text{O})}^{830\text{nm}} \cdot \epsilon_{\text{HbO}_2}^{690\text{nm}}}{\epsilon_{\text{HbO}_2}^{690\text{nm}} \epsilon_{\text{Hb}}^{830\text{nm}} - \epsilon_{\text{HbO}_2}^{830\text{nm}} \epsilon_{\text{Hb}}^{690\text{nm}}} C_{\text{H}_2\text{O}-\text{vf}}, \quad (5.7)$$

where ϵ_{Hb} and ϵ_{HbO_2} are the molar extinction coefficients of HbO₂ and Hb (Wray *et al.* 1988), $\mu_{a(\text{H}_2\text{O})}$ is the absorption coefficient of water (Hale and Querry 1973), and $C_{\text{H}_2\text{O}-\text{vf}}$ is the volume fraction of water content in tissue. Equations (5.6) and (5.7) show that $[\text{HbO}_2]$ and $[\text{Hb}]$ are linear functions of $C_{\text{H}_2\text{O}-\text{vf}}$ with intercepts $[\text{HbO}_2]_0$ and $[\text{Hb}]_0$ (corresponding to the oxy- and deoxy-hemoglobin concentrations in the absence of tissue water) and slopes that can be indicated as X and Y , respectively:

$$[\text{HbO}_2] = [\text{HbO}_2]_0 - XC_{\text{H}_2\text{O}-\text{vf}} \quad (5.8)$$

$$[\text{Hb}] = [\text{Hb}]_0 + YC_{\text{H}_2\text{O}-\text{vf}} \quad (5.9)$$

By using the known water absorption and hemoglobin molar extinction coefficients, for the wavelengths considered here, we find $X = 14.9 \mu\text{M}$, and $Y = 1.8 \mu\text{M}$. In the new approach, the total hemoglobin concentration ($[\text{HbT}] = [\text{HbO}_2] + [\text{Hb}]$) and hemoglobin saturation ($\text{StO}_2 = [\text{HbO}_2]/[\text{HbT}]$) are given by:

$$[\text{HbT}] = [\text{HbT}]_0 - (X - Y)C_{\text{H}_2\text{O}-\text{vf}} \quad (7.10)$$

$$\text{StO}_2 = \frac{\text{StO}_2|_0 [\text{HbT}]_0 - XC_{\text{H}_2\text{O}-\text{vf}}}{[\text{HbT}]_0 - (X - Y)C_{\text{H}_2\text{O}-\text{vf}}} \quad (7.11)$$

where $[\text{HbT}]_0$ and $\text{StO}_2|_0$ indicate the $[\text{HbT}]$ and StO_2 in the absence of water. In this study, we assumed a value of $C_{\text{H}_2\text{O-vf}}$ of 0.7, in agreement with the choice of other optical brain studies (Ohmae *et al.* 2006; Gagnon *et al.* 2008), on the basis of reported water contents of ~ 0.8 and ~ 0.7 for gray matter and white matter, respectively (Woodard and White 1986), and ~ 0.2 for cortical bone (Techawiboonwong *et al.* 2008).

5.3.2. Results

Differences between the left and right side measurements were smaller than inter-subject variability in all parameters, and therefore we report the average of the measurements on the two sides for all elderly subjects. Young subjects were only measured on the left side (see figure 5.11). To investigate the dependence of our measurements on source-detector separation, as a result of the layered structure of the measured tissue, we have considered subsets of data collected at three consecutive source-detector separations, spanning a range of 1 cm. By applying Eqs. (5.6) and (5.7) to such subsets of multi-distance data, we generated two sets of distance-dependent optical properties from session 1 and five sets from sessions 2 and 3 (see figure. 5.11).

Figure 5.12 (above) shows the results of this approach for all measured parameters on elderly subjects, who were measured twice (*i.e.* once in session 1 and once in session 2, $n=16$), where each bar represents the session mean (bar center) and standard error (bar width) over the corresponding source-detector separations (bar length). Red and blue blocks in figure 5.12 represent the results obtained in session 1 and session 2, respectively. Session 2 measurements, which are richer in information content due to the greater number of source-detector distances, revealed a dependence

of all parameters on source-detector distance. Results of this approach are summarized in Table 5.3, which compares measurements obtained from data collected at the shortest and longest sets of source-detector distances (namely, 0.8–1.8 cm and 2.8–3.8 cm), and reports their percent differences.

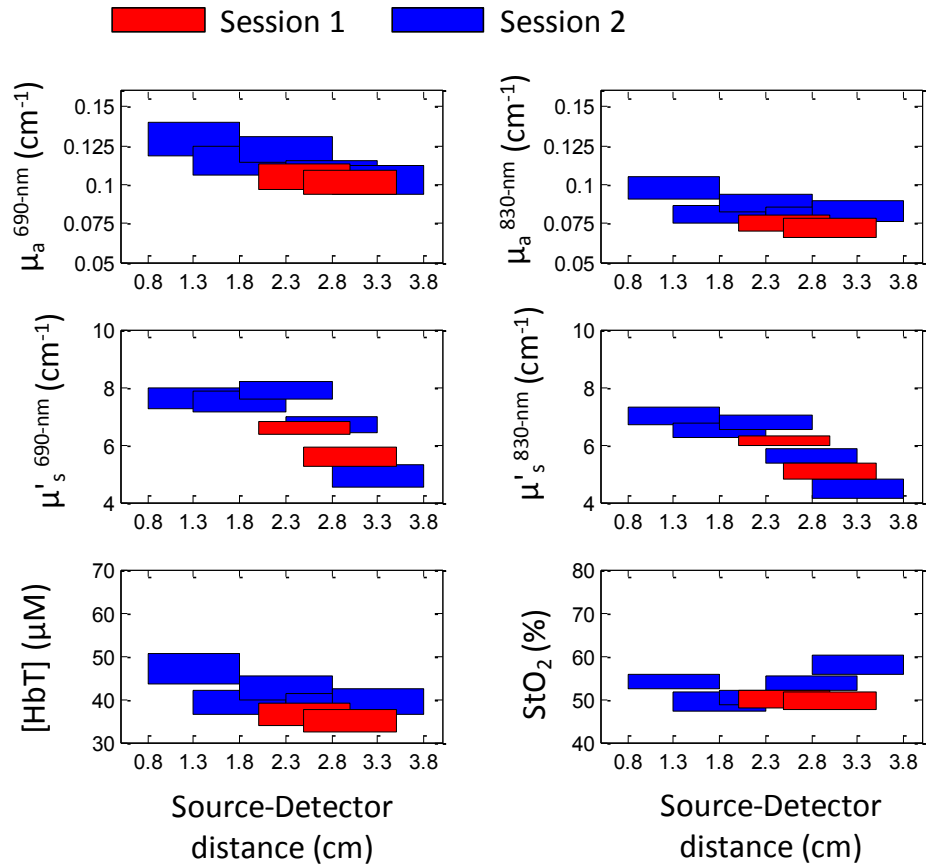


Figure 5.12. Dependence of measured parameters on source-detector separation in elderly subjects. Left and right top panels report measured μ_a at 690 and 830nm, respectively. Left and right middle panels report measured μ'_s at 690 and 830nm, respectively. Bottom left and right panels report measured [HbT] and StO₂, respectively. Grey and black blocks represent means (block center) and standard error (block thickness) of measurements in sessions 1 and 2, respectively, at corresponding distances.

Table 5.3. Dependence of optical measurements on source-detector separation. Values in parentheses represent the standard error on the last significant digit(s) of the mean.

	μ_a^{690nm} (cm^{-1})	μ_a^{830nm} (cm^{-1})	$\mu'_s{}^{690nm}$ (cm^{-1})	$\mu'_s{}^{830nm}$ (cm^{-1})	[HbO ₂] (μM)	[Hb] (μM)	[HbT] (μM)	StO ₂ (%)
Session 2 – Elderly Repeated (n=16)								
0.8 - 1.8 cm	0.13(1)	0.10(1)	7.6 (4)	7.0(3)	26(2)	22(2)	48(4)	54(2)
2.8 - 3.8 cm	0.10(1)	0.08(1)	4.9 (4)	4.5(4)	23(2)	17(2)	40(3)	58(2)
Percent Difference (%)	-23(10)	-20(13)	-36(6)	-36(6)	-12(10)	-23(11)	-17(9)	7(5)
Session 2 - Elderly (n = 29)								
0.8 - 1.8 cm	0.12(1)	0.09(1)	7.4(3)	6.8(2)	25(2)	20(1)	45(3)	55(1)
2.8 - 3.8 cm	0.10(1)	0.08(1)	5.7(3)	5.0(3)	21(1)	19(1)	40(2)	53(1)
Percent Difference (%)	-17(11)	-11(15)	-23(5)	-26(5)	-16(8)	-5(7)	-11(7)	-4(3)
Session 3 - Young (n = 19)								
0.8 - 1.8 cm	0.14(1)	0.13(1)	8.9(2)	7.5(2)	39(2)	21(1)	60(3)	64(2)
2.8 - 3.8 cm	0.14(1)	0.12(1)	7.2(4)	6.0(3)	39(3)	20(1)	59(4)	65(2)
Percent Difference (%)	0(10)	-8(10)	-19(5)	-20(5)	0(9)	-5(7)	-2(8)	2(4)

To assess the reproducibility of the measurements, we compared source-detector distances that were common to both sessions, namely from 2.0 to 3.5 cm in session 1 and from 2.3 to 3.3 cm in session 2. Figure 5.13 shows the correlation between values obtained in session 1 and 2.

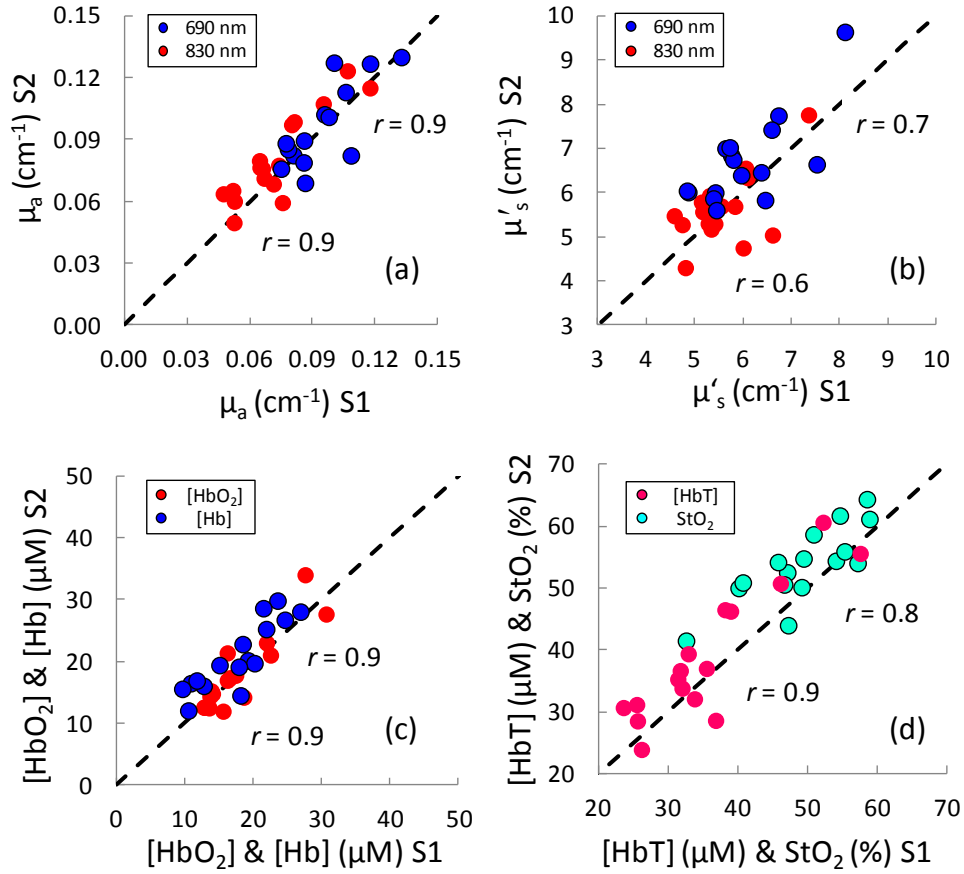


Figure 5.13. Measured parameters in session 2 as a function of corresponding parameters measured in session 1, illustrating the reproducibility of measurements taken five months apart on the same subjects. Dashed lines represent the ideal identity line to enhance reader’s visualization of the data.

Good agreement was found with cross-correlation coefficients of ~ 0.9 for both $\mu_a^{690\text{nm}}$ and $\mu_a^{830\text{nm}}$, ~ 0.7 and ~ 0.6 for $\mu'_s{}^{690\text{nm}}$ and $\mu'_s{}^{830\text{nm}}$, respectively, ~ 0.9 for both [HbO₂] and [Hb], and ~ 0.9 and ~ 0.8 for [HbT] and StO₂, respectively.

Figure 5.14 shows the comparable dependence of measured parameters on source-detector distance in elderly (session 2, $n = 29$) and young subjects (session 3, $n = 19$), despite differences in absolute values.

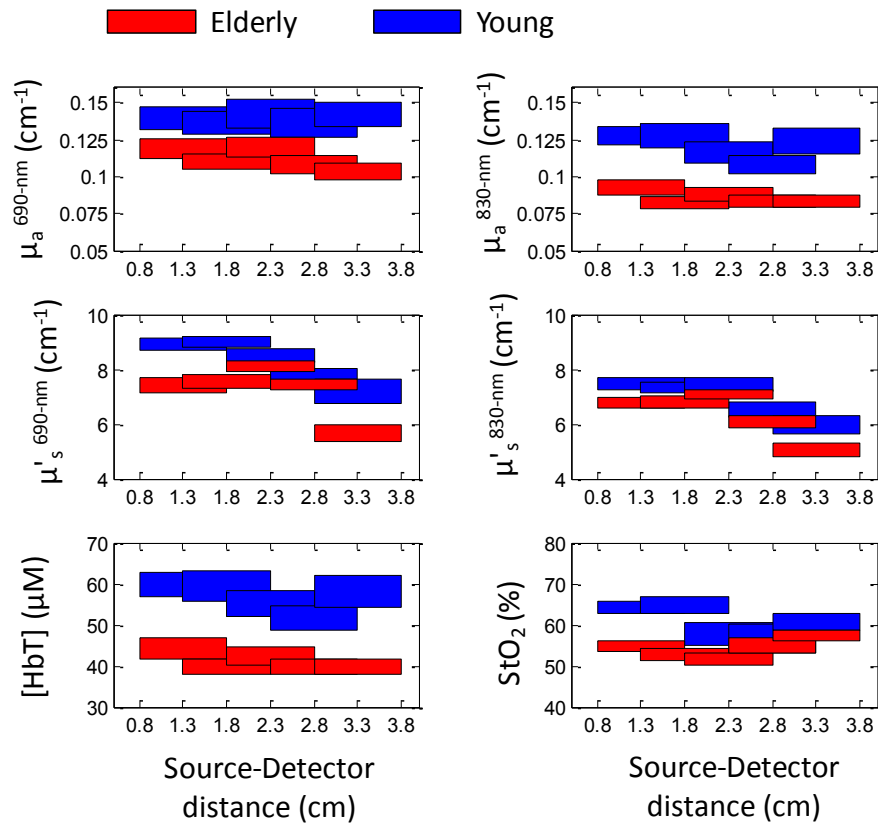


Figure 5.14. Dependence of measured parameters on source-detector separation in elderly and young subjects. Left and right top panels report measured μ_a at 690 and 830 nm, respectively. Left and right middle panels report measured μ'_s at 690 and 830 nm, respectively. Bottom left and right panels report measured [HbT] and StO_2 respectively. Red and blue blocks represent means (block center) and standard error (block thickness) of measurements in elderly and young subjects, respectively, at corresponding distances.

Red and blue bars represent the results for elderly and young subjects, respectively, over the corresponding source-detector distances (bar lengths), whereas bar centers represent means and bar widths represent standard errors. These results are also summarized in Table 5.3.

In order to make a meaningful comparison between physiological parameters in elderly and young subjects, we compared measurements at source-detector distances that were common to all three sessions, namely 2.0-3.5 cm in session 1 and 2.3-3.3 cm in sessions 2 and 3. We found significant differences between the two age groups in all measured parameters. Averages and standard errors across all subjects are presented in figure 5.15, where illustrations on the left and right sides of each graph represent measured parameters in the elderly and young subjects, respectively.

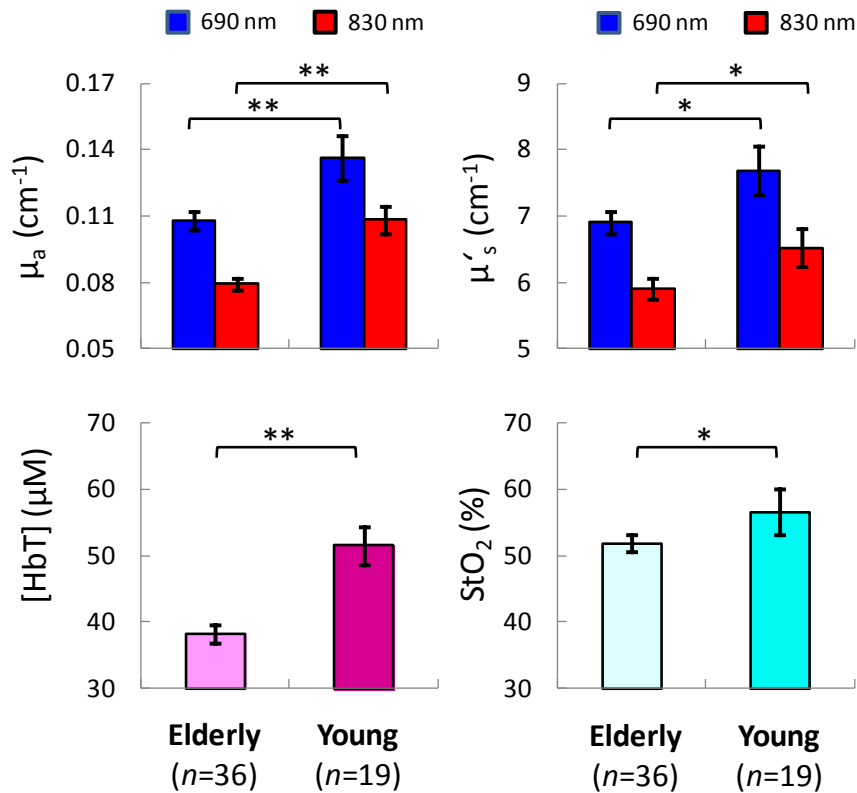


Figure 5.15. Mean and standard error of absolute measurements of optical properties, [HbO₂], [Hb], [HbT], and StO₂ in elderly and young human subjects (* $p < 0.05$, ** $p < 0.01$).

These results (including [HbO₂] and [Hb]) are summarized in Table 5.4.

Table 5.4. Summary of absolute measurements in elderly and young subjects. Values in parentheses represent the standard error on the last significant digit(s) of the mean.

	$\mu_a^{690\text{nm}}$ (cm^{-1})	$\mu_a^{830\text{nm}}$ (cm^{-1})	$\mu_s'^{690\text{nm}}$ (cm^{-1})	$\mu_s'^{830\text{nm}}$ (cm^{-1})	[HbO ₂] (μM)	[Hb] (μM)	[HbT] (μM)	StO ₂ (%)
Elderly	0.11(1)	0.08(1)	6.9(2)	6.0(2)	20(1)	18(1)	38(2)	52(2)
Young	0.13(1)	0.11(1)	7.7(4)	6.6(3)	30(3)	22(2)	52(3)	58(3)

5.3.3. Discussion of the results

The application of a homogeneous medium model to analyze non-invasive optical data collected on the subject's forehead is a first approximation to describe the heterogeneous composition of the probed tissue (skin, skull, brain, etc.). The multi-distance frequency domain approach over source-detector distances of 2.3–3.3 cm employed by us has been previously shown to be intrinsically insensitive to superficial tissue layers up to 4-5 mm (Franceschini *et al.* 1998), which addresses, at least in part, the layered inhomogeneity of the investigated forehead tissue. Nevertheless, the observed dependence of optical coefficients and hemoglobin parameters on source-detector separation (figures 12 and 14) implied a depth-dependence of the tissue composition, which is consistent with the head anatomy and with reports in the literature (Choi *et al.* 2004; Ohmae *et al.* 2006; Comelli *et al.* 2007; Gagnon *et al.* 2008). Despite this, we obtained reproducible absolute measurements in elderly subjects measured in two sessions (figures 5.12 and 5.13). This result is remarkable considering that the measurements were conducted five months apart with two different optical probes. Such reproducibility allows for a meaningful comparison across subjects, allowing us to observe significant differences in all measured parameters between elderly and young adults (figure 5.16). Based on the above arguments, such differences may be the result of anatomical differences, physiological

differences, or a combination of them. The reproducibility of measurements of cerebral blood volume in elderly subjects based on relative NIRS measurements of hemoglobin concentration has been previously reported (Claassen *et al.* 2006). To the best of our knowledge, ours was the first study showing a high level of reproducibility of absolute measurements of optical properties, hemoglobin concentration, and hemoglobin saturation in elderly subjects (figure 5.13).

Reproducibility of the results (figures 5.12 and 5.13) in the elderly subjects also served as strong evidence that measured differences between elderly and young individuals (figure 5.15) had a tissue origin. Such tissue origin, however, may be physiological (functional) and/or anatomical (structural), and the homogeneous medium model used here cannot directly discriminate between the two possibilities. Functional NIRS studies of brain activation (changes in hemoglobin concentrations and saturation) in response to cognitive challenges such as verbal fluency (rapid generation of words in a given period of time) (Kameyama *et al.* 2004; Herrmann *et al.* 2006), calculation (Hock *et al.* 1995; Richter *et al.* 2007) and paradigm determination (arrangement and modification of pictures) (Kwee and Nakada 2003) also report differences between elderly and young subjects. Even though a direct comparison between differences in changes as reported in these studies and absolute resting measurements as reported in this study is not possible, the physiological basis for these findings are expected to be related. I note also that one study has reported absolute optical properties and hemoglobin parameters on 13 subjects that implied a negative correlation between $[HbO_2]$ and subjects' ages (r -value = -0.60) (Gatto *et al.* 2007). It is noteworthy that we found a similar relation of $[HbO_2]$ to age (r -value = -0.58), even though Gatto *et al.*'s study was

smaller than ours (13 versus 55, respectively) and examined a narrower age range (26-59 versus 24-89). The observation of lower absolute brain tissue hemoglobin concentrations and oxygen saturation in the elderly subjects are likely to have clinical significance indicating cerebral microvascular rarefaction (Brown and Thore 2011) or age dependent impairment in cerebral perfusion and metabolism and associated neuropathology.

Water is a major tissue constituent that must be incorporated in the interpretation of optically measured hemoglobin concentrations. A range of values for volume fraction of water content in tissue (C_{H_2O-vf}) have been reported in different studies, from 0.3 (Iadecola 2010), to 0.7 (Quaresima *et al.* 2005), and 0.8 (Ohmae *et al.* 2006; Gagnon *et al.* 2008). In some cases C_{H_2O-vf} was not specified (Torricelli *et al.* 2001; Comelli *et al.* 2007), or was not mentioned (Leung *et al.* 2006). Equations (5.6) and (5.7) can be used to estimate errors in $[HbO_2]$ and $[Hb]$ due to errors in the assumed C_{H_2O-vf} values. These equations predict that assuming no water content in the probed tissue (i.e. $C_{H_2O-vf} = 0$) results in measurements of $[HbO_2]$ that are greater than the actual values by 4.5, 10.4 and 11.9 μM , and measurements of $[Hb]$ that are less than the actual values by 0.6, 1.3 and 1.5 μM , for cases in which C_{H_2O-vf} values are 0.3, 0.7 and 0.8, respectively. The relevance of taking into account the proper contribution of water absorption may, to some extent, explain differences in findings between labs and underscores the need to explicitly consider C_{H_2O-vf} in absolute NIRS measurements in cerebral tissues.

Another potential source of error is the calibration procedure. Phantom calibration for absolute NIRS measurements is a delicate protocol that requires precision in the calibration parameters (i.e. optical properties of the phantom) to avoid errors in the estimation of hemoglobin concentrations. For our measurements, we employed an

additional calibration-free protocol to measure the optical properties of the calibration phantom as described in Appendix B, which minimizes errors in the assignment of phantom optical properties to less than 5%. This in turn translates into errors of less than 4% in the measurement of tissue hemoglobin concentration. StO₂ measurements, which are determined by ratios of tissue absorption at two wavelengths, are insensitive to calibration errors.

Cerebral total hemoglobin concentration and oxygen saturation values reported in this study in young subjects ($52 \pm 13 \mu\text{M}$ and $58\% \pm 9\%$, respectively) are similar to those reported in Gagnon *et al.* ($51 \pm 11 \mu\text{M}$ and $60\% \pm 4\%$) evaluated by a time-domain system and in Gatto *et al.* ($42 \pm 13\mu\text{M}$ and $57\% \pm 7\%$), who used a frequency-domain system. Lower total hemoglobin concentration values reported in Gatto *et al.* may be representative of the older age group that was investigated in that study. Such hemoglobin oxygen saturation values around 60% may reflect the large oxygen consumption in the brain and/or sensitivity of non-invasive NIRS measurements to the venous compartment, whose oxygen saturation has been reported to be around 62% (Gibbs *et al.* 1942). To further extend our comparison with other studies, Ohmae *et al.* measured comparable total hemoglobin concentration and higher oxygen saturation values ($54 \pm 6 \mu\text{M}$ and $70\% \pm 2\%$) using a time-domain system. In an independent time-domain approach, Quaresima *et al.* reported higher values for both total hemoglobin concentration and oxygen saturation ($70 \pm 10 \mu\text{M}$ and $70\% \pm 3\%$). Small $C_{\text{H}_2\text{O}-\text{vf}}$ values considered in that study (0.3) relative to ours (0.7) could partially account for the greater hemoglobin concentration and oxygen saturation values. In addition, differences in probed tissue volumes between the multi-distance approach employed by us (with its

suppressed sensitivity to the most superficial tissue layers) and single-distance approach by Ohmae *et al.* and Quaresima *et al.* are other plausible causes for the differences in measured hemoglobin parameters. Finally, Choi *et al.* reported considerably higher total hemoglobin concentration and oxygen saturation values ($77 \pm 14 \mu\text{M}$ and $74\% \pm 6\%$) using a frequency-domain instrument. Differences in the results of that study and ours may have a basis on a combination of effects including differences in water correction (no $C_{\text{H}_2\text{O-vf}}$ was mentioned in that study), calibration methods (optical properties of the calibration phantom was not determined independently in that study), and source-detector distances (much larger distances were used in that study – 4.5–7cm).

References for Chapter 5

- Brown, W. R. and C. R. Thore (2011). "Review: cerebral microvascular pathology in ageing and neurodegeneration." Neuropathol Appl Neurobiol **37**(1): 56-74.
- Capraro, G. A., T. J. Mader, B. F. Coughlin, C. Lovewell, M. R. St Louis, M. Tirabassi, G. Wadie and H. A. Smithline (2007). "Feasibility of using near-infrared spectroscopy to diagnose testicular torsion: an experimental study in sheep." Annals of emergency medicine **49**(4): 520-525.
- Cerussi, A. E., J. S. Maier, S. Fantini, M. A. Franceschini and E. Gratton (1996). The Frequency-Domain Multi-Distance Method in the Presence of Curved Boundaries. OSA Trends in Optics and Photonics on Biomedical Optical Spectroscopy and Diagnostics. E. S. Muraca and D. Benaron. Orlando, FL. **3**: 92-97.
- Choi, J., M. Wolf, V. Toronov, U. Wolf, C. Polzonetti, D. Hueber, L. P. Safonova, R. Gupta, A. Michalos, W. Mantulin and E. Gratton (2004). "Noninvasive determination of the optical properties of adult brain: near-infrared spectroscopy approach." J Biomed Opt **9**(1): 221-229.
- Claassen, J. A., W. N. Colier and R. W. Jansen (2006). "Reproducibility of cerebral blood volume measurements by near infrared spectroscopy in 16 healthy elderly subjects." Physiol Meas **27**(3): 255-264.
- Clarke, R., A. D. Smith, K. A. Jobst, H. Refsum, L. Sutton and P. M. Ueland (1998). "Folate, vitamin B12, and serum total homocysteine levels in confirmed Alzheimer disease." Arch Neurol **55**(11): 1449-1455.
- Colier, W., F. Froeling, J. De Vries and B. Oeseburg (1995). "Measurement of the blood supply to the abdominal testis by means of near infrared spectroscopy." European urology **27**(2): 160-166.
- Comelli, D., A. Bassi, A. Pifferi, P. Taroni, A. Torricelli, R. Cubeddu, F. Martelli and G. Zaccanti (2007). "In vivo time-resolved reflectance spectroscopy of the human forehead." Appl Opt **46**(10): 1717-1725.
- Dayal, S., E. Arning, T. Bottiglieri, R. H. Boger, C. D. Sigmund, F. M. Faraci and S. R. Lentz (2004). "Cerebral vascular dysfunction mediated by superoxide in hyperhomocysteinemic mice." Stroke **35**(8): 1957-1962.
- Dayal, S. and S. R. Lentz (2008). "Murine models of hyperhomocysteinemia and their vascular phenotypes." Arterioscler Thromb Vasc Biol **28**(9): 1596-1605.
- Fantini, S. (2002). "A haemodynamic model for the physiological interpretation of in vivo measurements of the concentration and oxygen saturation of haemoglobin." Phys Med Biol **47**(18): N249-257.
- Fantini, S., M. A. Franceschini, J. B. Fishkin, B. Barbieri and E. Gratton (1994). "Quantitative determination of the absorption spectra of chromophores in strongly scattering media: a light-emitting-diode based technique." Appl Opt **33**(22): 5204-5213.
- Fantini, S., M. A. Franceschini and E. Gratton (1994). "Semi-infinite-geometry boundary problem for light migration in highly scattering media: a frequency-domain study in the diffusion approximation." J Opt Soc Am **11**(10): 2128-2138.

- Franceschini, M. A., S. Fantini, L. A. Paunescu, J. S. Maier and E. Gratton (1998). "Influence of a superficial layer in the quantitative spectroscopic study of strongly scattering media." Appl Opt **37**(31): 7447-7458.
- Gagnon, L., C. Gauthier, R. D. Hoge, F. Lesage, J. Selb and D. A. Boas (2008). "Double-layer estimation of intra- and extracerebral hemoglobin concentration with a time-resolved system." J Biomed Opt **13**(5): 054019.
- Gatto, R., W. E. Hoffman, M. Mueller, C. Paisansathan and F. Charbel (2007). "Age effects on brain oxygenation during hypercapnia." J Biomed Opt **12**(6): 062113.
- Gibbs, E. L., W. G. Lennox, L. F. Nims and F. A. Gibbs (1942). "Arterial and cerebral venous blood. Arterial differences in man." J. Biol. Chem. **144**: 325-332.
- Graaff, R., J. G. Aarnoudse, J. R. Zijp, P. M. A. Sloot, F. F. M. Demul, J. Greve and M. H. Koelink (1992). "Reduced light-scattering properties for mixtures of spherical-particles - a simple approximation derived from mie calculations." Applied Optics **31**(10): 1370-1376.
- Hale, G. M. and M. R. Querry (1973). "Optical Constants of Water in the 200-nm to 200-microm Wavelength Region." Appl Opt **12**(3): 555-563.
- Hampel, U., E. Schleicher and R. Freyer (2002). "Volume image reconstruction for diffuse optical tomography." Appl Opt **41**(19): 3816-3826.
- Hare, G. M. (2004). "Anaemia and the brain." Curr Opin Anaesthesiol **17**(5): 363-369.
- Herrmann, M. J., A. Walter, A. C. Ehlis and A. J. Fallgatter (2006). "Cerebral oxygenation changes in the prefrontal cortex: effects of age and gender." Neurobiol Aging **27**(6): 888-894.
- Hock, C., F. Muller-Spahn, S. Schuh-Hofer, M. Hofmann, U. Dirnagl and A. Villringer (1995). "Age dependency of changes in cerebral hemoglobin oxygenation during brain activation: a near-infrared spectroscopy study." J Cereb Blood Flow Metab **15**(6): 1103-1108.
- Iadecola, C. (2010). "The overlap between neurodegenerative and vascular factors in the pathogenesis of dementia." Acta Neuropathol **120**(3): 287-296.
- Kado, D. M., A. S. Karlamangla, M. H. Huang, A. Troen, J. W. Rowe, J. Selhub and T. E. Seeman (2005). "Homocysteine versus the vitamins folate, B6, and B12 as predictors of cognitive function and decline in older high-functioning adults: MacArthur Studies of Successful Aging." Am J Med **118**(2): 161-167.
- Kalaria, R. N., D. L. Cohen, D. R. Premkumar, S. Nag, J. C. LaManna and W. D. Lust (1998). "Vascular endothelial growth factor in Alzheimer's disease and experimental cerebral ischemia." Brain Res Mol Brain Res **62**(1): 101-105.
- Kalfa, N., C. Veyrac, C. Baud, A. Couture, M. Averous and R. B. Galifer (2004). "Ultrasonography of the spermatic cord in children with testicular torsion: impact on the surgical strategy." J Urol **172**(4 Pt 2): 1692-1695; discussion 1695.
- Kameyama, M., M. Fukuda, T. Uehara and M. Mikuni (2004). "Sex and age dependencies of cerebral blood volume changes during cognitive activation: a multichannel near-infrared spectroscopy study." Neuroimage **22**(4): 1715-1721.
- Karmazyn, B., R. Steinberg, L. Kornreich, E. Freud, S. Grozovski, M. Schwarz, N. Ziv and P. Livne (2005). "Clinical and sonographic criteria of acute scrotum in children: a retrospective study of 172 boys." Pediatr Radiol **35**(3): 302-310.

- Kim, J. M., H. Lee and N. Chang (2002). "Hyperhomocysteinemia due to short-term folate deprivation is related to electron microscopic changes in the rat brain." J Nutr **132**(11): 3418-3421.
- Koh, K. B., N. Dublin and T. Light (1995). "Testicular torsion." Aust N Z J Surg **65**(9): 645-646.
- Kohl, M., U. Lindauer, U. Dirnagl and A. Villringer (1998). "Separation of changes in light scattering and chromophore concentrations during cortical spreading depression in rats." Opt Lett **23**(7): 555-557.
- Kwee, I. L. and T. Nakada (2003). "Dorsolateral prefrontal lobe activation declines significantly with age--functional NIRS study." J Neurol **250**(5): 525-529.
- LaManna, J. C., J. C. Chavez and P. Pichiule (2004). "Structural and functional adaptation to hypoxia in the rat brain." J Exp Biol **207**(Pt 18): 3163-3169.
- Leung, T. S., I. Tachtsidis, M. Smith, D. T. Delpy and C. E. Elwell (2006). "Measurement of the absolute optical properties and cerebral blood volume of the adult human head with hybrid differential and spatially resolved spectroscopy." Phys Med Biol **51**(3): 703-717.
- Nussbaum Blask, A. R., D. Bulas, E. Shalaby-Rana, G. Rushton, C. Shao and M. Majd (2002). "Color Doppler sonography and scintigraphy of the testis: a prospective, comparative analysis in children with acute scrotal pain." Pediatr Emerg Care **18**(2): 67-71.
- Ohmae, E., Y. Ouchi, M. Oda, T. Suzuki, S. Nobesawa, T. Kanno, E. Yoshikawa, M. Futatsubashi, Y. Ueda, H. Okada and Y. Yamashita (2006). "Cerebral hemodynamics evaluation by near-infrared time-resolved spectroscopy: correlation with simultaneous positron emission tomography measurements." Neuroimage **29**(3): 697-705.
- Quaresima, V., M. Ferrari, A. Torricelli, L. Spinelli, A. Pifferi and R. Cubeddu (2005). "Bilateral prefrontal cortex oxygenation responses to a verbal fluency task: a multichannel time-resolved near-infrared topography study." J Biomed Opt **10**(1): 11012.
- Richter, M. M., M. J. Herrmann, A. C. Ehlis, M. M. Plichta and A. J. Fallgatter (2007). "Brain activation in elderly people with and without dementia: Influences of gender and medication." World J Biol Psychiatry **8**(1): 23-29.
- Selhub, J., L. C. Bagley, J. Miller and I. H. Rosenberg (2000). "B vitamins, homocysteine, and neurocognitive function in the elderly." Am J Clin Nutr **71**(2): 614S-620S.
- Smielewski, P., P. Kirkpatrick, P. Minhas, J. Pickard and C. M. (1995). "Can cerebrovascular reactivity be measured with near-infrared spectroscopy." Stroke **26**: 2285-2292.
- Snowdon, D. A., L. H. Greiner, J. A. Mortimer, K. P. Riley, P. A. Greiner and W. R. Markesbery (1997). "Brain infarction and the clinical expression of Alzheimer disease. The Nun Study." JAMA **277**(10): 813-817.
- Techawiboonwong, A., H. K. Song, M. B. Leonard and F. W. Wehrli (2008). "Cortical bone water: in vivo quantification with ultrashort echo-time MR imaging." Radiology **248**(3): 824-833.

- Torricelli, A., A. Pifferi, P. Taroni, E. Giambattistelli and R. Cubeddu (2001). "In vivo optical characterization of human tissues from 610 to 1010 nm by time-resolved reflectance spectroscopy." Phys Med Biol **46**(8): 2227-2237.
- Troen, A. and I. Rosenberg (2005). "Homocysteine and cognitive function." Semin Vasc Med **5**(2): 209-214.
- Troen, A. M., W. H. Chao, N. A. Crivello, K. E. D'Anci, B. Shukitt-Hale, D. E. Smith, J. Selhub and I. H. Rosenberg (2008). "Cognitive impairment in folate-deficient rats corresponds to depleted brain phosphatidylcholine and is prevented by dietary methionine without lowering plasma homocysteine." J Nutr **138**(12): 2502-2509.
- Troen, A. M., M. Shea-Budgell, B. Shukitt-Hale, D. E. Smith, J. Selhub and I. H. Rosenberg (2008b). "B-vitamin deficiency causes hyperhomocysteinemia and vascular cognitive impairment in mice." Proc Natl Acad Sci U S A **105**(34): 12474-12479.
- Vernieri, F., F. Tibuzzi, P. Pasqualetti, C. Altamura, P. Palazzo, P. M. Rossini and M. Silvestrini (2008). "Increased cerebral vasomotor reactivity in migraine with aura: an autoregulation disorder? A transcranial Doppler and near-infrared spectroscopy study." Cephalalgia **28**(7): 689-695.
- Vovenko, E. P. and A. E. Chuikin (2008). "Oxygen tension in rat cerebral cortex microvessels in acute anemia." Neurosci Behav Physiol **38**(5): 493-500.
- Williamson, R. C. (1976). "Torsion of the testis and allied conditions." Br J Surg **63**(6): 465-476.
- Woodard, H. Q. and D. R. White (1986). "The composition of body tissues." Br J Radiol **59**(708): 1209-1218.
- Wray, S., M. Cope, D. T. Delpy, J. S. Wyatt and E. O. Reynolds (1988). "Characterization of the near infrared absorption spectra of cytochrome aa3 and haemoglobin for the non-invasive monitoring of cerebral oxygenation." Biochim Biophys Acta **933**(1): 184-192.

Chapter 6

Experimental Studies based on Two-Layered Modeling

In this chapter, I report absolute measurements of the optical coefficients of two-layered media that expand on the experimental studies that I have described in Chapter 5. I present the application of the inversion procedure (that was introduced in Chapter 4) to translate multi-distance optical data into measurements of the absolute values of the optical coefficients in both layers, as well as the top layer thickness. When applied to optical measurements on the human head, this method yields hemoglobin concentrations and saturation in the extracerebral tissue (layer 1) and in the cerebral tissue (layer 2), as well as the depth of the cerebral cortex (scalp-cortex distance). The method, relies on our own implementation of Levenberg-Marquardt inversion procedure (as described in Chapter 4) applied to the two-layer solution of the diffusion equation (as described in Chapter 2).

Specific content of this chapter is as follows. In Section 6.1, I present a homogenous liquid phantom that was used for all reference measurements. In Section 6.2, results on simulated and two-layered phantom data are presented. Also in Section

6.2, I compare the performance of homogenous and two-layered analysis on optical data collected on two-layered phantoms. Finally, in Section 6.3, I demonstrate the application of the two-layered approach on data collected on the human forehead. In this section, I also make a comparison between homogenous and two-layered analyses.

6.1. Homogenous Phantom Measurements

6.1.1. Methods

We used liquid phantoms for all the phantom measurements that will be described in this chapter. The same recipe was employed for both homogenous and two-layered liquid phantoms. In order to measure the absolute optical properties of these phantoms, we performed infinite medium measurements as described in Chapter 2 (Section 2.2.1). The measurements were conducted in a large container (dimensions given in figure 6.1) in order to obtain an effectively infinite geometry arrangement (Chapter 2, figure 2.1), in which optical detector and source fibers (both 400 μm in diameter) were deeply immersed into the medium (at a depth of ~ 60 mm) and parallel to each other. This is a typical experimental arrangement for absolute optical characterization of liquid phantoms using NIRS, where the diffused intensity is generated and detected only within the diffusing medium avoiding any complications due to the boundary conditions. An illustration of the experimental setup is provided in figure 6.1.

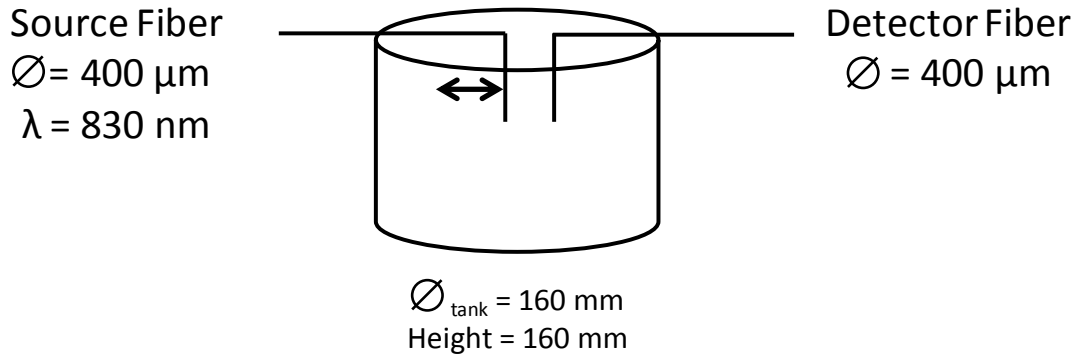


Figure 6.1. A pictorial illustration of the homogenous phantom setup in the infinite geometry arrangement.

The container was filled with controlled suspensions of deionized water, Intralipid 20% (Manufacturer Fresenius Kabi, Germany) and diluted India Ink (weight fraction of ink in water = 0.0074) for background dilution, scattering and absorption characteristics, respectively. Intralipid is an intravenous fat emulsion that has been widely used as a highly scattering tissue-like phantom (van Staveren *et al.* 1991; Flock *et al.* 1992; Bevilacqua *et al.* 1999; Di Ninni *et al.* 2011; Di Ninni *et al.* 2012). We followed a common experimental protocol (Fantini *et al.* 1994), where we employed an illumination fiber (400 μm diameter) delivering 830 nm wavelength of light and linearly scanned it away from the collection fiber by means of a programmable mechanical linear stage scanning system (Velmex Inc., Bloomfield, NY, USA) over the source–detector distances of ~ 20 to 35 mm. This procedure was repeated twenty times for eight different homogenous phantom preparations. The acquisition was automated and controlled by a program written in LabVIEW software (National Instruments, Austin, TX, USA). By exploiting the linear dependence of μ_a and μ'_s on the concentration of ink and Intralipid, respectively, we obtained: 1) intrinsic optical coefficients of pure Intralipid and ink; and

2) linear expressions that provided an independent means to characterize each medium that was used for the two-layered measurements.

6.1.2. Results of the Infinite Medium Measurements

We found a linear dependence of μ_a and μ'_s on India ink and Intralipid concentrations, respectively. These results are shown in figure 6.2, whereby we report measured μ_a and μ'_s at 830 nm as a function of volume fractions of diluted-ink and Intralipid. These are typical results for such experiments in the infinite geometry (Fantini *et al.* 1994; Martelli and Zaccanti 2007; Spinelli *et al.* 2007), which in fact confirm that the infinite boundary conditions were met during our measurements. We performed linear regression analysis on the experimental data and computed the slopes of μ_a and μ'_s to be 2.1 ± 0.1 ($\text{mm}^{-1}/\% \text{diluted-ink}$) and 19.2 ± 1.2 ($\text{mm}^{-1}/\% \text{Intralipid}$), respectively.

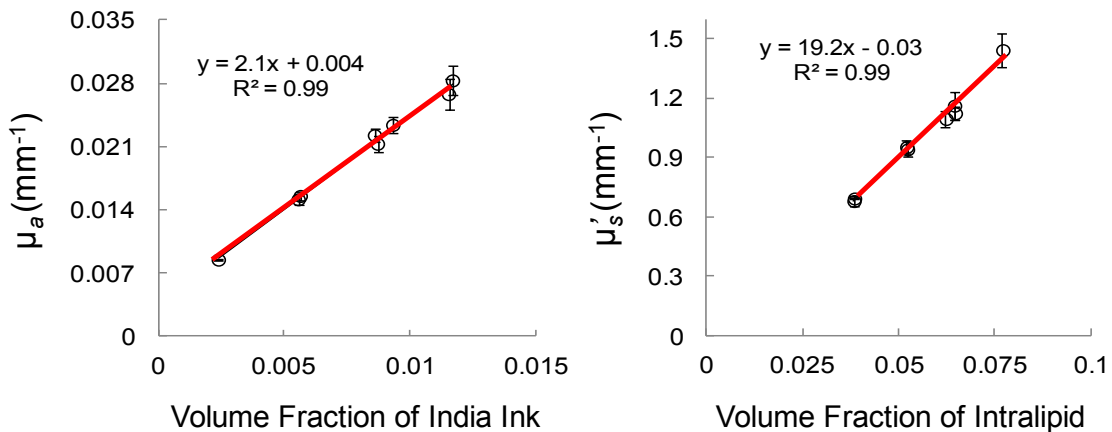


Figure 6.2. Measurement of μ_a (left panel) and μ'_s (right panel) at 830 nm wavelength on eight homogenous phantoms in the infinite geometry, presented as a function of volume fractions of ink dilution and intralipid, respectively. The symbols and error bars represent mean and standard deviation of 20 independent measurements in each phantom. The slopes of the linear curves were used to characterize the precise quantities used in the two-layered phantom measurements.

We note that these slopes represent the intrinsic μ_a and μ'_s per unit concentration of diluted-ink and pure-intralipid, respectively, which were used for the accurate optical characterization of the suspensions used in the two-layered phantom measurements. We evaluated the intrinsic μ_a of pure-ink to be 281.8 ± 13.6 ($\text{mm}^{-1}/\%$ ink). This led to infinite medium measurement uncertainties of $\sim 6\%$ for both μ_a and μ'_s . The y -intercepts of diluted-ink and Intralipid regression lines ($0.004 \pm 0.001 \text{ mm}^{-1}$ and $-0.03 \pm 0.04 \text{ mm}^{-1}$, respectively) represent our measured μ_a and μ'_s of pure water (figure 6.2). Although these values should be equal to the actual μ_a and μ'_s of water at 830 nm wavelength ($\mu_a = \sim 0.003 \text{ mm}^{-1}$ (Hale and Querry 1973) and $\mu'_s = 0 \text{ mm}^{-1}$, respectively), the actual values were within the measurement uncertainties.

6.2. Two-layered Monte Carlo Simulations and Phantom Measurements

6.2.1. Methods

For the Monte Carlo simulations, we followed the protocol described in Chapter 4. Simulations were run with refractive index pairs of 1 and 1.4 (for air and two-layered scattering media, respectively), and 1.56 and 1.33 [for surrounding medium (plastic scattering cell) and two-layered medium used in the phantom experiments (Intralipid 20%, Fresenius Kabi, Germany)], according to Mie theory with anisotropy coefficient $g = 5.15 \times 10^{-8}$ and a Henyey-Greenstein phase function with $g = 0.8$.

For the two-layered phantom experiments, we used a two-layered liquid phantom (Del Bianco *et al.* 2004), where the layers were separated by means of a thin (23 μm) Mylar membrane. Effects of Mylar to diffuse reflectance measurements in the near-infrared region have been shown to be negligible (Martelli *et al.* 2004). An illustration of the phantom that was used in this work is provided in figure 6.3. The phantom featured thirteen transparent optical windows at the center of its façade including one detection window (3 mm diameter) and twelve illumination windows (1 mm diameter each). Separation of the windows ranged from 6 to 50 mm. The overall dimensions of the phantom to ensure the validity of semi-infinite boundary conditions for layer 2 for a given thicknesses of layer 1 (in z -direction) were determined through Monte Carlo simulations. These dimensions are presented in figure 6.3.

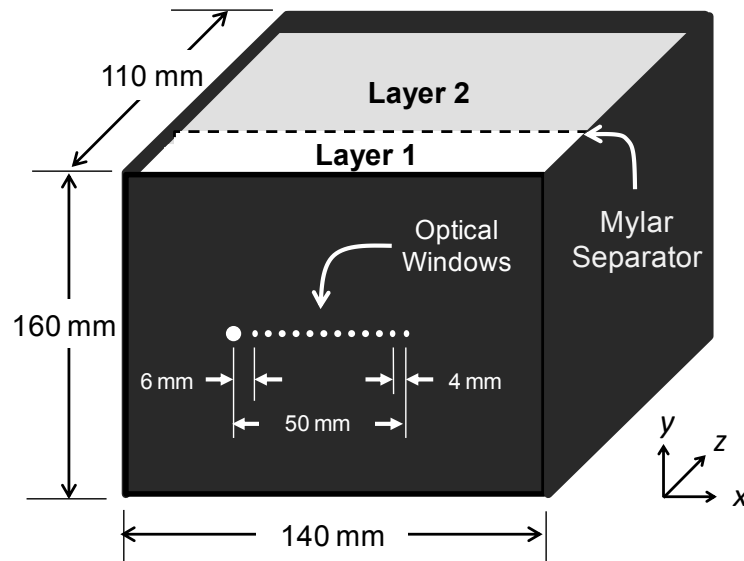


Figure 6.3. Illustration of the two-layered liquid phantom (Del Bianco *et al.* 2004), where larger and smaller optical windows denote detector and source fiber positions, respectively (Del Bianco *et al.* 2004).

The two layers were filled with controlled suspensions of deionized water, Intralipid 20% and diluted India Ink, again, for background dilution, scattering and absorption characteristics, respectively. Scattering and absorption coefficients of the two layers were controlled by changing the amount of Intralipid and ink in each layer. We performed multi-distance frequency-domain diffuse reflectance measurements on twelve different two-layered phantom preparations for three different first layer thicknesses (8, 10, and 15 mm). Apart from 8 mm, such first layer thicknesses match true anatomical values of scalp-cortex distance in the adult human forehead (~12–16 mm) (Haeussinger *et al.* 2011). Data from the two-layered phantoms were analyzed using the matching model, where the parameter vector was and the six-parameter inversion routine described in Chapter 3. As a reminder, here the parameter vector was: $\mathbf{x} = [\mu_{a1}, \mu'_{s1}, L, \mu_{a2}, \mu'_{s2}, AF]^T$. Even though the data was collected between 6–50 mm source-detector distances, the range considered for the analysis was 14–50 mm (i.e. starting from the third optical window) to comply with the diffusion conditions.

6.2.2. Results of the Monte Carlo Simulations

Recovered values from all eight Monte Carlo (MC) data sets were in good agreement with the actual values for all five parameters ($\mu_{a1}, \mu'_{s1}, L, \mu_{a2}, \mu'_{s2}$). We report these results in figure 6.4 in terms of MC data set (from 1 through 8), where the error bars represent uncertainties associated with the fitting procedure.

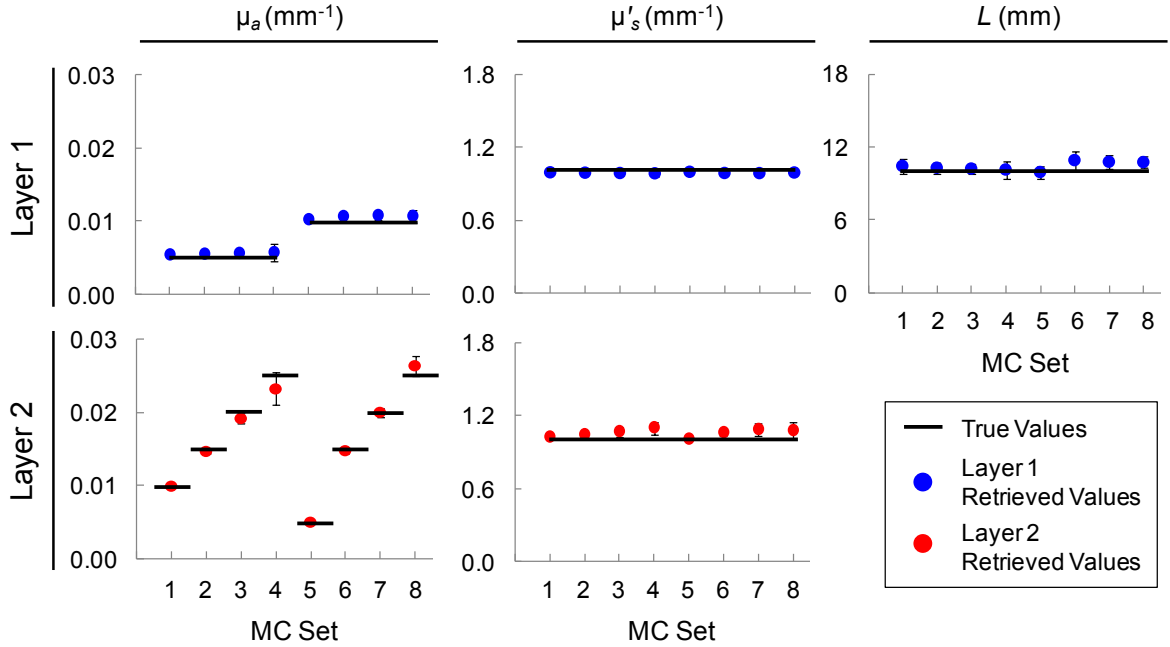


Figure 6.4. Six-parameter fitting procedure results on eight sets of two-layered Monte Carlo (MC) simulations reported in terms of MC set. *True values* represent values used for μ_a (column 1), μ'_s (column 2), and first layer thickness (column 3) in each MC simulation. Retrieved values for Layer 1 (row 1) and Layer 2 (row 2) are represented by open and filled circles, respectively. The error bars represent uncertainties determined by the fitting procedure.

All five parameters for most MC sets were recovered within 10% of the actual values. In two of the simulations (namely, MC sets: 3 and 4), where the absorption coefficient of layer 1 ($\mu_{a1} = 0.005 \text{ mm}^{-1}$) was significantly different than that of layer 2 ($\mu_{a2} = 0.02 \text{ mm}^{-1}$ for No. 3; and $\mu_{a2} = 0.025 \text{ mm}^{-1}$ for No. 4), μ_{a1} values were recovered with slightly larger errors (*i.e.* 12% for No. 3; and 14% for No. 4). However, deviations from the actual values for all other parameters in these simulations were still <10%. We note that the discrepancy between MC and DE would mostly account for these errors. To investigate this point, we have also carried out separate measurements on synthetic data generated using our forward model with additive noise (typically 1% random noise). We

found a more accurate recovery of the true values in these data sets, with deviations never exceeding a few percent and always smaller (as it is expected) than those found in the MC data (data not shown).

Our sensitivity analysis showed negligible effects of initial guesses for the parameter values in the inversion procedure. We demonstrate the method’s lack of sensitivity to initial guesses in Table 6.1, where two sets of initial guesses (i.e. “good” set and “bad” set) and retrieved values on the same representative data set is reported. As demonstrated in the Table 6.1, deviations between the retrieved and true values were less than 7% in both cases. This is a particularly important result demonstrating the method’s lack of sensitivity to local minima.

Table 6.1. Demonstration of the insensitivity of the inversion procedure to initialization. Similar convergence to good and bad initialization is reported

	μ_{a1} (mm ⁻¹)	μ'_{s1} (mm ⁻¹)	L (mm)	μ_{a2} (mm ⁻¹)	μ'_{s2} (mm ⁻¹)
True Values	0.0050	1.00	10.0	0.0100	1.00
Good Initial Guess	0.0060	1.20	8.0	0.0120	1.20
Retrieved Values	0.0053	0.99	10.2	0.0098	1.02
<i>Error on Initial Guess</i>	20%	20%	-20%	20%	20%
<i>Error on Retrieved Values</i>	7%	-1%	2%	-2%	2%
Bad Initial Guess	0.0100	3.00	1.0	0.0200	2.00
Retrieved Values	0.0054	0.99	10.4	0.0099	1.02
<i>Error on Initial Guess</i>	100%	200%	-90%	100%	100%
<i>Error on Retrieved Values</i>	7%	-1%	4%	-1%	2%

6.2.3. Results of the Two-layered Phantom Measurements

Moving onto phantom measurements, in figure 6.5, we report the results of a representative two-layered phantom measurement including the resulting fit (solid lines) on measurements (circles) of AC (left panel) and phase (right panel) as a function of

source-detector distance. Dotted lines illustrate the results yielded by the first iteration of the inversion procedure (using the initial guesses).

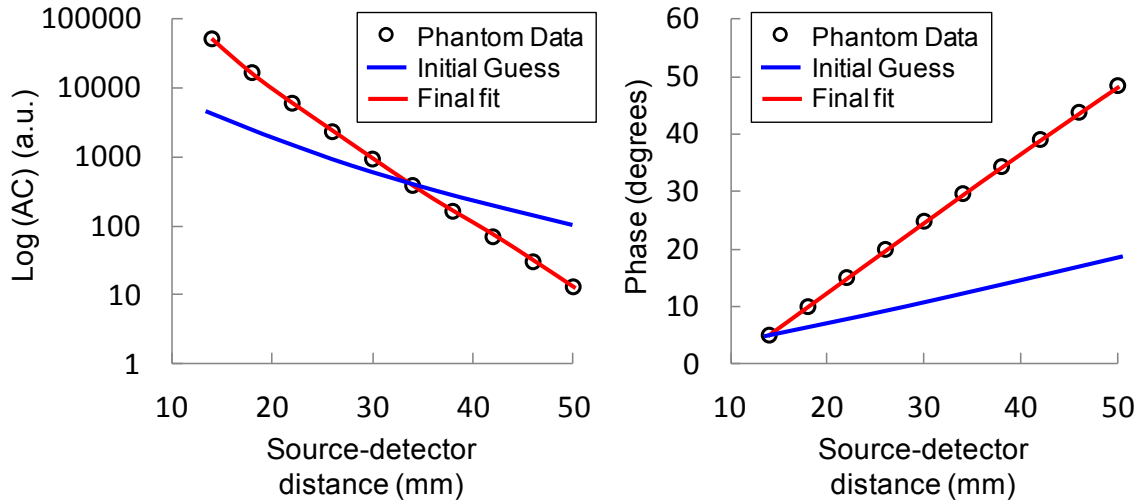


Figure 6.5. A representative case illustrating the final fit (solid lines) on measurements (circles) of AC attenuation (left panel) and phase shift (right panel) as a function of source-detector distance from the two-layer phantom. Dotted lines illustrate the results yielded by the first iteration of the inversion procedure (using the initial guesses). Final fit was obtained at the 102nd iteration.

In figure 6.6, we present the evolution of the six fitted parameters $[\mu_{a1}, \mu'_{s1}, L, \mu_{a2}, \mu'_{s2}, AF]$ for the same phantom considered in figure 6.5 during all iterations involved in the fitting procedure, which demonstrate the robustness of the inversion procedure and once again its insensitivity to initial guesses. Here results are presented for every other iteration for clarity. Horizontal solid and dashed lines represent the true values, measured independently in the infinite geometry using a homogenous model as described in Section 6.1.

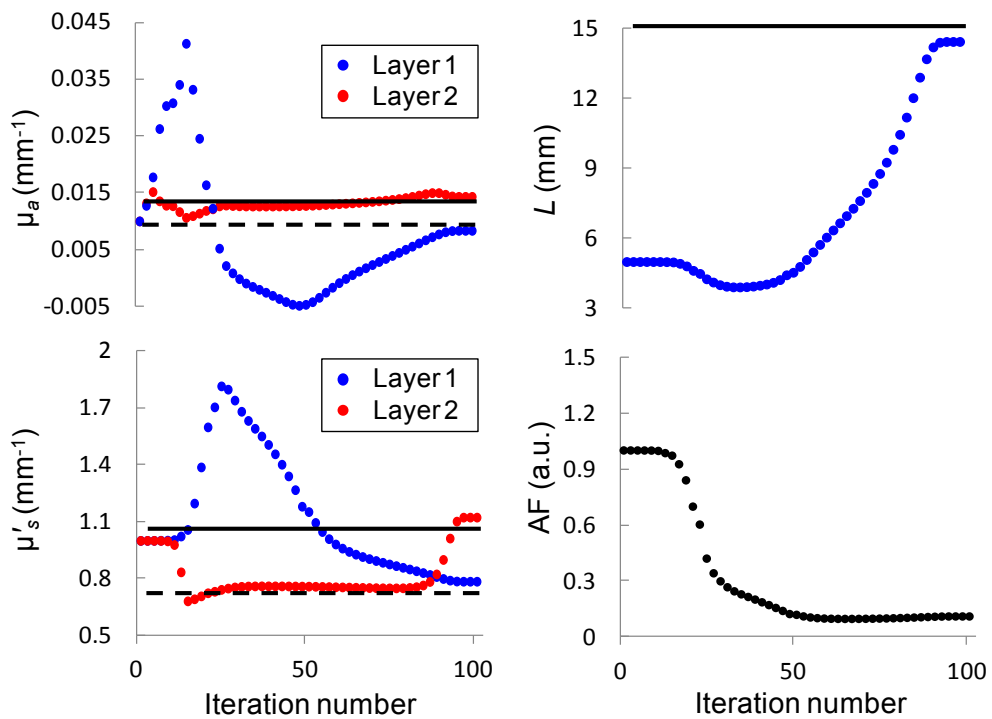


Figure 6.6. A representative case illustrating the evolution of the six parameters (μ_{a1} , μ'_{s1} , L , μ_{a2} , μ'_{s2} and AF) during the fitting procedure on two-layered phantom data, demonstrating the robustness of the inversion procedure and its insensitivity to initial guesses. Solid and dashed lines represent true values, measured independently in the infinite geometry.

Results of the two-layered phantom measurements for all twelve phantoms are reported in figure 6.7, where the error bars represent uncertainties associated with the fitting procedure.

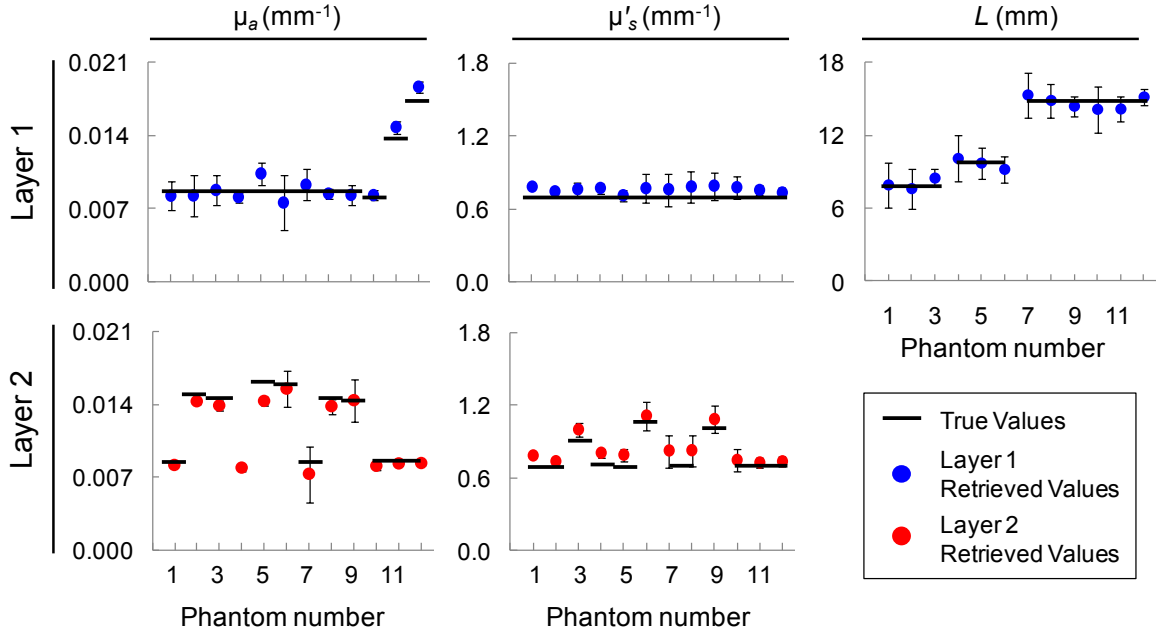


Figure 6.7. Six-parameter fitting procedure results on twelve two-layered phantoms with a range of optical coefficients and top-layer thicknesses that are representative of the human brain. *True values* represent quantities measured in the infinite medium geometry using a homogenous model. Retrieved values for layer 1 (row 1) and layer 2 (row 2) are represented by open and filled circles, respectively. The error bars represent uncertainties determined by the fitting procedure.

Considering the complexity of liquid phantom measurements, we have found excellent agreement between the true values and the retrieved values (*i.e.* measured from two-layered phantoms and retrieved simultaneously using our two-layered inversion routine). In fact, taking into account all two-layered phantom measurements [*i.e.* 12 phantoms \times 5 key parameters (μ_{a1} , μ'_{s1} , L , μ_{a2} , μ'_{s2}) = 60 parameters in total] more than 75% of the retrieved parameters were within 10% of the true values, half of which were within 5% of the true values. More specifically, the most accurately retrieved parameters in the two-layered phantom measurements were L and μ_{a2} , with ranges of absolute % deviations of 1% – 8% and 3% – 13%, respectively, from the true values.

Subsequently, ranges of absolute % deviations in μ_{a1} , μ'_{s1} , μ'_{s2} from their true values were 1% – 14%, 3% – 15%, and 5% – 20%, respectively. Therefore, the least accurately retrieved parameter was μ'_{s2} , where in four of the twelve phantoms we observed absolute % deviations within 15% – 20% (Nos. 4, 7, 8 and 9) from the true values. The complete summary of the phantom experiments is reported in Table C1 in Appendix C, where we also include retrieved values using a semi-infinite homogenous model for comparison.

Considering the measurement uncertainties in the true values (~6%) and in the retrieved values (as shown by the error bars in figure. 6.7), as well as mixture calibration errors during the liquid phantom preparation (not quantified), the two-layered approach employed here was able to retrieve all parameters with good accuracy. We present the absolute % deviation in the measured parameters averaged across 12 phantoms in figure 6.8, where the error bars represent standard errors of the % deviations.

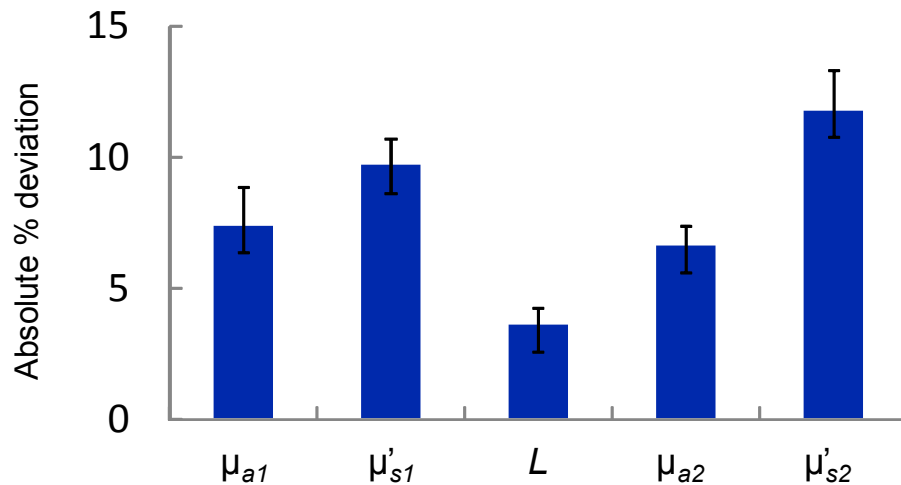


Figure 6.8. Average of the absolute % errors in the measured parameters with respect to true values across twelve two-layered phantoms. The error bars represent standard errors.

We underscore the fact that clinically most relevant parameters, L and μ_{a2} , which are representative of scalp-cortex distance and cerebral absorption coefficient, respectively, were recovered with high accuracy (absolute % error $< 7\%$).

6.2.4. Discussion of the Results

Monte Carlo methods offer a flexible and accurate approach toward simulating photon transport in turbid media. In this work, MC simulations allowed us to verify the validity of our implementation of the analytical solution of the DE for two-layered media. The optical coefficients and top layer thickness in all MC sets were recovered with good accuracy, with deviations in the order of a few percent in most cases, which are typical uncertainties found also in other studies (Kienle *et al.* 1998; Alexandrakis *et al.* 2001). To test the performance of our inversion routine, we have also carried out separate measurements on synthetic data generated using our forward model with additive noise (typically 1% random noise). We found accurate recovery of the true values in these data sets, with deviations never exceeding a few percent and always smaller (as it is expected) than those found in the MC data (data not shown).

The two-layered phantom experiments presented here were of key importance in the validation of our approach, which featured an unconstrained inversion procedure of six unknown parameters with no prior knowledge. Previous experiments on two-layered phantoms, featuring two-layered models have been reported for the representation of extracerebral tissue overlaying cerebral tissue (Pucci *et al.* 2010) (top layer thickness typically more than ~ 10) and skin tissue overlaying fat/muscle tissue (Pham *et al.* 2000; Alexandrakis *et al.* 2001; Ripoll *et al.* 2001; Martelli *et al.* 2004; Li *et al.* 2007) (top layer

thickness typically less than ~ 6 mm). In just two of these studies optical coefficients of the two layers and the top layer thicknesses were measured simultaneously (Alexandrakis *et al.* 2001; Martelli *et al.* 2004). In the frequency domain, Alexandrakis *et al.* used a simplex search algorithm and recovered the second layer optical coefficients with good accuracy (absolute % deviations $\sim 10\%$) in almost all phantoms (Alexandrakis *et al.* 2001). However their measurement accuracy was lower for the first layer parameters. In the time domain, Martelli *et al.* used a Levenberg-Marquardt routine and reported excellent recovery of the first layer optical coefficients and second layer absorption coefficient (with absolute % deviations of less than 5%) (Martelli *et al.* 2004). For the first layer thickness and the second layer scattering coefficients their accuracy was lower (absolute % deviations of 11% and 33%, respectively). In the current study, using a frequency domain acquisition system and a Levenberg-Marquardt inversion routine we were able to measure all parameters with relatively high accuracy (with absolute % deviations of less than 12% for all parameters) (as seen in figure 6). To our knowledge, such high accuracy measurements on two-layered phantoms in the frequency domain are unprecedented. Furthermore, the experimental tests (where the reference true values were obtained with diffusion theory in an infinite geometry and with source-detector separations > 20 mm, thus under conditions well within the limits of applicability of diffusion theory) indicate the accuracy of our proposed diffusion-based method for the optical characterization of two-layered media.

6.3. Demonstration in Human Volunteers

6.3.1. Methods

Three participants were recruited to demonstrate the methods applicability in human subjects (all males, mean \pm standard deviation age of 29 ± 2 years). The protocol for the human subject measurements was approved by the Tufts University Institutional Review Board and written informed consent was obtained from all subjects prior to the measurements. We used an approach based on a preliminary calibration of the optical probe on a known phantom as described in (Hallacoglu *et al.* 2012). The optical probe was made of polyurethane silicon and featured two detector optical fiber bundles (3 mm in core diameter) separated by 11 mm, and seven pairs of illumination optical fibers (0.4 mm in core diameter) that guided light at 690 and 830 nm, located at distances in the range 8–49 mm from the detector fiber bundles. Figure 6.9 illustrates the probe layout and placement on the subject's forehead. As illustrated in figure 6.9, source fibers were located 8 to 38 mm from the first detector bundle and 19 to 49 mm from the second detector bundle in 5 mm increments. The optical probe was placed on the left side of the subjects' forehead and held in place using a commercial sports band to exert light pressure for comfort, while guaranteeing good contact between the optical fibers and the subject's scalp.

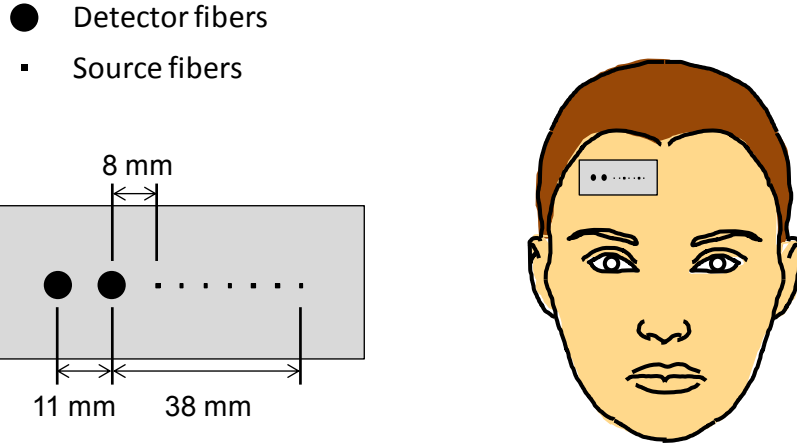


Figure 6.9. Schematic diagram of the experimental setup for the human subject measurements. A) The polystyrene optical probe used in the *in vivo* measurements, and (B) its positioning on the subject's forehead during measurements. Larger and smaller circles in (A) denote detector and source fibers positions, respectively.

For the analysis, recordings from the two detector bundles were combined, providing an effective source-detector range of 8 to 49 mm. Here, the range considered for the analysis was 13–48 mm to comply with the diffusion conditions. Under the assumption that oxy-hemoglobin (HbO_2), deoxy-hemoglobin (Hb) and water are the major absorbers in the probed tissue volume at the two wavelengths considered, we calculated tissue concentrations of HbO_2 and Hb in each layer using the expressions introduced in Chapter 5, Section 5.3 for two-layers:

$$[\text{HbO}_2]_i = \frac{\mu_{ai}^{690\text{nm}} \cdot \epsilon_{\text{Hb}}^{830\text{nm}} - \mu_{ai}^{830\text{nm}} \cdot \epsilon_{\text{Hb}}^{690\text{nm}}}{\epsilon_{\text{HbO}_2}^{690\text{nm}} \epsilon_{\text{Hb}}^{830\text{nm}} - \epsilon_{\text{HbO}_2}^{830\text{nm}} \epsilon_{\text{Hb}}^{690\text{nm}}} - \frac{\mu_{a(\text{H}_2\text{O})}^{690\text{nm}} \cdot \epsilon_{\text{Hb}}^{830\text{nm}} - \mu_{a(\text{H}_2\text{O})}^{830\text{nm}} \cdot \epsilon_{\text{Hb}}^{690\text{nm}}}{\epsilon_{\text{HbO}_2}^{690\text{nm}} \epsilon_{\text{Hb}}^{830\text{nm}} - \epsilon_{\text{HbO}_2}^{830\text{nm}} \epsilon_{\text{Hb}}^{690\text{nm}}} C_{\text{H}_2\text{O}-vf} \quad (6.1)$$

$$[\text{Hb}]_i = \frac{\mu_{ai}^{830\text{nm}} \cdot \epsilon_{\text{HbO}_2}^{690\text{nm}} - \mu_{ai}^{690\text{nm}} \cdot \epsilon_{\text{HbO}_2}^{830\text{nm}}}{\epsilon_{\text{HbO}_2}^{690\text{nm}} \epsilon_{\text{Hb}}^{830\text{nm}} - \epsilon_{\text{HbO}_2}^{830\text{nm}} \epsilon_{\text{Hb}}^{690\text{nm}}} + \frac{\mu_{a(\text{H}_2\text{O})}^{690\text{nm}} \cdot \epsilon_{\text{HbO}_2}^{830\text{nm}} - \mu_{a(\text{H}_2\text{O})}^{830\text{nm}} \cdot \epsilon_{\text{HbO}_2}^{690\text{nm}}}{\epsilon_{\text{HbO}_2}^{690\text{nm}} \epsilon_{\text{Hb}}^{830\text{nm}} - \epsilon_{\text{HbO}_2}^{830\text{nm}} \epsilon_{\text{Hb}}^{690\text{nm}}} C_{\text{H}_2\text{O}-vf} \quad (6.2)$$

where $i = 1, 2$ (i.e. extracerebral and cerebral tissue, respectively). We assumed a value of 0.7 (i.e. 70% water content) for $C_{\text{H}_2\text{O-vf}}$ (Ohmae *et al.* 2006; Gagnon *et al.* 2008; Hallacoglu *et al.* 2012) Finally, we calculated the total hemoglobin concentration and hemoglobin saturation in each layer using:

$$[\text{HbT}]_i = [\text{HbO}_2]_i + [\text{Hb}]_i \quad (6.3)$$

$$\text{StO}_2|_i = [\text{HbO}_2]_i / [\text{HbT}]_i. \quad (6.4)$$

6.3.2. Results

We report retrieved values for μ_{a1} , μ'_{s1} , L , μ_{a2} , μ'_{s2} for wavelengths 690 nm and 830 nm and corresponding hemoglobin values on three subjects in figure 6.10. Panels at the far left represent absolute absorption (panel A) and reduced scattering coefficients (panel D) measured in all three subjects at the corresponding wavelengths (i.e. 690 and 830 nm). Panels in the middle represent the same data plotted against the layers (i.e. Layer 1 and Layer 2) for visualization purposes. Corresponding total hemoglobin concentration and oxygen saturation are reported in panel C. Finally, first layer thicknesses measured at both wavelengths are reported in panel F.

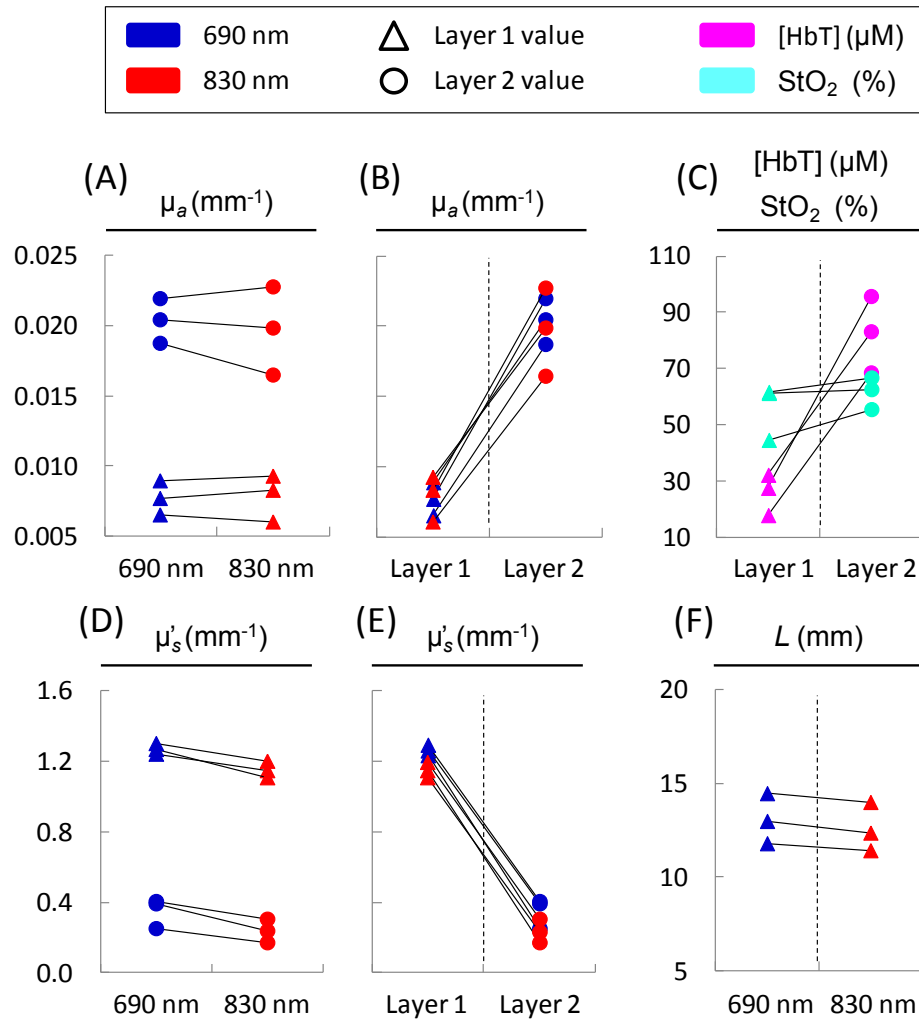


Figure 6.10. Retrieved results on the forehead of three human subjects using two-layered analysis. (A) Absorption coefficient measured with wavelength 690 nm and 830 nm; (B) Absorption coefficient in layers 1 and 2; (C) Total hemoglobin concentration and oxygen saturation in layers 1 and 2; (D) Reduced scattering coefficient measured with wavelength 690 nm and 830 nm; (E) Reduced scattering coefficient in layers 1 and 2; (F) First layer thickness measured with wavelength 690 nm and 830 nm.

In Table 6.2, I report the optical coefficients and the first layer thickness measured using the two-layered analysis. For a comparison with Table 6.2, in Table 6.3, I report optical coefficients that were retrieved using a semi-infinite homogenous model. In Tables 6.4 and 6.5, I report corresponding hemoglobin values for both the two methods.

Table 6.2. Retrieved optical coefficients and first layer thickness on the forehead of three human subjects.

Subject	μ_{a1} (mm ⁻¹)		μ'_{s1} (mm ⁻¹)		L (mm)		μ_{a2} (mm ⁻¹)		μ'_{s2} (mm ⁻¹)	
	690 nm	830 nm	690 nm	830 nm	690 nm	830 nm	690 nm	830 nm	690 nm	830 nm
1	0.007	0.006	1.2	1.1	11.8	11.4	0.019	0.016	0.2	0.2
2	0.009	0.009	1.3	1.2	13.0	12.3	0.020	0.020	0.4	0.3
3	0.008	0.008	1.3	1.1	14.5	14.0	0.022	0.023	0.4	0.2
<i>mean</i>	<i>0.008</i>	<i>0.008</i>	<i>1.3</i>	<i>1.1</i>	<i>13.1</i>	<i>12.6</i>	<i>0.020</i>	<i>0.020</i>	<i>0.3</i>	<i>0.2</i>
<i>stdev</i>	<i>0.001</i>	<i>0.002</i>	<i>0.0</i>	<i>0.0</i>	<i>1.3</i>	<i>1.3</i>	<i>0.002</i>	<i>0.003</i>	<i>0.1</i>	<i>0.1</i>

Table 6.3. Retrieved optical coefficients on the forehead of three human subjects using a homogenous model as a comparison with Table 3. Group mean and standard deviations (stdev) are reported in the bottom two rows.

Subject	μ_a (mm ⁻¹)		μ'_s (mm ⁻¹)	
	690 nm	830 nm	690 nm	830 nm
1	0.013	0.012	0.4	0.3
2	0.011	0.013	1.0	0.7
3	0.010	0.012	0.8	0.6
<i>mean</i>	<i>0.011</i>	<i>0.012</i>	<i>0.7</i>	<i>0.5</i>
<i>stdev</i>	<i>0.001</i>	<i>0.000</i>	<i>0.3</i>	<i>0.2</i>

Table 6.4. Retrieved concentrations of oxy-hemoglobin ([HbO₂]) and deoxy-hemoglobin ([Hb]) on the forehead of three human subjects using two-layered (indicated by ‘Superficial’ and ‘Cerebral’) and homogeneous models. Group mean and standard deviations (stdev) are reported in the bottom two rows.

Subject	[HbO ₂] (uM)			[Hb] (uM)		
	Superficial	Cerebral	Homogeneous	Superficial	Cerebral	Homogeneous
1	8.0	38.0	25.6	9.9	30.3	21.1
2	19.8	51.8	33.8	12.4	31.2	14.3
3	17.1	63.7	31.8	10.5	31.9	14.5
<i>mean</i>	<i>15.0</i>	<i>51.2</i>	<i>30.4</i>	<i>10.9</i>	<i>31.1</i>	<i>16.6</i>
<i>stdev</i>	<i>6.2</i>	<i>12.9</i>	<i>4.3</i>	<i>1.3</i>	<i>0.8</i>	<i>3.9</i>

A first striking result is the reproducibility of L , which was measured independently using the two wavelengths (table 6.2). The measured range for this parameter across all subjects (11.4 – 14.5 mm) are within anatomical values reported in the literature for the adult human forehead (~12 – 16 mm) (Haeussinger *et al.* 2011). Other common characteristics across subjects include significantly higher μ_{a2} values with respect to μ_{a1} (Table 6.2), which corresponds to higher total hemoglobin concentrations in the cerebral tissues ($82 \pm 14 \mu\text{M}$) in comparison to superficial tissues ($26 \pm 7 \mu\text{M}$). We also found slightly higher hemoglobin saturation in cerebral tissues ($62\% \pm 10\%$) in comparison to superficial tissues ($56\% \pm 6\%$); however this difference was not significant (Table 6.5).

Table 6.5. Retrieved total hemoglobin concentration ([HbT]) and hemoglobin oxygen saturation (StO₂) on the forehead of three human subjects using two-layered (indicated by ‘Superficial’ and ‘Cerebral’) and homogeneous models. Group mean and standard deviations (stdev) are reported in the bottom two rows.

Subject	[HbT] (μM)			StO ₂ (%)		
	Superficial	Cerebral	Homogeneous	Superficial	Cerebral	Homogeneous
1	17.9	68.3	46.7	44.8	55.6	54.7
2	32.2	83.0	48.1	61.5	62.4	69.2
3	27.6	95.6	46.3	61.9	66.6	68.7
<i>mean</i>	25.9	82.3	47.0	56.0	61.6	64.2
<i>stdev</i>	7.3	13.6	0.9	9.8	5.6	8.2

6.3.3. Discussion of the Results

Although we have not performed independent validation measurements (for example an MRI measurement of scalp-cortex distance), two arguments can be made in support of the reliability of the results of our method. The first argument is that the reduced

scattering coefficient measured at 690 nm was larger than that at 830 nm for both layers and for all subjects, following the expected wavelength dependence relationship (Fantini and Sassaroli 2012). The second argument is the consistency of independently measured scalp-cortex distance at the two wavelengths used in all subjects (Table 6.2) and that all measured values are within anatomical ranges (Haeussinger *et al.* 2011). We emphasize the importance of such results given that the inversion procedure implemented by us was unconstrained, allowing the measured parameters to take any possible value during the inversion procedure. This point is demonstrated in figure 6.6, where the first layer μ_a (μ_{a1}) varies from as high as 0.045 mm^{-1} (around 20th iteration) to as low as $\sim -0.005 \text{ mm}^{-1}$ (around 50th iteration) in the course of the inversion procedure prior to converging to the correct value.

Concentration and saturation of hemoglobin measurements in all three subjects were within previously reported values in animal (Fantini *et al.* 1999; Hallacoglu *et al.* 2011) and human (Franceschini *et al.* 2007; Gagnon *et al.* 2008; Hallacoglu *et al.* 2012) brain. The first and the second layer measurement of some of these parameters (Table 6.3) were significantly different. Such differences have also been observed by other researchers (Choi *et al.* 2004; Gagnon *et al.* 2008). The advantage of our approach over these earlier studies was the derivation of the hemoglobin parameters and the scalp-cortex distances without any *a priori* knowledge (these studies used MRI to measure the scalp-cortex distance). Interestingly, the total hemoglobin concentration measured in young subjects using the homogenous model in Chapter 5, Section 3 (mean \pm standard deviation: $52 \pm 13 \text{ }\mu\text{M}$) compares well with the values here (mean \pm standard deviation: $47 \pm 1 \text{ }\mu\text{M}$) when a homogenous model is used (Table 6.5). Moreover, these values are in

between the first ($30 \pm 7 \mu\text{M}$) and the second layer ($82 \pm 13 \mu\text{M}$) values measured in this study (Table 6.5). This is an indication that homogenous assumption was influenced by the extracerebral tissue physiology. Cerebral saturation in the earlier study (mean \pm standard deviation: $58\% \pm 13\%$) (Hallacoglu *et al.* 2012) compares well with both the first ($56\% \pm 10\%$) and the second ($62\% \pm 6\%$) layer values reported here.

Intersubject variability in baseline human head hemoglobin concentrations has been reported in several studies including those that used homogenous (Comelli *et al.* 2007; Hallacoglu *et al.* 2012) or two layered (Choi *et al.* 2004; Gagnon *et al.* 2008) models. Although we have studied only a small group of subjects, in this study we have observed a similar intersubject variability in the baseline concentrations of hemoglobin, both in the extracerebral and cerebral tissue layers (Table 6.2). These results emphasize the fact that individualized characterization of the baseline optical coefficients of the human head is important and should be a part of routine practice in NIRS and fNIRS studies.

We point out that second layer reduced scattering coefficients measured in the subjects ($0.3 \pm 0.1 \text{ mm}^{-1}$ and $0.2 \pm 0.1 \text{ mm}^{-1}$ at 690 nm and 830 nm, respectively) appear to be low, even though this result is consistent with some reported values in the literature (such as 0.3 mm^{-1} and 0.5 mm^{-1} as reported in Gagnon *et al.*, (Fig. 3A) (Gagnon *et al.* 2008)). Low μ'_{s2} values such as these may have a physiological origin in that they may be representative of contributions from the clear cerebrospinal fluid (CSF) (featuring low scattering) to the layer 2 measurements. In this case, absorption coefficient in layer 2 (μ_{a2}) would also be underestimated due to the CSF ($\mu_{a(\text{CSF})} < 0.005 \text{ mm}^{-1}$), which would further enhance the differences in hemoglobin concentrations between the two layers.

Another possibility is that this parameter may have a low level of information content inherent to the two-layered diffuse reflectance measurements, which is an interpretation also shared by a similar study in the time domain (Martelli *et al.* 2004). In fact, μ'_{s2} was the parameter that we were least sensitive to in our phantom experiments as seen in the absolute % deviation plot (figure 6.8).

In this Chapter, I presented a multi-distance frequency-domain NIRS approach that relies on a two-layered solution of the diffusion equation and an accompanying six-parameter inversion routine to simultaneously measure the absolute optical coefficients of two-layered turbid media. When applied to non-invasive NIRS measurements on the human head, the approach yields the concentration and oxygen saturation of hemoglobin in the extracerebral (layer 1) and cerebral (layer 2) tissue layers, as well as the scalp-cortex distance. This is the first frequency-domain study that presents high accuracy measurement of these parameters simultaneously using standalone NIRS. I have reported results of Monte Carlo (MC) simulations and two-layered phantom measurements. I have also reported measurements in human subjects to explore the *in vivo* applicability of our approach and found physiologically reasonable values for all measured parameters.

References for Chapter 6

- Alexandrakis, G., D. R. Busch, G. W. Faris and M. S. Patterson (2001). "Determination of the optical properties of two-layer turbid media by use of a frequency-domain hybrid monte carlo diffusion model." *Appl Opt* **40**(22): 3810-3821.
- Bevilacqua, F., D. Piguet, P. Marquet, J. D. Gross, B. J. Tromberg and C. Depeursinge (1999). "In vivo local determination of tissue optical properties: applications to human brain." *Appl Opt* **38**(22): 4939-4950.
- Choi, J., M. Wolf, V. Toronov, U. Wolf, C. Polzonetti, D. Hueber, L. P. Safonova, R. Gupta, A. Michalos, W. Mantulin and E. Gratton (2004). "Noninvasive determination of the optical properties of adult brain: near-infrared spectroscopy approach." *J Biomed Opt* **9**(1): 221-229.
- Comelli, D., A. Bassi, A. Pifferi, P. Taroni, A. Torricelli, R. Cubeddu, F. Martelli and G. Zaccanti (2007). "In vivo time-resolved reflectance spectroscopy of the human forehead." *Appl Opt* **46**(10): 1717-1725.
- Del Bianco, S., F. Martelli, F. Cignini, G. Zaccanti, A. Pifferi, A. Torricelli, A. Bassi, P. Taroni and R. Cubeddu (2004). "Liquid phantom for investigating light propagation through layered diffusive media." *Opt Express* **12**(10): 2102-2111.
- Di Ninni, P., Y. Berube-Lauziere, L. Mercatelli, E. Sani and F. Martelli (2012). "Fat emulsions as diffusive reference standards for tissue simulating phantoms?" *Appl Opt* **51**(30): 7176-7182.
- Di Ninni, P., F. Martelli and G. Zaccanti (2011). "Intralipid: towards a diffusive reference standard for optical tissue phantoms." *Phys Med Biol* **56**(2): N21-28.
- Fantini, S., M. A. Franceschini and E. Gratton (1994). "Semi-infinite-geometry boundary problem for light migration in highly scattering media: a frequency-domain study in the diffusion approximation." *J. Opt. Soc. Am. B* **11**(10): 2128-2138.
- Fantini, S., D. Hueber, M. A. Franceschini, E. Gratton, W. Rosenfeld, P. G. Stubblefield, D. Maulik and M. R. Stankovic (1999). "Non-invasive optical monitoring of the newborn piglet brain using continuous-wave and frequency-domain spectroscopy." *Phys Med Biol* **44**(6): 1543-1563.
- Fantini, S. and A. Sassaroli (2012). "Near-infrared optical mammography for breast cancer detection with intrinsic contrast." *Ann Biomed Eng* **40**(2): 398-407.
- Flock, S. T., S. L. Jacques, B. C. Wilson, W. M. Star and M. J. van Gemert (1992). "Optical properties of Intralipid: a phantom medium for light propagation studies." *Lasers Surg Med* **12**(5): 510-519.
- Franceschini, M. A., S. Thaker, G. Themelis, K. K. Krishnamoorthy, H. Bortfeld, S. G. Diamond, D. A. Boas, K. Arvin and P. E. Grant (2007). "Assessment of infant brain development with frequency-domain near-infrared spectroscopy." *Pediatr Res* **61**(5 Pt 1): 546-551.
- Gagnon, L., C. Gauthier, R. D. Hoge, F. Lesage, J. Selb and D. A. Boas (2008). "Double-layer estimation of intra- and extracerebral hemoglobin concentration with a time-resolved system." *J Biomed Opt* **13**(5): 054019.
- Haeussinger, F. B., S. Heinzl, T. Hahn, M. Schecklmann, A. C. Ehlis and A. J. Fallgatter (2011). "Simulation of near-infrared light absorption considering individual head

- and prefrontal cortex anatomy: implications for optical neuroimaging." PLoS ONE **6**(10): e26377.
- Hale, G. M. and M. R. Querry (1973). "Optical Constants of Water in the 200-nm to 200-microm Wavelength Region." Appl Opt **12**(3): 555-563.
- Hallacoglu, B., A. Sassaroli, S. Fantini and A. M. Troen (2011). "Cerebral perfusion and oxygenation are impaired by folate deficiency in rat: absolute measurements with noninvasive near-infrared spectroscopy." J Cereb Blood Flow Metab **31**(6): 1482-1492.
- Hallacoglu, B., A. Sassaroli, M. Wysocki, E. Guerrero-Berroa, M. Schnaider Beeri, V. Haroutunian, M. Shaul, I. H. Rosenberg, A. M. Troen and S. Fantini (2012). "Absolute measurement of cerebral optical coefficients, hemoglobin concentration and oxygen saturation in old and young adults with near-infrared spectroscopy." J Biomed Opt **17**(8): 081406-081401.
- Hallacoglu, B., A. Sassaroli, M. Wysocki, E. Guerrero-Berroa, M. Schnaider Beeri, V. Haroutunian, M. Shaul, I. H. Rosenberg, A. M. Troen and S. Fantini (2012). "Absolute measurement of cerebral optical coefficients, hemoglobin concentration and oxygen saturation in old and young adults with near-infrared spectroscopy." J Biomed Opt **17**(8): 81406-81401.
- Kienle, A., M. S. Patterson, N. Dognitz, R. Bays, G. Wagninures and H. van den Bergh (1998). "Noninvasive determination of the optical properties of two-layered turbid media." Appl Opt **37**(4): 779-791.
- Li, A., R. Kwong, A. Cerussi, S. Merritt, C. Hayakawa and B. Tromberg (2007). "Method for recovering quantitative broadband diffuse optical spectra from layered media." Appl Opt **46**(21): 4828-4833.
- Martelli, F., S. Del Bianco, G. Zaccanti, A. Pifferi, A. Torricelli, A. Bassi, P. Taroni and R. Cubeddu (2004). "Phantom validation and in vivo application of an inversion procedure for retrieving the optical properties of diffusive layered media from time-resolved reflectance measurements." Opt Lett **29**(17): 2037-2039.
- Martelli, F. and G. Zaccanti (2007). "Calibration of scattering and absorption properties of a liquid diffusive medium at NIR wavelengths. CW method." Opt Express **15**(2): 486-500.
- Ohmae, E., Y. Ouchi, M. Oda, T. Suzuki, S. Nobesawa, T. Kanno, E. Yoshikawa, M. Futatsubashi, Y. Ueda, H. Okada and Y. Yamashita (2006). "Cerebral hemodynamics evaluation by near-infrared time-resolved spectroscopy: correlation with simultaneous positron emission tomography measurements." Neuroimage **29**(3): 697-705.
- Pham, T. H., T. Spott, L. O. Svaasand and B. J. Tromberg (2000). "Quantifying the properties of two-layer turbid media with frequency-domain diffuse reflectance." Appl Opt **39**(25): 4733-4745.
- Pucci, O., V. Toronov and K. St Lawrence (2010). "Measurement of the optical properties of a two-layer model of the human head using broadband near-infrared spectroscopy." Appl Opt **49**(32): 6324-6332.
- Ripoll, J., V. Ntziachristos, J. P. Culver, D. N. Pattanayak, A. G. Yodh and M. Nieto-Vesperinas (2001). "Recovery of optical parameters in multiple-layered diffusive media: theory and experiments." J Opt Soc Am A Opt Image Sci Vis **18**(4): 821-830.

- Spinelli, L., F. Martelli, A. Farina, A. Pifferi, A. Torricelli, R. Cubeddu and G. Zaccanti (2007). "Calibration of scattering and absorption properties of a liquid diffusive medium at NIR wavelengths. Time-resolved method." Opt Express **15**(11): 6589-6604.
- van Staveren, H. J., C. J. Moes, J. van Marie, S. A. Prahl and M. J. van Gemert (1991). "Light scattering in Intralipid-10% in the wavelength range of 400-1100 nm." Appl Opt **30**(31): 4507-4514.

Chapter 7

Summary and Future Directions

In its core, this work and the thesis thereof were about one longstanding project that has evolved to maturity through both theoretical development and numerous independent yet cohesive experimental approaches. In the framework of this project, these two aspects (that is, theory and practice) have been closely connected and required concurrent evolution. The study on the rabbit model of testicular ischemia (Chapter 5, Section 5.1) was the first *in vivo* study featuring small tissue volumes (as small as $\sim 500 \text{ mm}^3$ with dimensions $30 \times 15 \times 11 \text{ mm}$) that we worked on. The significance of this study in the framework of this thesis was that it was paramount for the development of theoretical methods and practical validation.

For the theoretical aspect, the study presented us with the opportunity to test the homogenous solution of the diffusion equation and semi-infinite boundary conditions in small tissue volumes. The optical properties under semi-infinite geometry assumption can be recovered in two different ways as we have introduced in Chapter 2 and discussed further in Appendix A. As a reminder, these are through approximations [Eqs. (2.9) – (2.14) in Chapter 2] that are valid under certain conditions, or by employing nonlinear fitting procedures. I have shown in the simulation study reported in Appendix A that the approximations underestimate the true optical properties at short source detector

separations. When the same analysis was performed in the rabbit study, we found similar trends, for instance, results for a representative case (Rabbit 1, Left/Baseline) were as follows:

$$\begin{aligned} \mu_{a\text{-Fit}} &= 0.016 \text{ mm}^{-1}, & \mu'_{s\text{-Fit}} &= 0.56 \text{ mm}^{-1}, \\ \mu_{a\text{-Apx}} &= 0.014 \text{ mm}^{-1}, & \mu'_{s\text{-Apx}} &= 0.42 \text{ mm}^{-1}, \end{aligned}$$

where “Fit” and “Apx” represent results through nonlinear fitting and approximations, respectively. Since the intrinsic optical properties of the testicular tissue are not known, the appropriate theoretical approach for optical characterization of small tissue volumes (nonlinear fitting procedure) was established in this way.

For the practical aspect, the protocol in the study was very suitable to test our acquisition system in small tissue volumes. The blood perfusion in the testicular tissue was either unrestricted or restricted (dictated by the torsion). Experimental variables such as anesthesia or physiological features (*i.e.* respiration rate, heart rate etc.), which could play a role in investigating the brain, did not play a role in the alterations of the tissue perfusion. In addition, the torsion surgery induced a uniform reduction in blood perfusion and oxygenation in the testicular tissue. These, in turn, allowed us to test the sensitivity of our approach (*i.e.* to changes in the concentrations of hemoglobin chromophores) in a protocol with a well-characterized physiological outcome.

The methods that were developed in the rabbit study allowed us to move on to the investigation of the rat brain. From the perspective of theoretical modeling, the study in the rat brain (Chapter 5, Section 5.2) featured the analysis strategies that were developed in the rabbit study. Small scalp-to-cortex distance in the rat head (~1 mm) allowed us to

reasonably assume optical homogeneity of the probed tissue volume. For this study, we developed a novel, fully automated rat brain oximetry system (figure 7.4) for performing absolute measurement of optical properties during baseline/resting conditions and respiration challenges. One of the most important observations we have made in this study was that absolute baseline values were far more informative than the relative changes induced by respiration challenges. Absolute values enabled physiologically meaningful comparisons of long-term changes in cerebrovascular function, both within and among rats, and improved relative measurements by allowing corrections/normalizations based on specific baseline values for each rat. The fact that absolute measures revealed significant differences between control and treatment groups, whereas relative measures did not, demonstrated the richer information content that absolute NIRS measures could provide for the evaluation of cerebrovascular health.

The study in the elderly and young people (Chapter 5, Section 5.3) was a first attempt to perform such measurements in human. The results were among the few reported absolute optical measurements to have been made noninvasively in the human brain. We demonstrated that multi-distance measurements and a homogeneous, semi-infinite model provide fast, reliable and robust information in the human head. However, our sensitivity analysis revealed a dependence of the optical coefficients to source-detector separation, which implied a dependence of the tissue composition to tissue depth, consistent with the layered anatomy of the head (*i.e.* scalp, skull, dura mater, subarachnoid space overlaying the brain). These results motivated the successive studies using two-layered approaches to explore the potential of achieving depth discrimination in absolute NIRS measurements, as presented in Chapter 6.

In Chapter 6, we attempted to address the effect of superficial, extracerebral tissue layers to noninvasive optical measurements of the human brain. Our results in human subjects using homogenous analysis (both in Chapters 5 and 6) demonstrated that achieving depth discrimination is highly relevant and significant in absolute brain oximetry. To the best of our knowledge, this is the first time that such concurrent measurements of hemoglobin concentration in extracerebral and cerebral tissues combined with a measure of cerebral cortex depth using standalone NIRS have been presented. This represents a significant advance toward the application of NIRS to monitor long-term changes in cerebrovascular health both by stand-alone cerebral oximetry and by correcting relative measures of hemodynamic changes in functional studies.

Looking forward, further studies on a larger number of subjects would be required to gain confidence in the reproducibility of the absolute values in the human head. Other potential *in vivo* experiments include studies on large animal models (*i.e.* pig or sheep) featuring measurements under controlled physiological challenges, which would allow for a direct validation of our approach *in vivo*. Moreover, utilizing numerical forward models for a realistic human head geometry would be highly relevant (for instance, using NIRFAST software) (Dehghani *et al.* 2008) to test the performance of our approach in more realistic geometries.

References for Chapter 7

Dehghani, H., M. E. Eames, P. K. Yalavarthy, S. C. Davis, S. Srinivasan, C. M. Carpenter, B. W. Pogue and K. D. Paulsen (2008). "Near infrared optical tomography using NIRFAST: Algorithm for numerical model and image reconstruction." Commun Numer Methods Eng **25**(6): 711-732.

Appendix A

As I have reported in Chapter 2, Section 2.2.2, the linear approximations given for semi-infinite geometry hold only if the condition $r \mu_{\text{eff}} \gg 1$ is satisfied. Here, I present a comparison between the linear approximations and a nonlinear inversion procedure (based on the Levenberg-Marquard method) in the evaluation of optical properties of a homogeneous semi-infinite medium. The data were generated using Monte Carlo simulations. I report the percent errors between the true and the retrieved optical properties for seven media, where the red symbols represent the errors using the linear approximations and the blue symbols represent the errors using the nonlinear inversion procedure. Here, absorption coefficient (μ_a) is varied between $0.002 - 0.03 \text{ mm}^{-1}$ and reduced scattering coefficient (μ'_s) is set to 1 mm^{-1} . For the analysis, three examples are considered, featuring different ranges of source-detector separations (r).

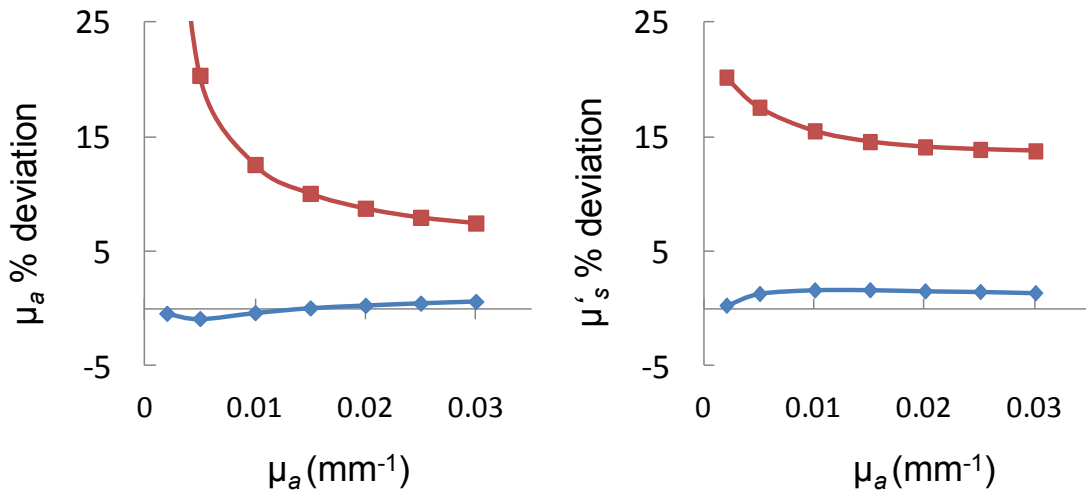


Figure A1. Analysis range: 6 – 35 mm. Reduced scattering coefficient = 1 mm^{-1} . Red – Linear Approximation; Blue – Nonlinear Inversion Procedure

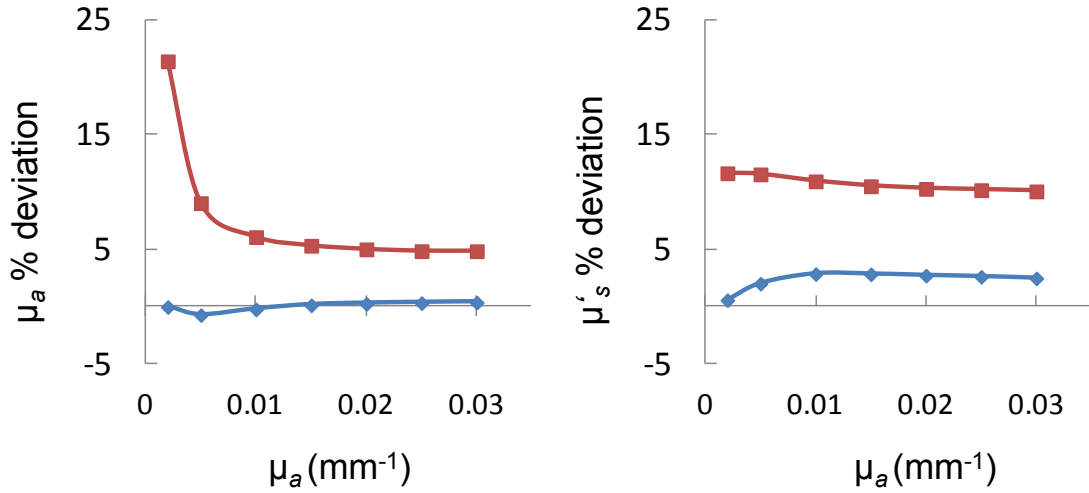


Figure A2. Analysis range: 10 – 35 mm. Reduced scattering coefficient = 1 mm^{-1} . Red – Linear Approximation; Blue – Nonlinear Inversion Procedure

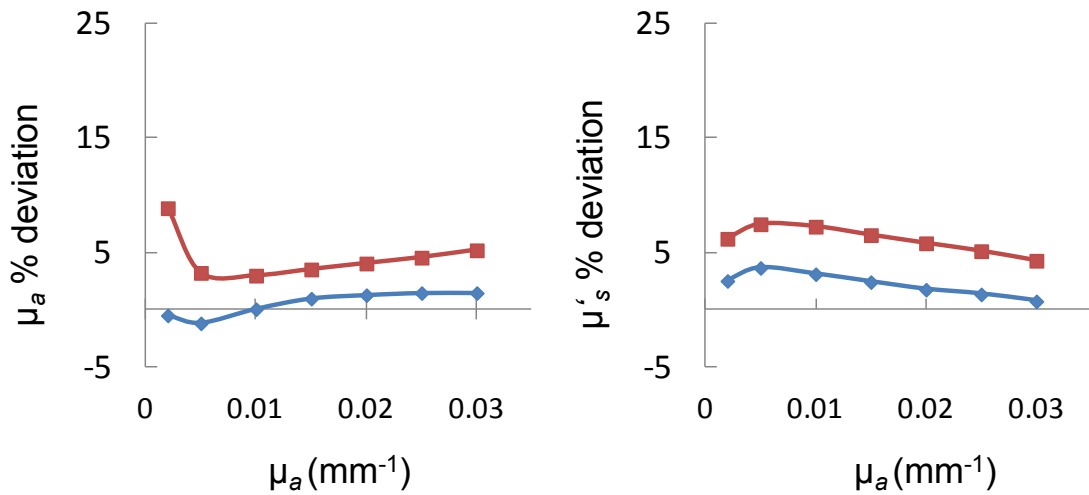


Figure A1. Analysis range: 20 – 35 mm. Reduced scattering coefficient = 1 mm^{-1} . Red – Linear Approximation; Blue – Nonlinear Inversion Procedure

As it is clearly demonstrated in these three examples, the linear approximations perform well once the required condition (*i.e.* $r \mu_{\text{eff}} \gg 1$) is met. Here, the reduced scattering coefficient is fixed at 1 mm^{-1} for all of the simulations, therefore the only two

parameters that influence the % deviation values are the source-detector separation and the absorption coefficient. Between the two parameters, it is clear that the effect of source-detector separation dominates.

Appendix B

We performed measurements on a tissue-like phantom to validate the applicability of our diffusion based model to short source-detector distances. A silicon resin phantom (manufactured by ISS Inc, Champaign, IL) with absorption and reduced scattering coefficients of $\mu_a^{690\text{nm}} \sim 0.18 \text{ cm}^{-1}$, $\mu_a^{830\text{nm}} \sim 0.16 \text{ cm}^{-1}$, $\mu_s^{690\text{nm}} \sim 4.6 \text{ cm}^{-1}$ and $\mu_s^{830\text{nm}} \sim 4.4 \text{ cm}^{-1}$ was utilized for these measurements. With the same scanning protocols used in the rabbit and rat studies, AC and phase data were collected on the phantom at source-detector separations ranging from 6 to 15 mm. Using the known optical properties of the phantom, we evaluated theoretical AC and phase values on the basis of diffusion theory, and we computed residuals between experimental and theoretical values. Figures B1 (a) and B1 (b) report experimental (solid lines) and theoretical (dotted lines) traces of phase and AC data, respectively, at the same wavelengths used in the rat study (690 and 830 nm) for source-detector distances of 6-15 mm. Figures B1 (c) and B1 (d) report the quantitative deviation (residuals) of experimental values from diffusion theory. Rectangular regions indicate the range of source-detector distances considered in the analysis of data from the rat study (Section 5.2). Figure B1 shows that a discrepancy between experimental and diffusion-based traces exists at short source detector separations (< 8 mm), however this difference becomes negligible beyond 8 mm. It is important to point out that the region of applicability of diffusion theory likely extends to even shorter source-detector distances in the rat brain, whose reduced scattering

coefficient ($\mu'_s \sim 10 \text{ cm}^{-1}$) is almost twice as much as that of the phantom used in this experiment.

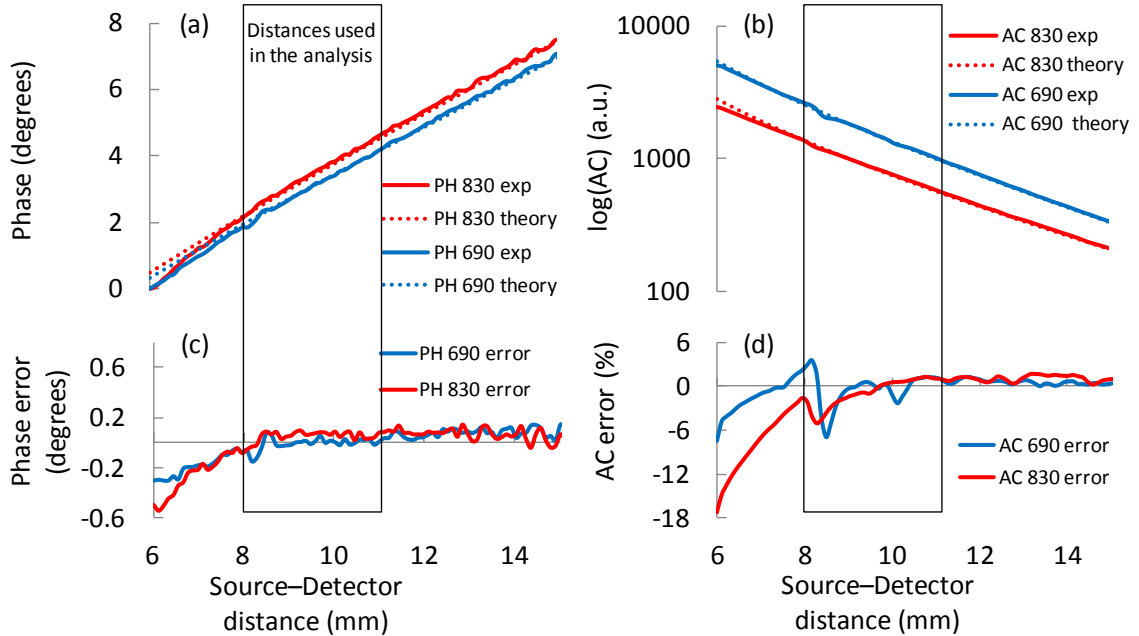


Figure B1 – Validation of our diffusion-based model on a tissue-like phantom at short source-detector distances. Panels (a) and (b) illustrate experimental phase (PH) and amplitude (AC) values, respectively, measured at 690 and 830 nm (solid lines) versus diffusion theory approximation (dotted lines). Panels (c) and (d) illustrate quantitative errors between measurements and diffusion theory. Rectangular regions indicate the range of distances (8-11.5 mm) used in the rat data analysis.

As a final note, we also performed Monte Carlo simulations (not presented) to investigate the effects of the heterogeneity of the rodent head and of the difference of sampled tissue volumes at 830 and 690 nm on our measurements. A two-layer diffusing medium was modeled (Martelli *et al.* 2002) comprising a superficial, 1 mm thick scalp/skull layer, and a second brain layer extending indefinitely. Our results showed that by using AC and phase data at source-detector distances in the range 8-11.5 mm, we

could successfully recover the concentration and oxygen saturation of hemoglobin in the bottom layer (brain) to within 0.1%.

References for Appendix B

Martelli, F., A. Sassaroli, Y. Yamada and G. Zaccanti (2002). "Analytical approximate solutions of the time-domain diffusion equation in layered slabs." J Opt Soc Am A Opt Image Sci Vis **19**(1): 71-80.

Appendix C

We analyzed the two-layered phantom data (Chapter 6, Section 6.2) using both the two-layered solution (Chapter 2, Section 2.3.2) and the homogenous solution (Chapter 2, Section 2.2.2) of the diffusion equation. The complete summary of the two-layered phantom experiments is reported below in Table C1, where we present the results using both two-layered and homogenous analysis. In comparison with the two-layered analysis, homogenous analysis performed: *i*) reasonably well in phantoms with 8 mm first layer thicknesses (Nos. 2 and 3); *ii*) worse in phantoms with 10 mm first layer thicknesses (Nos. 5 and 6); and *iii*) much worse in phantoms with 15 mm first layer thicknesses (Nos. 8,9,11 and 12) in retrieving the second layer absorption coefficient (μ_{a2}) (Table C1). We note that such results are indicative of the adequacy of homogeneous analysis for thin first layer thicknesses (here, <8 mm) in the source-detector distances that were considered (14–50 mm). Furthermore, the same comparison in the homogenous phantoms (Nos. 1, 4, 7 and 10) highlight the robustness of the two-layered analysis in homogeneous media.

Table C1. Summary of the phantom experiments. *True Value* represents optical coefficients measured in infinite medium geometry, and the actual thickness of the first layer; *Retrieved Value* represents two-layered phantom measurements retrieved simultaneously using our two-layered or homogenous inversion procedure; and *Error* represents the error between the true values and the retrieved values. Pink color highlights homogeneous phantoms.

		Two-Layered					Homogenous	
		μ_{a1} (mm^{-1})	μ'_{s1} (mm^{-1})	L (mm)	μ_{a2} (mm^{-1})	μ'_{s2} (mm^{-1})	μ_a (mm^{-1})	μ'_s (mm^{-1})
Phantom 1	True Value	0.009	0.69	8.0	0.009	0.69	0.009	0.69
	Retrieved Value	0.008	0.78	7.8	0.008	0.78	0.008	0.78
	Error	-7%	13%	-3%	-7%	13%	-7%	13%
Phantom 2	True Value	0.009	0.69	8.0	0.015	0.68	0.015	0.68
	Retrieved Value	0.009	0.74	8.0	0.014	0.73	0.013	0.70
	Error	-2%	7%	-1%	-4%	7%	-13%	2%
Phantom 3	True Value	0.009	0.69	8.0	0.015	0.93	0.015	0.93
	Retrieved Value	0.009	0.76	8.5	0.014	0.99	0.014	0.77
	Error	0%	10%	6%	-6%	7%	-9%	-17%
Phantom 4	True Value	0.009	0.69	10.0	0.009	0.69	0.009	0.69
	Retrieved Value	0.008	0.77	10.1	0.008	0.80	0.008	0.78
	Error	-8%	12%	1%	-10%	17%	-8%	13%
Phantom 5	True Value	0.009	0.69	10.0	0.017	0.68	0.017	0.68
	Retrieved Value	0.010	0.71	9.7	0.014	0.78	0.013	0.69
	Error	18%	3%	-3%	-13%	15%	-19%	1%
Phantom 6	True Value	0.009	0.69	10.0	0.016	1.02	0.016	1.02
	Retrieved Value	0.008	0.77	9.2	0.016	1.11	0.014	0.75
	Error	-14%	11%	-8%	-5%	8%	-16%	-27%
Phantom 7	True Value	0.009	0.68	15.0	0.009	0.68	0.009	0.68
	Retrieved Value	0.009	0.76	15.6	0.008	0.80	0.009	0.77
	Error	5%	11%	4%	-6%	17%	1%	13%
Phantom 8	True Value	0.009	0.68	15.0	0.015	0.68	0.015	0.68
	Retrieved Value	0.009	0.72	14.7	0.014	0.82	0.010	0.74
	Error	3%	5%	-2%	-7%	21%	-32%	9%
Phantom 9	True Value	0.009	0.68	15.0	0.015	0.92	0.015	0.92
	Retrieved Value	0.008	0.79	14.4	0.014	1.08	0.010	0.74
	Error	-6%	15%	-4%	-3%	17%	-34%	-20%
Phantom 10	True Value	0.009	0.69	15.0	0.009	0.69	0.009	0.69
	Retrieved Value	0.008	0.77	14.1	0.008	0.74	0.008	0.77
	Error	-4%	12%	-6%	-8%	8%	-7%	13%
Phantom 11	True Value	0.013	0.69	15.0	0.009	0.69	0.009	0.69
	Retrieved Value	0.015	0.75	14.2	0.008	0.72	0.011	0.82
	Error	10%	9%	-6%	-5%	5%	30%	20%
Phantom 12	True Value	0.017	0.69	15.0	0.009	0.69	0.009	0.69
	Retrieved Value	0.019	0.73	15.2	0.008	0.73	0.014	0.83
	Error	12%	6%	1%	-5%	6%	59%	21%